Understanding twinning mechanism and measuring twinning stress of the Cantor high entropy alloy applying micromechanical testing

Zur Erlangung des akademischen Grades einer

DOKTORIN DER INGENIEURWISSENSCHAFTEN (Dr.-Ing.)

von der KIT-Fakultät für Maschinenbau des

Karlsruher Instituts für Technologie (KIT)

angenommene

DISSERTATION

von

Camila Aguiar Teixeira, M.Sc.

Tag der mündlichen Prüfung	23. Juni 2025
Hauptreferentin	Prof. Dr. Christoph Kirchlechner
Korreferent	Prof. Dr. rer. nat. Gerhard Dehm

Abstract

The main object of this PhD thesis was to investigate deformation twinning on the Cantor high entropy alloy by applying *in situ* micro-mechanical testing. This work is divided in two parts: (i) a comparison of different micro-mechanical geometries in terms of twinning stress measurement and twinning mechanism investigation; and (ii) secondly insights into the twinning mechanism obtained by applying *in situ* SEM micro-pillar compression experiments.

In the first part, a comprehensive comparison was conducted between three micro-mechanical geometries (micro-shear, micro-pillar and micro-cantilever). Here, the challenges for each specimen preparation, their success rate in deformation twinning activation, as well as difficulties encountered during in *post mortem* analyses were considered. The results have shown that among the geometries tested, there were two suitable approaches: micro-shear and micro-pillar compression. The micro-shear case, offers the possibility of directly activate the twinning system with superior reproducibility. In contrast, the micro-pillars provide a fast and uncomplicated fabrication process allowing statistical analysis of the mechanical data. Micro-cantilevers were the least suitable approach for twinning studies, due to a lower success rate on twinning activation and a stress gradient that complicates quantitative interpretation of its mechanical data.

With that stablished, the remainder of the thesis, focusses on twinning mechanistic investigations and stress analysis, conducted with *in situ* micro-pillar experiments. A relatively wide range of micro-pillar diameters were tested (0.14 μm to 10 μm), which enabled a mechanical size-effect analyses of the twinning stress as well as a comparison with dislocation slip. Furthermore, this also offered insights regarding twinning mechanisms, as differences in mechanical behavior and slip activity were observed as diameter varied. Mechanical size-effect analyses showed negligible difference between dislocation slip and deformation twinning. As micro-pillar's diameter reached 10 μm deformation twinning was no longer observed, and, with that, the lower bound of the twinning stress was estimated around 130 MPa. And finally, a thorough *post mortem* investigation (including EBSD, SEM-BSE and TEM) suggested two twinning mechanism were exhibited. The primary is the three-layer model, proposed by Mahajan and Chin, which was predominant among the sub-micron micro-pillars and the secondary mechanism, present in 3 μm and 6 μm diameter micro-pillars, remains unclear. The three-layer model seems to be the predominant mechanism for the micro-shear geometry.

Kurzfassung

In dieser Dissertation geht es in erster Linie darum, Verformungszwillinge in der hochentropischen Cantor-Legierung durch mikromechanische *in-situ*-Prüfungen zu untersuchen. Diese Arbeit kann in zwei Teile unterteilt werden: (i) ein Vergleich verschiedener mikromechanischer Geometrien in Bezug auf die Messung der Zwillingsbildung und die Untersuchung des Zwillingsmechanismus; und (ii) Einblicke in den fundamentalen Zwillingsmechanismus, der durch die Anwendung von *in situ*-SEM-Mikrosäulendruckexperimenten gewonnen wurden.

Im ersten Teil wurde ein umfassender Vergleich zwischen drei mikromechanischen Geometrien (Mikro-Scher, Mikro-Säule und Mikro-Cantilever) durchgeführt. Dabei wurden die Herausforderungen bei der Probenvorbereitung, die Erfolgsquote bei der Bildung von Deformationszwillingen sowie Herausforderungen bei der Post-Mortem-Analyse berücksichtigt. Die Ergebnisse haben gezeigt, dass es unter den getesteten Geometrien zwei geeignete Ansätze gab: Mikro-Scherung und Mikro-Säule. Die Mikroscherung bietet die Möglichkeit, das Zwillingssystem direkt und mit hoher Reproduzierbarkeit zu aktivieren. Im Falle der Mikro-Säule bietet sie ein schnelles und unkompliziertes Herstellungsverfahren, das eine statistische Analyse der mechanischen Daten ermöglicht. Der Mikro-Cantilevern war die am wenigsten geeignete Geometrie für Zwillingsstudien, da er eine geringere Erfolgsquote bei der Zwillingsaktivierung und einen Spannungsgradienten aufweist, der die quantitative Interpretation seiner mechanischen Daten erschwert.

Auf dieser Grundlage wurde der Rest der Arbeit, d. h. die mechanistische Untersuchung der Zwillingsbildung und die Spannungsanalyse, mit *in situ*-Mikrosäulenexperimenten durchgeführt. Anschließend wurde ein relativ großer Bereich von Mikrosäulendurchmessern getestet (0,14 µm bis 10 µm), was eine Analyse der mechanischen Größenauswirkungen auf die Zwillingsspannung sowie einen Vergleich mit der Plastizität durch Versetzungsgleitung ermöglichte. Darüber hinaus bot dies auch Einblicke in die Mechanismen der Zwillingsbildung, da bei unterschiedlichen Durchmessern Unterschiede im mechanischen Verhalten beobachtet wurden. Mechanische Größeneffekt-Analysen zeigten einen vernachlässigbaren Unterschied zwischen Versetzungsgleiten und Deformationszwillingen. Als der Durchmesser der Mikrosäulen 10 µm erreichte, wurde kein Deformationszwilling mehr beobachtet, und die untere Grenze der Zwillingsspannung konnte auf etwa 130 MPa abgeschätzt werden. Schließlich ergab eine

gründliche Post-Mortem-Untersuchung (einschließlich EBSD, SEM-BSE und TEM), dass es zwei Mechanismen der Zwillingsbildung gibt. Der primäre ist das Dreilagenmodell, von Mahajan und Chin, das bei den Mikrosäulen im Submikrometerbereich vorherrschend war, während der sekundäre Mechanismus, der bei Mikrosäulen mit einem Durchmesser von 3 µm und 6 µm auftritt, unklar bleibt. Das Dreilagenmodell scheint der vorherrschende Mechanismus für die Mikro-Scher-Geometrie zu sein.

Table of contents

List of abbreviation

BSE	Backscattered electrons
BF	Bright field
CRSS	Critical resolved shear stress
DF	Dark field
EBSD	Electron backscattered diffraction
FCC	Face centered cubic
FIB	Focused ion beam
HEA	High entropy alloy
IPF	Inverse pole figure
IPF-Z	Inverse pole figure on Z direction
PF	Pole figure
SEM	Scanning electron microscope
SADP	Selected area diffraction pattern
SRO	Short range order
TEM	Transmission electron microscope
TD	Transverse direction
ZA	Zone axis

List of notations

τ_{bulk}	Bulk shear stress
$\tau_{2\%}$	Critical resolved shear stress at 2% strain
D_{mp}	Diameter of the micro-pillar
Δl	Displacement applied on the micro-pillar
Δ	Displacement applied on the micro-shear ligament
d_s	Distance separation between two partial dislocations
γ	Engineering shear strain
τ_{eng}	Engineering shear stress
ε	Engineering strain calculated for the micro-pillar
σ_{eng}	Engineering stress calculated for the micro-pillar
τ_{zx}	External stress
k	Fitting parameter
l_0	Height of the micro-pillar
H	Height of the micro-shear ligament
L	Length of the micro-cantilever
P	Load
b_p	Partial dislocation Burgers vector
v	Poisson's ratio
r	Radius
m	Schmid factor
G	Shear modulus
n	Size scaling exponent
γ_{sf}	Stacking fault energy
σ	Tensile stress on the micro-cantilever
w	Thickness of the micro-cantilever
D	Thickness of the micro-shear ligament
b	Width of the micro-cantilever
W	Width of the micro-shear ligament
$\sigma_{2\%}$	Yield stress at 2% strain offset

Acknowledgements

First and foremost, I owe my deepest gratitude to my supervisor, Prof. Dr. Christoph Kirchlechner, for the opportunity to work at the Karlsruhe Institute of Technology (KIT) and do my PhD under his supervision and guidance. I am immensely grateful for the incredible support I received over the years, beginning with writing the proposal, through the challenges of a PhD journey, until the final pages of this thesis. Thank you for so many insightful discussions and for providing such an encouraging and inspiring environment for scientific growth. I would like to extend my gratitude Prof. Dr. Gehard Dehm for reviewing this thesis and for being the co-examiner during my PhD defense.

This PhD work was carried out at the Institute for Applied Materials - Mechanics of Materials and Interfaces (IAM-MMI) in the *In situ* Microscopy group, led by Dr. Subin Lee. I am extremely grateful for your constant support in experiments and equipment training, for so many fruitful discussions and the encouraging atmosphere within the group. Thank you for always having your door open for discussions.

I would like to specially thank Prof. Dr. Reinhard Pippan, Prof. Dr. Jon Molina, Prof. Dr. Peter Gumbsch and Prof. Dr. Guillaume Laplanche for the fruitful scientific discussion and invaluable contributions.

My sincere gratitude goes to all my IAM-MMI colleagues, for all the support and, direct or indirect, contributions during my PhD. And also extend my thanks to Dr. Alexander Kauffmann, from IAM-WK, for providing all the samples used in this PhD work.

I would like to express my appreciation to all my group members, Dr. Eloho Okotete, Angelica Medina, Dr. Divya Bandla, Dr. Ujjval Bansal, Yinxia Zhang, Ved Gumaste, for all the support during rehearsals, scientific discussions and fun moments shared, in and out of office. I would like to specially thank my officemate, Dr. Eloho Okotete, for all discussions and laughs shared in our office (and for finally admitting I am the funny one). A special thanks to Dr. Ujjval Bansal for the time spent with TEM analyses and discussions, and to Dr. Divya Bandla for the support with ECC imaging. And I am also grateful to Dr. Maria Vrellou, for the conversations over coffee, daily gossip and fun times together.

Moving to another country to do my PhD was a big challenge and I truly appreciate having such an amazing group of friends in Karlsruhe, but also back home (and some around the world), for always providing me with moral support, most needed distractions and encouragement.

I would also like to express my deepest appreciation to my family, for their unwavering support, yearly visits and phone calls, that shortened the distance and kept me going during tough times. I am deeply grateful to my loving parents, Joao and Gina, for the unconditional love and support I received throughout my entire life. And I am grateful to my brothers, Caio and Lucas, for the companionship and encouraging words through this PhD journey.

Finally, I would like to thank the Karlsruhe House of Young Scientist (KHYS) for the Networking grant and Prof. Dr. Jon Molina for kindly accepting and organizing my stay at IMDEA in Spain. And I'm also grateful for the Robert Bosch Foundation for funding my doctorate research at the KIT and Karlsruhe Nano Micro Facility (KNMFi) for supporting the TEM work.

1. Motivation

Since first reported in 2004, there has been an increasing scientific interest surrounding high entropy alloys (HEAs) [1,2]. It was one of the first times an alloy with at least 5 elements in an equiatomic composition, forming a single phase solid solution was reported [1], and questions involving its deformation mechanisms and potential properties (or combination of them) were raised. The equiatomic CoCrFeMnNi alloy, known as the Cantor alloy, is by far the most researched HEA, due to its outstanding combination of mechanical properties, which also extends to extreme environments (i.e. cryogenic temperature) [3–6]. Moreover, although the Cantor alloy has been widely investigated, there are fundamental questions remaining in terms of their underlying deformation mechanism and this work focuses on one of them: deformation twinning.

The outstanding mechanical properties of the Cantor alloy include but are not limited to: high ductility and tensile strength, as well as fracture toughness [3–6]. The mechanical behavior has often been attributed to mechanical twinning. It is understood that dynamically formed twins act as barriers to dislocation motion, which provide additional work hardening, delaying necking instability and postponing fracture [4]. Under cryogenic conditions, deformation twinning is observed early during deformation, contributing to work hardening, however, the lower yield strength achieved at room temperature requires additional work hardening for the twinning stress to be reached, causing twinning to be formed close to fracture [4]. Given the importance of deformation twinning as a deformation mechanism in FCC HEAs, in-depth understanding of the underlying mechanism(s), including measuring the stress necessary for its formation (i.e. twinning stress), is crucial for advancing HEAs design.

The drive for in-depth knowledge of underlying deformation mechanisms led to the development of the *in situ* micro-mechanical testing techniques [7]. The goal was to mechanically test materials locally, obtaining insights into individual mechanisms and respective activation stresses, not being prone to stress heterogeneity experienced in polycrystalline bulk sample tests. Micromechanical testing is allied to focused ion beam (FIB) milling, which enables specimen fabrication in particular crystallographic orientations or grain boundaries of interest, and tests are performed inside a scanning electron microscope (SEM). This allows their mechanical behavior to be observed simultaneously as load and displacement curves are recorded. In this work, *in situ* micro-mechanical techniques are combined with advanced microstructural characterization techniques

such as SEM, electron backscattered diffraction (EBSD), transmission electron microscope (TEM), which enable an in-depth investigation of the underlying mechanism.

With that in mind, the first question to answer is: can twinning stress be measured with micro-mechanics? Thus far, twinning stress measurements have been performed in bulk samples, through interrupted mechanical tests followed by *post mortem* analysis. In polycrystalline microstructure, however, the local stress causing twinning cannot be measured. Here, *in situ* micro-mechanical tests might be an attractive alternative, because it enables the investigation of mechanism individually, as previously remarked. Therefore, the first goal of this work is to develop protocols to measure the twinning stress which consisted in comparison of three different micro-mechanical testing geometries: micro-shear, micro-pillar and micro-cantilever. This is the focus of Chapter 4, where a comprehensive comparison is done and the suitable geometries to study deformation twinning are discussed.

The second goal of this work is to provide insights into the twinning mechanism of the Cantor alloy. Currently, there is no agreement regarding how deformation twins are formed, however, several models have been proposed. Therefore, in Chapter 5, *in situ* micro-pillar compression tests combined with advanced microstructural characterization techniques are applied to investigate the twinning mechanism. Micro-pillar compression test is a unique tool to study size-effect, due to the ease in testing samples in nano to micron scale. Thus by varying the micro-pillars diameter, different stress levels are applied and possible changes in mechanical behavior can be observed. This way, each micro-pillar is examined for deformation twinning activation, slip activity and previously proposed twinning mechanism are evaluated according to the results obtained.

This thesis is comprised in the following chapters: in Chapter 2 the literature review consisting of a background in HEAs, deformation twinning and micro-mechanical testing; in Chapter 3 the materials and methodology is explained in detail; in Chapter 4 a comparison between testing geometries is conducted, which is based on the published manuscript [8]; in Chapter 5 *in situ* micro-pillar compression experiments are performed to obtain insight into the twinning mechanism and conduct a stress analyses on the Cantor HEA, which based on a manuscript under review [9]; and, finally, Chapter 6 presents a summary of the thesis followed by an outlook in Chapter 7.

2. Literature review

2.1. High entropy alloys

High entropy alloys (HEAs) or multicomponent alloys emerged around 2004, when two differently motivated approaches were proposed with a similar goal: innovative materials design [1,2]. Conventionally, alloys consist of one or two major components with small addition of alloying elements based on required properties. This often leads to a tradeoff in terms of properties, e.g. ductility over strength [10]. At the time, it was pointed out that this method was restrictive in terms of elemental composition, focusing on the edges of the phase diagram and resulting in limited number of alloy possibilities as well as properties combinations [1,2]. However, a multiple principal element approach would be generally avoided as brittle intermetallic with complex microstructures were expected to form [2]. In an attempt to escape conventional metallurgy methods, Cantor and co-workers investigated several multicomponent alloys containing equiatomic ratios of transition metals with the motivation of exploring the phase diagram's center [1]. The high entropy approach was suggested by Yeh and co-workers, which they proposed that stable solid solutions could be formed in five or more multiple element alloys due to their large mixing entropy [2]. Although presenting different motivations, both concepts intersect in the idea of exploring multiple principal element alloys, breaking the conventional pattern, which theoretically would lead to a wider number of new possible alloys with potentially enhanced properties combinations [1,2].

Since discovered, there were four hypothesized core effects in HEAs, which were believed to result in their outstanding properties: the high entropy effect, lattice distortions, sluggish diffusion, and, lastly, the cocktail effect [11–13]. The high entropy effect, their maiden concept, proposes that as number of elements are increased (i.e. from 5 up to 13 elements) the high entropy of mixing would result in stable single solid solutions [12]. The lattice distortion effect arises from the difference in atomic sizes between the atoms composing such multi-principal element alloys, given that all atoms are essentially solutes, which in turn can influence their mechanical properties (see Figure *2-1*) [12]. Their diffusion was believed to be slower than in conventional alloys, which was based retention of nanocrystal even after annealing [11]. And the cocktail effect, which suggests that unexpected properties could emerge from complex elemental combination [11,14]. Additionally,

short range order (SRO) has also been suggested as a core effect, which can affect their mechanical properties [15].

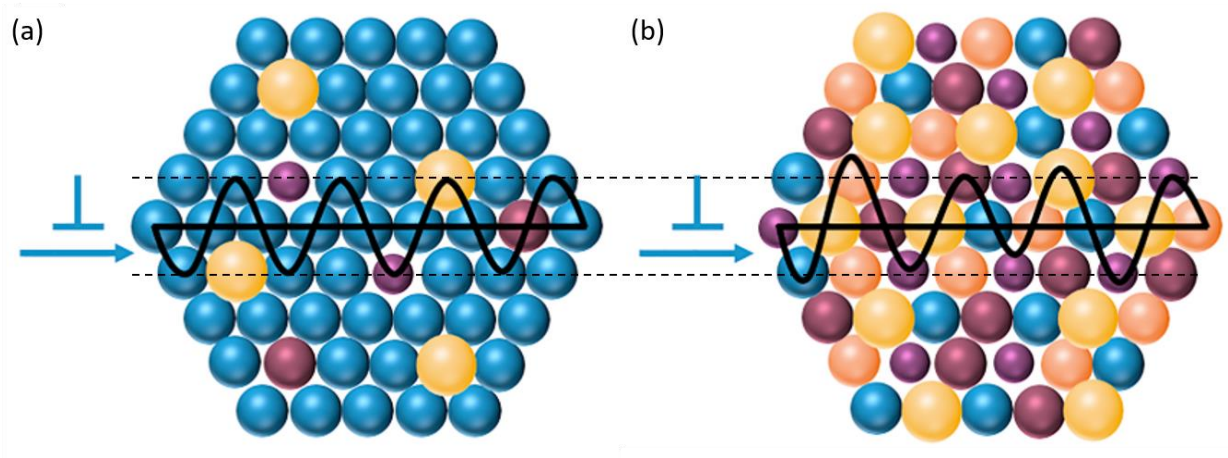

Figure 2-1 Schematic representation of dislocation motion and different Peierls-Nabarro energy barrier field in: (a) a dilute solid solution and (b) HEA (modified from [16]).

However, these HEAs' core effects have been subject of debate over the years. For instance, the influence of high entropy effect on phase stability has been questioned, as multiple equiatomic five element alloys have shown presence of intermetallic phases [17], suggesting other factors such as enthalpy could favor phase stabilization, which is further supported by the single phase medium entropy alloys that have been reported [18]. Furthermore, the sluggish diffusion initial assumptions were also disputed as most evidences so far suggested that their diffusion coefficient does not differ from conventional alloys [19–21].

The "severe" lattice distortion has also been debated, as first principle calculations showed that the Cantor alloy and subsets present a small average atomic displacement from ideal lattice position [22]. It was also suggested that a particular combination of elements provide solute strengthening depending on the misfit volume, which in turns depends not only on the elements' radii but also the others present in the alloy [22,23]. A theory of solute strengthening for FCC HEAs was proposed by Varvenne et al. [24–26], it suggests that the strengthening would result from the interaction energies of the solute and dislocations. Local energetic fluctuation can arise from randomly distributed solutes and, once interacting with the solutes, dislocations adopt a wavy

configuration reducing the total dislocation energy [24]. Recently it was reported for the VCoNi equiatomic medium entropy alloy reached higher yield strength compared to the CrCoNi, refined grain (2 μm) was near 1 GPa, and it was attributed to severe lattice distortion, as the mean square atomic displacement was nearly twice compared to the Cantor alloy and subsets [27].

The more recent core effect, the SRO could be defined as a deviation of local chemical or topological order from a random atomic distribution [15]. Although initially thought as a random solid solution, the chemical complexity of HEAs could favor the formation of SRO [15]. Reports suggest that the SRO can affect the stacking fault energy [28–30], magnetic [31] and mechanical properties [28]. If the SRO affects positively the HEAs or MEAs mechanical properties is still in debate, as experimental reports so far have been conflicting showing either an increase yield strength and hardness [28] or no measurable effects at all [32–34]. However, recent studies believe that by tuning short range order and/or lattice distortions, enhanced mechanical properties can be achieved [35,36].

The major task in literature thus far has been understanding the HEAs' found properties and how do they differ from conventional alloys: (i) are there enhanced properties and (ii) is there a difference in terms of mechanisms? As pointed out by George and co-workers [10] on their recent review on HEAs' mechanical properties, within the research done so far, it doesn't seem that the HEA's outstanding mechanical properties can be explained solely by their core effects, such as severe lattice distortion or solute strengthening [37,38]. Additional mechanisms which are similarly observed in conventional alloys as for instance mechanical twinning, interstitial solid solution strengthening, etc., are often associated with improvements in mechanical properties [3–6,39]. However, the key relevant aspect of further developing HEAs, is the possibility of tuning mechanical properties – combining properties that are otherwise mutually exclusive – and, with that, obtain enhanced advanced alloys [10].

The Cantor alloy (equiatomic CrCoFeMnNi), for instance, exhibited an exceptional mechanical behavior, including an inverse temperature dependence in yield strength and work hardening [5,6]. Meaning, as temperature decreased both tensile strength and ductility increased considerably, compared to room temperature tests [5,6]. Furthermore, their exceptional damage tolerance, a good combination of high fracture toughness and yield stress [3] (see Figure 2-2), led the Cantor alloy

to be by far the most researched HEA, as there was an increased interest to further understand the underlying mechanism that promotes such behavior.

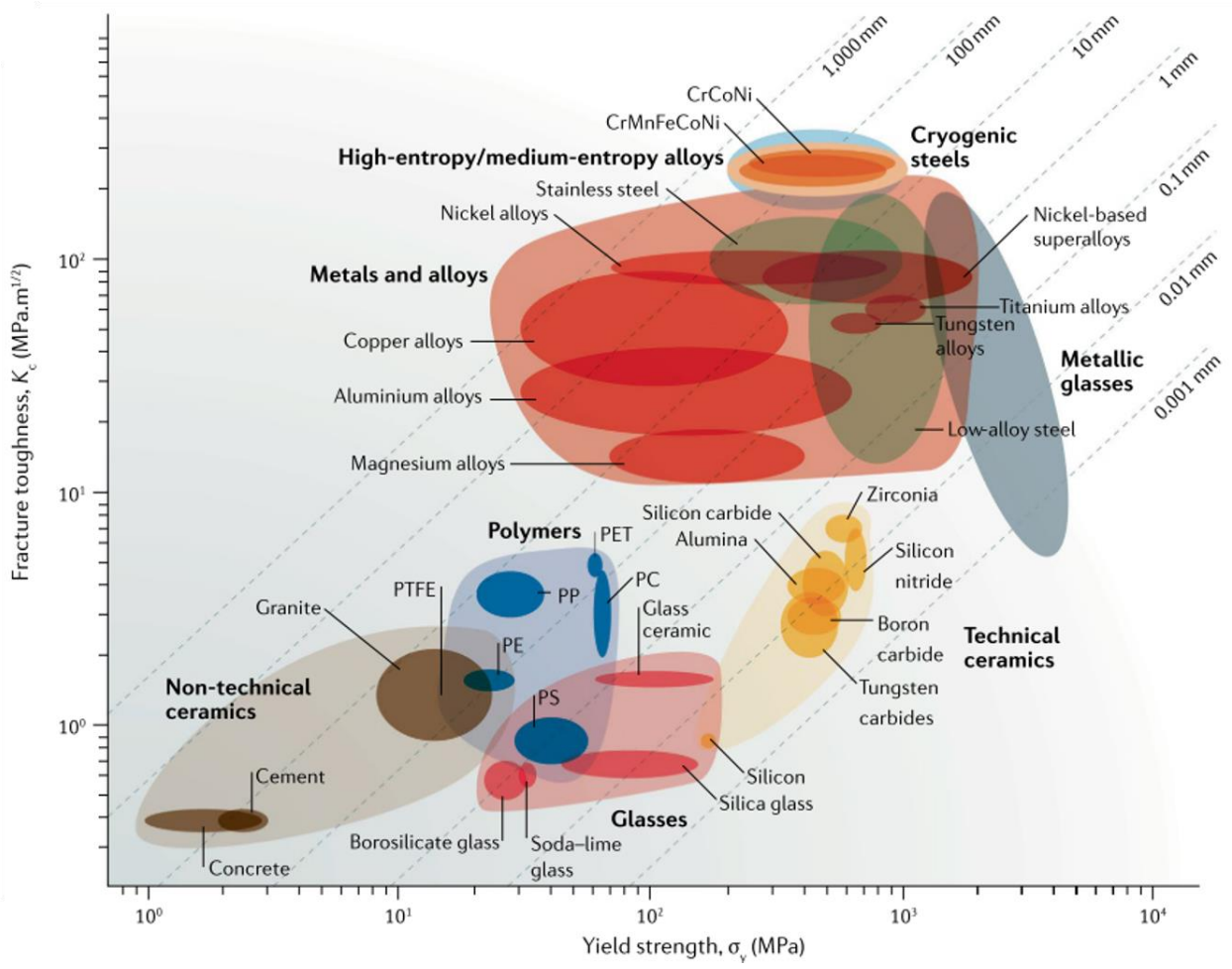

Figure 2-2 Ashby map with fracture toughness (K_c) and yield strength (σ_y) comparing several materials highlighting the CoCrNi-based HEAs (reprinted from [18]). Note that the dashed lines represents the values for plastic-zone radius (${K_c}^2/\pi{\sigma_y}^2$).

2.1.1. Deformation twinning in FCC HEAs

Although the presented flow stress and ductility increase under cryogenic conditions is not an entirely new behavior, previously observed in Cu-based alloys for instance [40–42], the Cantor alloy standouts by also maintaining high fracture toughness [3,18]. For some many FCC HEAs, a

continuous steady work hardening was observed for samples tested at cryogenic temperatures compared to room temperature tests (see a representative case for the Cantor alloy in Figure 2-3(a)) [3–6,23,43,44]. Early studies attributed this behavior to deformation twinning, as it is accepted that twinning introduces new interfaces, i.e. twin boundaries, which causes the "dynamic Hall-Petch" effect. Essentially, grains will be sectioned into smaller grains, acting as obstacles by reducing the dislocation free mean path, which in turn leads to additional work hardening that delays necking instability and catastrophic failure through fracture. The extensive mechanical twinning was associated to their low stacking fault energy [3], which later was shown to decrease as temperature decreases, overall improving twinability [45].

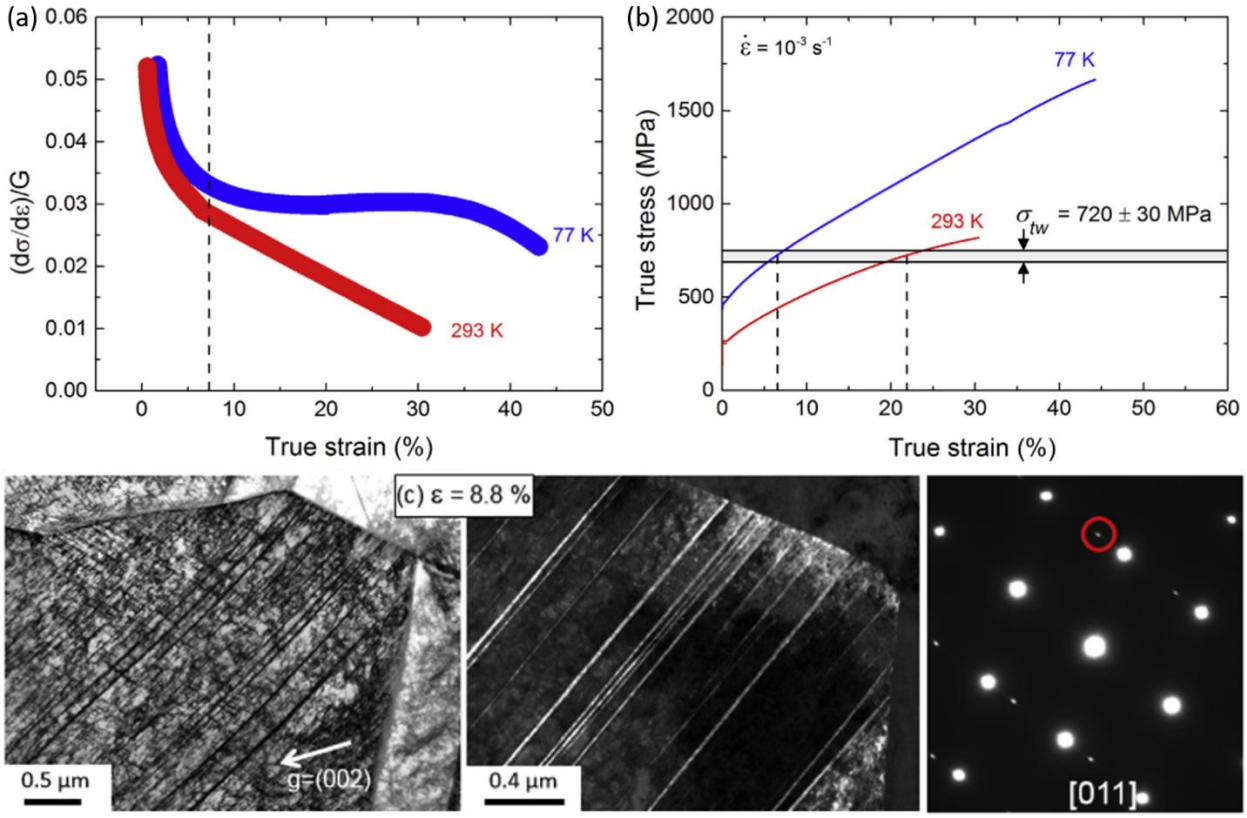

Figure 2-3 Mechanical behavior of the Cantor alloy under 77 K and 293 K and *post mortem* analysis showing deformation twinning: (a) work hardening scaled with shear modulus versus true strain plot and (b) true stress and strain plot; (c) TEM bright field (left) and dark field (middle) micrographs with selected area diffraction patterns showing the twin and matrix spots (modified from [4]).

Since deformation twinning was observed in polycrystalline Cantor alloy samples, under particular stress states at room temperature [46], but not under uniaxial tensile stress for 2% and 20% strain [6], this motivated a study carried out by Laplanche and co-workers in 2016 [4]. This work was the first attempt to pin point when deformation twinning occurs, in both cryogenic and room temperature, understanding how the onset of mechanical twinning affects flow stress and work hardening, and experimentally measure the critical stress for twinning activation on the Cantor alloy [4]. Through interrupted tensile tests followed by TEM analyses (Figure 2-3(c)), evidences of deformation twinning around the onset of the continuous work hardening was observed for 77 K (Figure 2-3(a)), suggesting a contribution of this deformation mechanism to delay necking [4]. At room temperature, deformation twinning was only observed at later stages of the experiment (close to fracture), which was explained by the lower stresses at room temperature and additional strain was needed for the critical stress to be reached [4]. Deformation twinning is believed to be a stress controlled mechanism and this critical stress is known as the twinning stress [47–51]. In this case, the twinning stress showed no temperature dependence (similarly observed by [49]) and was estimated to be 235 MPa (see Figure 2-3(b)) [4]. Since this first twinning stress measurement attempt, several macro scale experiments were performed studying the effects of stacking fault energy, crystallographic orientation, grain size and temperature [52–57], and also predictions through simulations [58,59]. The twinning stress of the Cantor alloy was found to be around 110 MPa and 378 MPa [4,53,55,56,60].

Given the importance of twinning as a deformation mechanism of FCC alloys and its impact on mechanical behavior, in-depth understanding of how the mechanism develops and which stresses are required for this processes are crucial for a mechanism-based development of advanced HEAs. Prior to the present work, experimental twinning stress measurements for the Cantor alloy have been performed through interrupted mechanical bulk scale tests followed by *post mortem* analysis, which raises concerns regarding the proper measurement of stresses locally due to the surrounding microstructure. Other well-established approaches could be more reliable not only to perform such measurements but also to provide insights into the underlying mechanism, and will be further discussed in Section 2.3. But firstly, the deformation twinning basic concepts and proposed mechanisms for FCC alloys will be discussed in the next section.

2.2. Twinning mechanism FCC alloys

The process which describes deformation twinning formation and growth, i.e. the twinning mechanism, remains a debate in literature. However, the role of crystallographic orientation [54,56,61], dislocation slip activity [62], stacking fault energy [63,64], temperature [44] and strain rate [49,51] are well understood.

The stacking fault energy is inversely proportional to the stacking fault distance. In FCC alloys, full dislocations dissociate in to two Shockley partial dislocations separated by a stacking fault. The lower the stacking fault energy, the larger is this separation, which in turn minimizes cross-slip (planar glide often observed [6,65]) and also favors deformation twinning [52]. As for temperature and strain rate effects, the flow stress increases with the increase of the strain rate and decrease of temperature [51,66]. In higher flow stress, the critical stress for twinning is easily achieved in earlier stages. Of course, this holds true assuming twinning stress is insensitive to temperature and strain rate. For the Cantor alloy, twinning stress is temperature independent [4,49], however, it increased from 760 MPa to 885 MPa in a strain rate of 10^{-4} s^{-1} to 4700 s^{-1} respectively [67].

It is accepted that dislocation slip precedes deformation twinning [62]. For FCC alloys, deformation twinning can be triggered by the glide of Shockley partial dislocations, named as twinning partials (i.e. $\langle 112 \rangle$), subsequently on adjacent $\{111\}$ planes [61]. The twinning system therefore is $\{111\}\langle 112 \rangle$. Each twinning partial dislocation will produce a stacking fault and this repeated process leads to the formation of a micro-twin. During the deformation twinning process, the twinned region is sheared into a permanently different crystallographic orientation [66]. However, the twinned region and matrix (i.e. parent) relate by: a mirror symmetry sharing a common $\{111\}$ plane (i.e. mirror plane or twinning plane), which can be best viewed along a $\langle 110 \rangle$ orientation and at the twin boundary an angle of 141° is observed [66]; and a 60° misorientation with a rotation around a $\langle 111 \rangle$ axis [68].

Deformation twinning is also known for a crystallographic orientation and stress state dependency, because, the shear stresses acting on the leading and trailing partial dislocations will differ according to the stress state applied in a given crystallographic orientation, resulting in a tension-compression asymmetry [51,61]. For instance, considering a compressive stress state, moving from the $\langle 113 \rangle - \langle 102 \rangle$ line (see Figure 2-4) towards the lower left corner of the inverse pole

figure (IPF) (close to a ⟨001⟩ loading direction), the highest calculated Schmid factor is on the leading partial dislocation. Meanwhile, towards the right side of the IPF (close to ⟨111⟩ or ⟨101⟩ loading direction), the trailing partial dislocation would have the highest calculated Schmid factor. And the opposite is observed under a tensile stress state (see Figure 2-4). Thus, the ⟨113⟩ − ⟨102⟩ line represents orientations which stress acting on both partial dislocations are equal. Therefore, to promote twinning the goal in both cases (either in a tensile or a compressive stress state) is to maximize the resolved shear stress on the leading partial dislocation. This leads to extension of the stacking fault between the two partial dislocations favoring twinning [69,70].

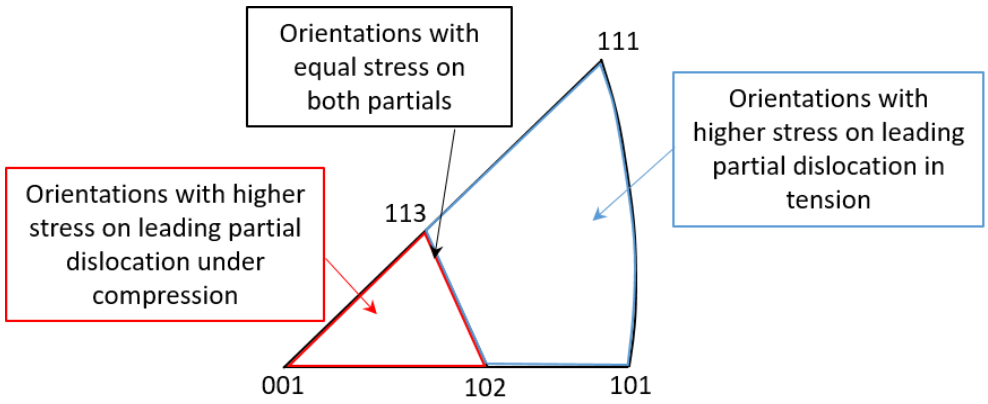

Figure 2-4 Inverse pole figure (IPF) with the representation of maximized shear stresses on leading partial dislocations based on their crystallographic orientation and stresses applied (based on [61]).

Despite these basics on deformation twinning, its underlying mechanism remains a question to date. Classically, deformation twinning formation is explained as mentioned above, by emission of Shockley partial dislocations on adjacent {111} planes, leaving a stacking in each plane, which leads to the formation of a micro-twin [61]. Such classical mechanism has been suggested as the twinning mechanism for different alloys at the nano to micron scale [71–73]. However, the motion of Shockley partial dislocations on {111} planes seems to oversimplify the complex twinning mechanism and more elaborated models have been proposed over the years [74–80]. Given that some models will require solely single slip activation and other multiple slip activation to occur, they will be further categorized in to single (see Figure 2-5) and multiple slip models (see Figure *2-8*, 2-7 and 2-8), as summarized in Table 2-1.

In the single slip activation case, there are two main models: the three-layer mechanism from Mahajan and Chin [76], and the pole mechanism from Venable [74,75]. The three-layer model, glide of co-planar dislocations with different Burgers vectors occur and the interaction of such dislocations which generates the three-layer fault that acts as a twin source (see Table 2-1 and Figure 2-5(a)) [76]. The reaction between the co-planar dislocations, DA and BA (in Thompson tetrahedron standard notation) is of repulsive nature, therefore, it requires high stresses to occur [76]. The authors proposed that, instead, a constriction would occur in the dissociated DA (constriction not shown in Figure 2-5(a)). The constricted segment dissociates and a swap between leading (Dγ) and trailing partial dislocation (γA) occurs, resulting in an anomalous fault, which is converted to an extrinsic fault, if the dissociation in $D\gamma \rightarrow \gamma B + \gamma A$, and $\gamma A \rightarrow B\gamma + D\gamma$ occurs (as seen in Figure 2-5(a)) [81]. Then, partial dislocations Bγ and γB would annihilate. The extrinsic fault converts to the three-fault layer (3γA), i.e. twin source [76]. As a result, the twin and slip bands would lie on the same plane.

The other single slip model was proposed by Venables [74,75], known as the pole mechanism, which was an extension of a model previously suggested for BCC alloys [82], but in this case focusing on FCC alloys (see Table 2-1 and Figure 2-5(b)). This model requires a prismatic source (CB), a long jog along AD pinned at the two nodes, N_1 and N_2. It suggests that CB dissociates in to a Shockley partial dislocation (γB) and a Frank partial dislocation (Cγ), which acts as the pole dislocation [74,75,83]. The Shockley partial dislocation glides away, rotating in opposite direction (producing a fault layer) until reaching the pole dislocation again [74,75,83]. And, through each operation, the twin source is reformed in a different adjacent plane and the twin lamella growth occurs [74,75,83].

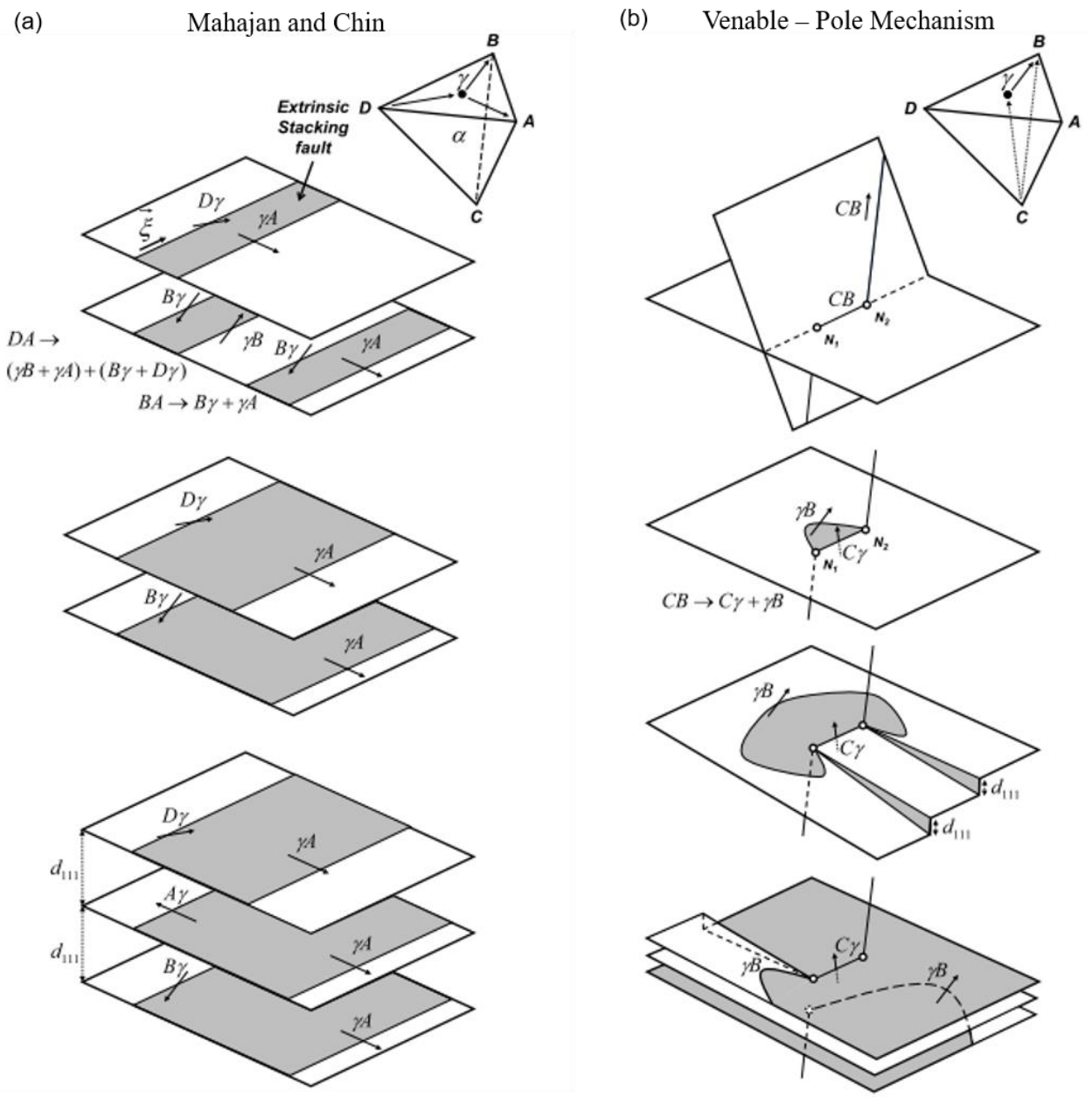

Figure 2-5 Schematic representation of the single slip models: (a) Mahajan and Chin's three-layer model and (b) Venable's pole mechanism. (modified from [84])

For the multiple slip models, as named, it requires activation of multiple slip systems to occur for the twin source to be formed such as: the two-layer [77], Cohen and Weertman [78] and stair-rod cross-slip mechanisms [79,80] (see Table 2-1 and Figure 2-6, 2-7 and 2-8). The two-layer model suggests the dislocation (BA) would pile-up against the Lomer dislocation (DC), which is located

in the intersection of the primary γ and cross plane α [77,85]. The two-layer fault (2γA), which may act as a twin source, would be formed through the reaction of the leading BA dislocation of the pile up with the Lomer dislocation [77,85].

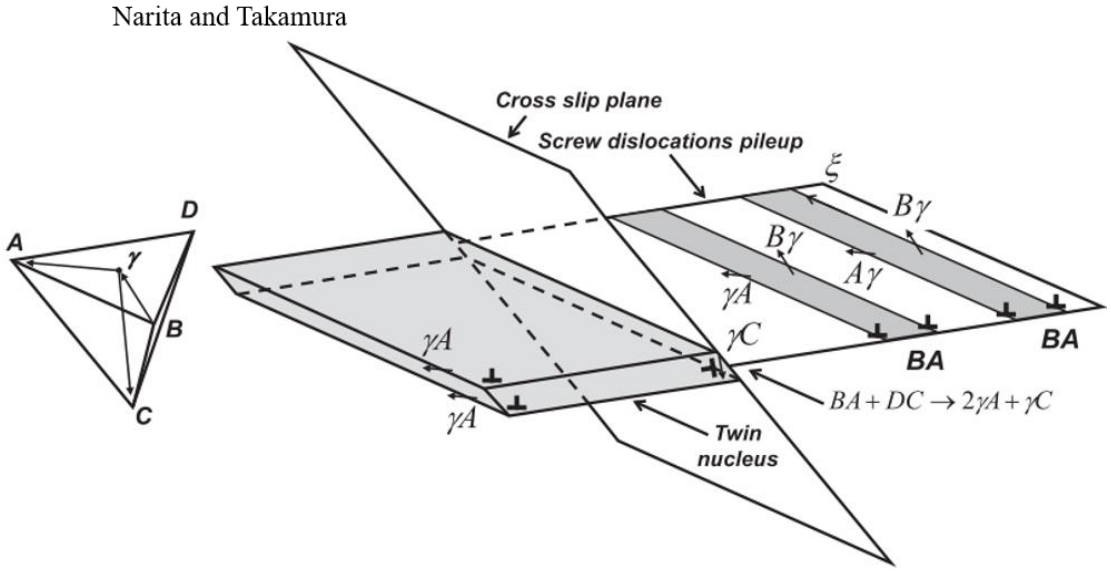

Figure 2-6 Schematic representation of the Narita and Takamura's two-layer model (modified from [84]).

The Cohen and Weertman model [78] on the other hand, suggests that many stacking faults would be created through the split of (AC) dislocations into Shockley (Aγ) and Frank partial (γC) dislocations, as dislocations (DA) and (AC) pile-up against a Lomer-Cottrell lock that intersects planes δ and γ (see Table 2-1 and Figure 2-7). The Shockley partial dislocation (Aγ) moves oppositely to the Frank partial dislocation (γC) and away from the pile-up (AC), creating a stacking fault [78]. This model considers that many stacking faults would be produced, leading to twin formation: (i) due to the large number of dislocations in the pile up, which could split and form additional stacking faults; (ii) through the same process repeated in adjacent planes, due to the presence of other Lomer-Cottrell locks, thus forming additional stacking faults [78].

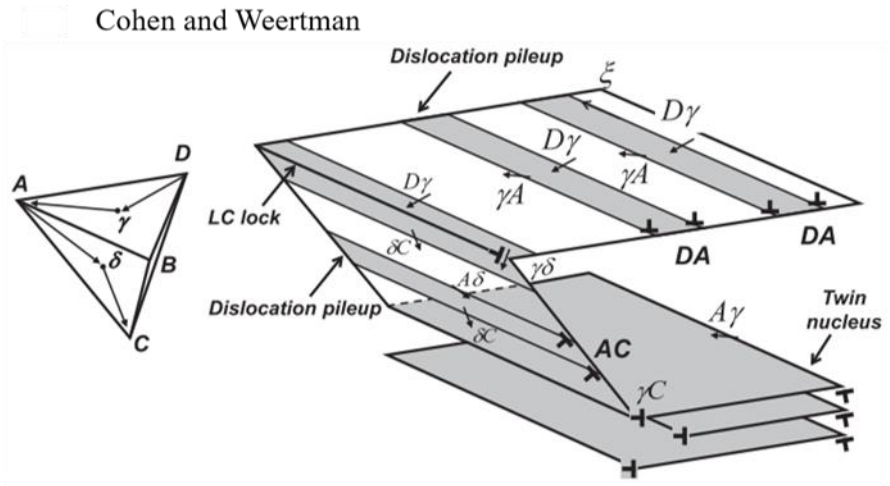

Figure 2-7 Schematic representation of the Cohen and Weertman model (modified from [84]).

And finally, the stair-rod cross-slip mechanism which was proposed by Fujita and Mori [79,80]. It was suggested that once the dislocation (DA) encounters an obstacle such as Lomer-Cottrell lock, the Shockley partial dislocation (Dγ) on the primary plane (γ) dissociates into the Shockley partial dislocation (Dα), i.e. twinning dislocation, on the conjugate plane (α) and the stair-rod dislocation (αγ) (see Table 2-1 and Figure 2-8) [80,83]. The twin lamella is formed in the conjugate plane and growth develops by the repeated stair-rod cross-slip events, which occurs if resolved shear stresses on the conjugate plane (α) is higher than on the primary plane (γ) [79].

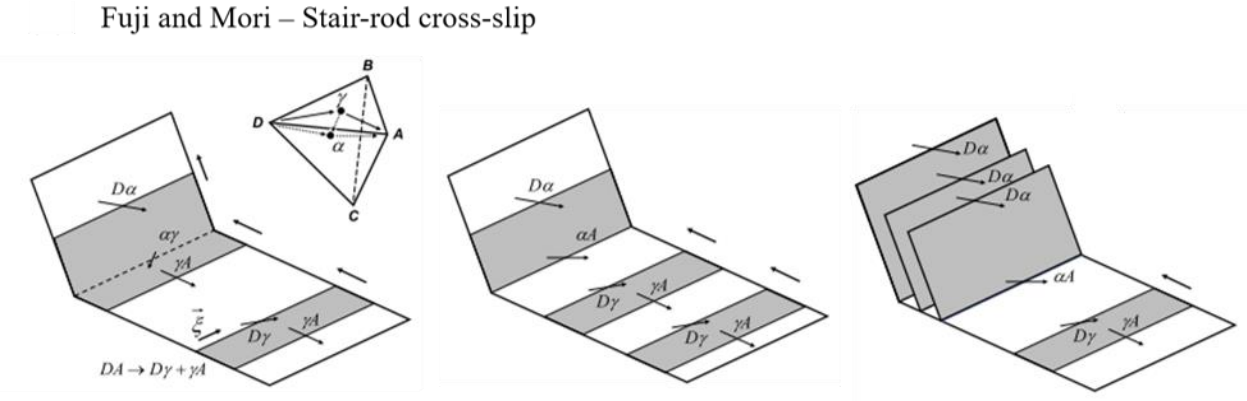

Figure 2-8 Schematic representation of the Fuji and Mori's stair-rod cross-slip model (modified from [84]).

Table 2-1 Summary of twinning mechanism models sorted by single or multiple slip, and their respective dislocation reaction to form the twin source (based on [83]).

Model	Dislocation reaction (Thompson tetrahedron notations)	Mechanism
Single slip	$\frac{1}{2}[101]+\frac{1}{2}[1\bar{1}0]\rightarrow 3\frac{1}{6}[2\bar{1}1]$ (DA+BA → 3γA)	Three-layer (Mahajan and Chin) [76]
	$\frac{1}{2}[\bar{1}01] \rightarrow \frac{1}{3}[\bar{1}\bar{1}1]+\frac{1}{6}[\bar{1}21]$ (CB → Bγ+γC)	Venables pole [74,75]
Multiple slip	$\frac{1}{2}[1\bar{1}0]+\frac{1}{2}[011] \rightarrow 2\frac{1}{6}[2\bar{1}1]+\frac{1}{3}[11\bar{1}]$ (BA+DC → 2γA+γC)	Two-layer (Narita and Takamura) [77]
	$\frac{1}{2}[101]+\frac{1}{2}[01\bar{1}] \rightarrow \frac{1}{2}[101]+\frac{1}{6}[\bar{2}1\bar{1}]+\frac{1}{3}[11\bar{1}]$ (DA+AC → DA+Aγ+γC)	Cohen and Weertman [78]
	$\frac{1}{2}[101] \rightarrow \frac{1}{6}[112]+\frac{1}{6}[2\bar{1}1] \rightarrow \frac{1}{6}[121]+\frac{1}{6}[0\bar{1}1]+\frac{1}{3}[1\bar{1}1]$ (DA → Dγ+γA → Dα+αγ+αA)	Stair-rod cross-slip (Fujita and Mori) [79]

2.3. *In situ* micro-mechanical testing

As mentioned in section 2.1.1, twinning stress measurements for the Cantor alloy have been mainly performed through interrupted bulk scale mechanical tests [4,52–56]. This would then consist of tensile or compression tests interrupted in particular strain levels, followed by a *post mortem* analysis which vary from EBSD mapping to an in-depth analysis with TEM. Then the stress range for twinning activation would be defined and the twinning stress estimated from the engineering stress. However, these stresses will be greatly affected by the local microstructure, which in turn results in stress heterogeneities, making it difficult the correlation between stresses and individual mechanism. Therefore, this type of bulk scale measurements may not provide the twinning stress quantitatively. An alternative method for strength measurements, free of surrounding microstructure influence, was developed by Uchic and co-workers in 2004 [7]. In this mechanical testing method, cylindrical samples for compression were prepared by FIB based techniques and

a nanoindenter equipped with a flat punch was used to perform the small scale mechanical tests. FIB sample fabrication is key, as it allows a specimen to be fabricated directly in either a grain, of particular crystallographic orientation, or a grain boundary desired for the work. Later, this method was adapted to work inside the SEM, allowing the *in situ* observation of the mechanical test as deformation occurs, with the load and displacement data, as well as the SEM video simultaneously recorded. This type of small scale mechanical testing finally enabled the study of underlying mechanisms, allowing stress measurements to be performed locally [86]. From this invention, a series of *in situ* SEM micro-mechanical testing with different geometries were established.

In this work, three micro-mechanical testing geometries were applied and they will be the only ones discussed (in terms of advantages and disadvantages) in detail in this section: micro-pillar, micro-shear and micro-cantilever. The comparison between micro-mechanical testing geometries to measure the twinning stress is the focus of Chapter 4.

2.3.1. Micro-pillar compression

The first geometry reported was the micro-pillar, which is the geometry used for small scale compression tests [7]. In this case, cylindrical specimens are FIB milled by either annular or Lathe techniques (Figure 2-9) [87]. Although the Lathe technique (Figure 2-9(a)) provides a well-defined micro-pillar with a constant cross-section, this technique is not widely applied mainly because of its time-consuming fabrication and great FIB damage on sample's surface, due to repeated scanning during the fabrication process to guarantee a good alignment [88]. Instead, annular milling (Figure 2-9(b)) is the most commonly used technique, which provides samples not perfectly defined, as the incident beam 90-degree angle introduces a taper angle (causing a stress gradient), however, its fast fabrication process allows easy statistical analyses, which can be important in small scale mechanics.

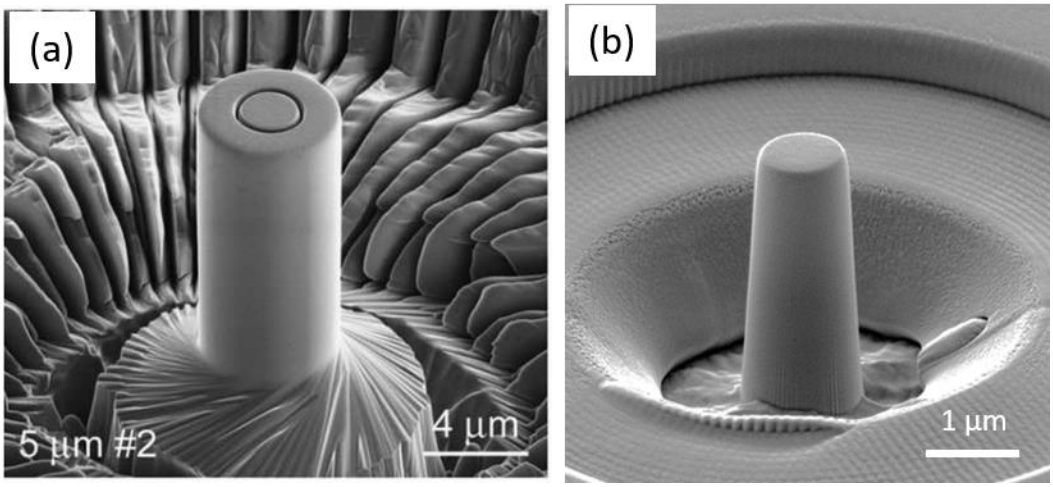

Figure 2-9 Resultant micro-pillar shape depending on milling technique: (a) Lathe (reprinted from [89]) and (b) annular milling.

The micro-pillar's imperfect shape allied to testing set-up related issues, require few predefined assumptions and experimental protocols to be followed to allow an artifact poor data extraction [86]. These assumptions involve: a constant cross-section throughout the micro-pillar, pure axial loading during test, deformation concentrated in the micro-pillar volume and testing set-up stiffness having a negligible influence in the mechanical data [86]. For yield stress extraction with negligible error, the micro-pillar's taper angle should be maintained below 1.5-degrees [90]. To minimize the effect of lateral forces and friction, which could eventually lead to a non-uniaxial stress state, unloading segments should be applied during a test [91]. Additionally, buckling can be avoided by keeping an aspect ratio diameter-height between 1:2 or 3 [92]. And finally, imprints on the bulk sample surface can be used to optimize a proper sample to indenter tip alignment, which in turn avoids unwanted/unexpected slip systems to be activated as well misinterpretation on the load displacement curves [93].

Although there are clear shortcomings about micro-pillar compression tests, it is one of the most used micro-mechanical geometry thus far, given the ease of sample preparation in a nano to micron scale, which finally enabled studies of mechanical size effects (a benefit of *in situ* micro-mechanical testing in general, as it has been also performed with micro-tensile specimens [94]). Additionally, later mechanical data analysis is relatively easy, as the load and displacement data acquired can be easily converted to engineering stress and strain curves by normalizing the load

by cross-section area and the displacement by initial micro-pillars height, respectively. If protocols mentioned above are followed, representative yield stress data can be extracted.

2.3.2. Other micro-mechanical geometries

Prior to the present work, *in situ* micro-pillar compression was the only micro-mechanical geometry applied for deformation twinning studies in TWIP steels and CoCrNiFe HEA [69–72,95,96]. However, other established micro-mechanical geometries could be applied, such as micro-tensile, micro-cantilever or micro-shear, and, therefore, deformation twinning could be evaluated under different stress states.

Micro-tensile experiments are an interesting alternative to micro-pillars, as known constrains of micro-pillar applications are overcome by this geometry [94,97]. For instance, issues such as buckling that limits micro-pillar diameter-to-height aspect ratio, would be averted with micro-tensile specimens as high aspect ratios are possible. Higher aspect-ratio, i.e. greater specimen length, also aids in terms of constrains [94]. However, this type of specimen fabrication is time-consuming, which precludes this geometry from a wider use [86]. Within the scope of applying tensile stress for deformation twinning activation, one could think alternatively about the micro-cantilever geometry, as not only it is a specimen that is fabricated faster than a micro-tensile one, but also, the introduction of compressive stresses, allows investigation of anisotropy.

Contrary to micro-tensile tests, in a micro-cantilever bending test the specimen is subjected to an inhomogeneous stress distribution. A clear consequence of this stress gradient is the dislocation pile-up caused during deformation that affects the mechanical behavior of the tested beam, e.g. hardening [86]. As the dislocations approach the neutral fiber of the micro-cantilever, the inevitable transition in stress state occurs (tensile to compressive stresses) and the progressive reduction of the stress affects the dislocation motion leading to a dislocation pile-up (see Figure 2-10(b)) [98]. The dislocation pile-up generates back stresses, which can affect the operation of dislocation sources [99]. The stress gradient complicates mechanical data interpretation, i.e. correlation between acting stress and mechanism. This led this geometry to be applied mainly in plasticity if understanding influence of strain gradient is of interest [86], or for fracture toughness experiments [100].

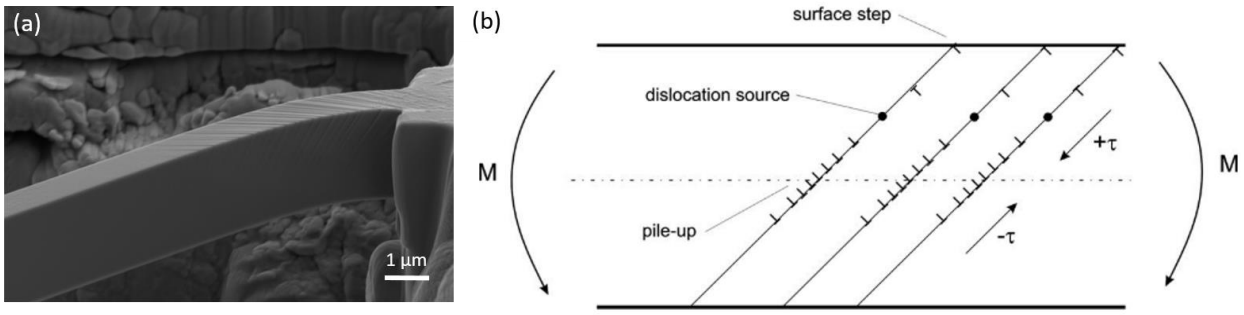

Figure 2-10 Micro-cantilever bending experiment: (a) *post mortem* SEM image and (b) dislocation pile-ups formed in micro-cantilever at the neutral fiber ((b) is reprinted from [98]).

An alternative testing geometry for deformation twinning studies would be the micro-shear geometry. This geometry is a macroscale experiment adaptation of the double shear creep specimen [101–103] and has been successfully applied in the micro scale for critical resolved shear stress (CRSS) assessment of specific slip systems in pure metals such as Cu [102,104], Au [103] and Mg [105]. This is due to its unique specimen geometry and crystallographic alignment, which allows the direct activation of a specific slip system by pure shear without constrains, as dislocations can freely glide through the shear zones [102,103]. It also represents a simple case of multiaxial loading ($\sigma_1 = -\sigma_3 \neq 0, \sigma_2 = 0$) (see Figure 2-11) [102].

It is important to note, however, that for a successful micro-shear experiment, aspect ratio dimensions should be followed as previously tested in [101] (see dimensions in Figure 2-11). Possible consequences are for instance: if the width (W) is increased to favor shear displacement, this leads to increase in superimposed bending stress; bending stress can then be reduced by increasing the height of the shear zone (H), which in turn will increase the force necessary to deform the specimen [103]. This way, experiments can be conducted with a homogenous shear stress state in 80% of the shear zone [103].

Moreover, this geometry has shown to be an effective micro-mechanical geometry, as it enables direct activation of a desired slip system (according to crystallographic alignment) [102–105], and previous experiments have also shown no change in slip geometry [102,103], as well as a good reproducibility in mechanical data [103].

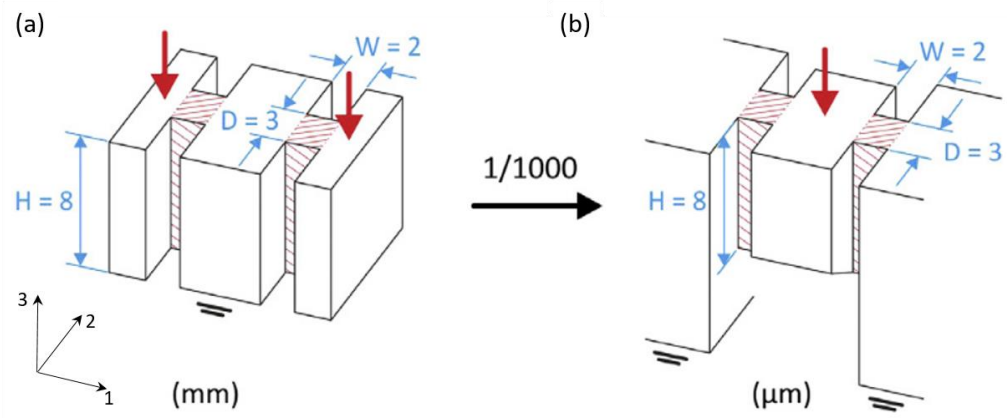

Figure 2-11 Representative drawing of the shear geometry with their dimension aspect ratio on the: (a) macro and (b) micro scale (modified from [103]).

2.3.3. Mechanical size-effect

Early micro-mechanical experiments already showed the "the smaller the stronger" trend, as the micron to nanoscale micro-pillars tested exhibited a significant increase in CRSS as diameter size decreased [7,89]. Following these initial reports, many studies were conducted to explain the origin of such behavior in small scale mechanics [94,106–115] and models were proposed, such as dislocation starvation [106,109], dislocation source truncation [110,111] and source exhaustion [112,115]. The dislocation starvation model proposes that initial mobile dislocations escape from free surface, resulting in a dislocation-starved state, which then require higher stresses for dislocation nucleation [106]. The truncated dislocation source model explains the observed increase in strength in small scale due to operation of single-arm sources, truncated at the surface and the stress for operation depends on its length [111]. And source exhaustion proposes that dislocation multiplication is slower than their escape [115].

Therefore, generally the size-dependence has been explained by the number and size of the dislocation sources [86]. Considering a sample volume reduction, a smaller number and size of dislocation sources is expected. Thus, such limited volume samples may or may not contain dislocations initially and their mechanical response will be greatly affected by that. If a sample is dislocation free, for instance, their strength could be comparable to the theoretical strength, reaching the so-called "whiskers-like" behavior; however, if such samples contain a few dislocation, the number and size of sources will determine their mechanical response, leading to a

stochastic behavior; and lastly, if samples size is increased, reaching to a large number of dislocations and sources, their mechanical behavior will be dominated by their collective response, reaching the so-called “bulk-like” behavior [86].

For the Cantor HEA, a mechanical size-effect has been reported for micro-pillars with compression axis on [5 1 3] [116], [11 3 5] [117], [1 0 1] [118,119] and on [1 2 6] and [1 2 3] [65], however full dislocation slip was predominantly observed. In these cases, the size scaling exponent reported either smaller or closer to the lower bound compared to values obtained for other FCC metals, which typically ranges between -0.6 and -1.1 [70,89,120], while obtained values were -0.32 [117] (see Figure 2-12(a)), -0.53 [116] and -0.63 [65]. It has been suggested that the smaller size scaling exponent indicated a more dominant role of high lattice friction or solid solution hardening as strengthening mechanisms [116,117].

Mechanical size effect was also study for the CoCrFeNi HEA, through micro-pillar compression, comparing mechanical response of three different orientation (see Figure 2-12(b)) [96]. In this study, a slightly smaller size scaling exponent for the micro-pillars that deformed by deformation twinning was obtained, -0.32, compared to -0.56 and -0.61 for samples that deformed by dislocation slip, oriented for ⟨110⟩ and ⟨111⟩ respectively [96]. Molecular dynamics simulation performed attributed such differences to initiation of the twinning process by emission of partial dislocations from initial dislocations or free surface sources, which induces a weaker size effect [96].

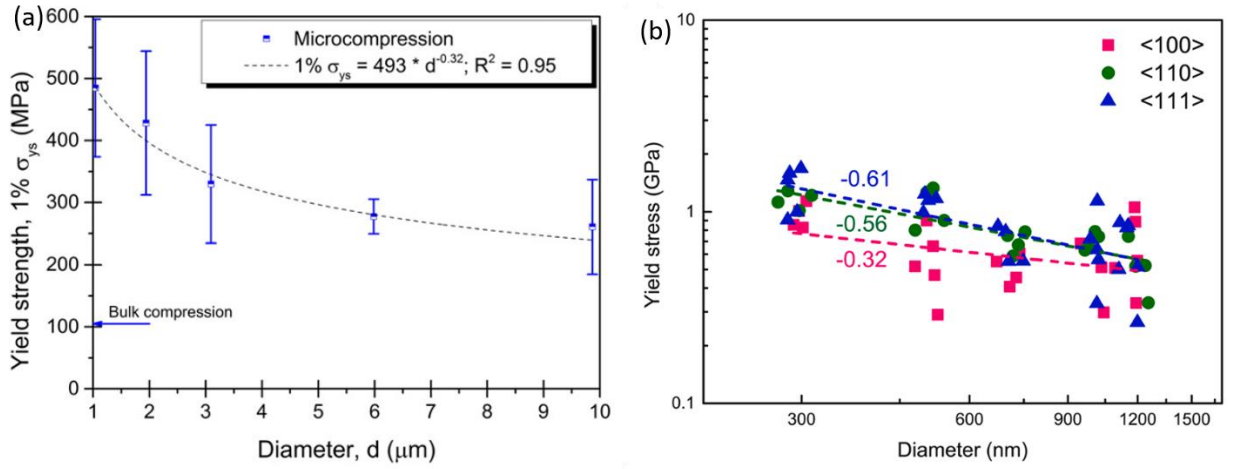

Figure 2-12 Size-effect plots for HEAs: (a) Cantor alloy oriented for full dislocation slip ([11 3 5]) and (b) CoCrFeNi in different orientations ⟨110⟩, ⟨111⟩ and ⟨100⟩, which favor deformation twinning activation ((a) is reprinted from [117] and (b) is reprinted from [96]).

However, so far, there are no *in situ* SEM experimental reports on the Cantor alloy that thoroughly investigates how different stress levels might influence deformation twinning in terms of mechanism. This is discussed on the Chapter 5, which comprises an in-depth analysis that include: (i) deformation twinning activation, e.g. estimation of twinning stress; (ii) stress analyses with mechanical size-effect observations on twinning stress and how it compares to dislocation slip; and with this knowledge, (iii) investigate the twinning mechanism and potential differences under different stress levels and dislocation population, evaluating previously proposed mechanisms, i.e. insights into the underlying mechanism.

Shining light on this knowledge gap is the main aim of this thesis. Therefore, in this work quantitative stress analysis combined with advanced microstructure characterization are applied to obtain insights into detailed dislocation mechanisms of twin nucleation and growth for FCC HEAs. Here, *in situ* micro-pillar compression experiments are performed varying micro-pillar diameters, therefore, different stress levels are applied. This provides relevant information on critical stresses for twin nucleation and, through microstructural investigations, changes in twin structure can be observed. With that, valuable insights for a mechanism-based development of advanced HEAs are obtained.

3. Materials and methods

3.1. Bulk sample preparation

The Cantor alloy samples used in this PhD work were provided by collaborators at the Karlsruhe Institute of Technology [121]. Further details on the fabrication process as summarized below can be found in detail in the following references [121,122].

An arc melting furnace was used to produce the equiatomic CoCrFeMnNi HEA (Cantor alloy) bulk sample. The sample was fabricated under Ar atmosphere using highly pure elements (99.95+%). After melting, a water-cooled Cu mold was used to cast rod-shaped ingots. To analyze the resultant chemical composition, an inductively coupled plasma optical emission spectrometry was applied. The samples chemical composition was confirmed to be: 20.4 at.% Co, 19.7 at.% Cr, 20.3 at.% Fe, 19.2 at.% Mn and 20.4 at.% Ni (accuracy of 0.1 at.%) [121]. The as-cast ingots underwent homogenization heat treatment, sealed in a glass tube, at 1473 K for 72 hours followed by water quenching. The ingot diameter size was reduced from 14 mm to 6 mm by rotary swaging. Then, to obtain a fully recrystallized microstructure, annealing was done at 1273 K for 1 hour, which resulted in a grain size around 60 μm [122].

Before preparing specimens for micromechanical testing using FIB, 1 mm thick pieces were cut with a diamond saw and metallographically prepared to obtain a deformation-free surface. This metallographic preparation consisted of gradually increasing grinding steps up to 2500 mesh followed by polishing steps of firstly with diamond suspension of 3 μm and 1 μm, and finished with oxide polishing suspension (0.02 μm particle size).

3.2. Fabrication of samples for micromechanical testing

Ga FIB milling was applied for fabricating samples for mechanical testing at the micron scale including micro-pillar compression, micro-cantilever bending and micro-shear tests. All FIB sample preparation were carried out in a Zeiss Crossbeam 550L and all EBSD analyses were performed with a Symmetry S2 (Oxford Instruments) in the same FIB-SEM (Crossbeam 550L, Zeiss).

Deformation twinning in FCC metals/alloys is crystallographic orientation dependent (see Section 2.2, page 9). Which means that for a given crystallographic orientation, deformation twinning will be triggered either by tensile stresses or compressive stresses. Therefore, the goal in both cases is to maximize the resolved shear stress on the leading partial dislocation, which promotes twinning by extension of the stacking fault between the two partial dislocations [69,70]. In this work, to activate deformation twinning during test, samples were milled in specific grain orientations, according to the expected stress state, carefully calculated by EBSD analyses. EBSD analysis is explained in detail on Section 3.4.

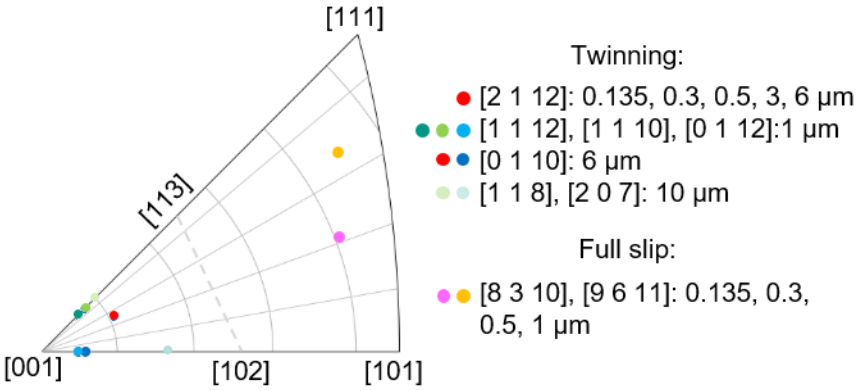

Figure 3-1 Inverse pole figure (IPF) in compression direction showing crystallographic orientation of the micro-pillars tested and respective diameter size (reprinted from supplementary documents of paper [9]).

For the micro-pillar compression tests, all specimens were cut from a polycrystalline bulk piece, in the middle region of the desired grain to avoid grain boundaries, resulting in single crystal micro-pillars. Two subsets of pillars were tested, which included loading direction oriented for full dislocation slip and deformation twinning activation (summarized in Figure 3-1). The subset that favored deformation twinning activation were oriented on [2 1 12], [1 1 12], [0 1 10], [1 1 8] and [2 0 7]. And the subset for full dislocation slip activation were oriented on: [8 3 10] and [9 6 11]. The grains crystallographic orientation was carefully selected by using EBSD. Micro-pillars were machined using the FIB with an acceleration voltage of 30 kV and currents varying

from 65 nA, for coarse milling, to 10 pA, for fine milling, according to their size. Top diameter of the pillars ranged from 0.14 μm to 10 μm, maintaining an aspect-ratio diameter-to-height of 1:2-3 to avoid buckling. In Table 3-1 the currents used for each milling step and corresponding micro-pillar diameter is described. In Chapter 4, only micro-pillars of loading orientation [1 1 10] and [2 1 12] with 0.5 μm and 1 μm diameter were considered. In Chapter 5, all micro-pillar sizes were considered, including the ones oriented for full dislocation slip, which enabled the mechanical size effect comparison (Figure 3-1). Overall, at least 3 micro-pillars were tested for each diameter which makes a total of 22 micro-pillars oriented for deformation twinning activation and 55 micro-pillars oriented for full dislocation slip.

Table 3-1 FIB parameters used on the Nano Patterning and Visualization Engine (NPVE) (Zeiss) in each milling step for the corresponding micro-pillar diameter.

Diameter (μm)	Milling step	Voltage (kV)	Current (nA)	Overlap	Orientation
10	Coarse	30	65	50% - 50%	Alternating
	Medium		7	50% - 50%	Alternating
	Fine		0.7	75% - 75%	Out – in
6	Coarse	30	30	50% - 50%	Alternating
	Medium		7	50% - 50%	Alternating
	Fine		0.7	75% - 75%	Out – in
3	Coarse	30	30	50% - 50%	Alternating
	Medium		1.5	50% - 50%	Alternating
	Fine		0.7	75% - 75%	Out – in
1	Coarse	30	1.5	50% - 50%	Alternating
	Medium		0.7	50% - 50%	Alternating
	Fine		0.3	75% - 75%	Out – in
0.5	Coarse	30	1.5	50% - 50%	Alternating
	Medium		0.7	50% - 50%	Alternating
	Fine		0.05	75% - 75%	Out – in
0.3	Coarse	-	-	-	-
	Medium	30	0.3	50% - 50%	Alternating
	Fine		0.05	75% - 75%	Out - in
0.14	Coarse	-	-	-	-
	Medium	30	0.05	50% - 50%	Alternating
	Fine		0.01	75% - 75%	Out - in

Please note that, in Chapter 5, for simplicity, the micro-pillar's orientation, which are aligned for deformation twinning activation, are compiled to [1 1 10] loading direction. Most pillars, despite variation in in-plane orientation, deviate less than 5 degrees from the [1 1 10], with the exception of one 10 μm diameter which was cut on a [2 0 7] grain.

Contrary to micro-pillars, a micro-shear specimen requires a precise alignment geometrically with respect to the crystallographic orientation in both, the in-plane and the loading directions (Figure *3-2* (a) and (b)). In terms of in-plane alignment, to activate mechanical twinning the ligament-normal direction should correspond to the twinning plane $\{111\}$, while the loading direction should be aligned to one of the three $\langle 112 \rangle$ twinning direction. Considering that the sample used in this work was polycrystalline and an undercut needed to be performed, once the $[112]$ (surface-normal direction) grain was chosen and correctly aligned transverse direction (TD) to $(11\bar{1})$ plane, a large cut was done to expose the desired grain. Since a large material needed to be removed, this cut was performed with femtosecond laser ablation, using the same Zeiss Crossbeam 550L. Specimens were then micro machined using the FIB with an acceleration voltage of 30 kV and currents starting with 3 nA for coarse, 700 pA for intermediate and 50 pA for fine milling. Sample dimensions were based on literature [102,103,105] keeping the same aspect ratio with D = 500 nm, W = 750 nm, and H = 3 μm.

In the micro-cantilever case, the selected orientation was with a TD close to a $\langle 111 \rangle$. Five micro-cantilevers were prepared from three different grains of which TD orientation is $[3\bar{1}\bar{2}]$, $[1\bar{3}\bar{2}]$ and $[11\bar{1}]$, respectively. As shown in Figure 3-2 (c), micro-cantilevers with dimensions of $W = b$ = 2 μm and L = 10 μm were then micro machined in the same FIB operated at 30 kV using ion beam currents of 3 nA for coarse, 700 pA for intermediate and 50 pA for fine milling.

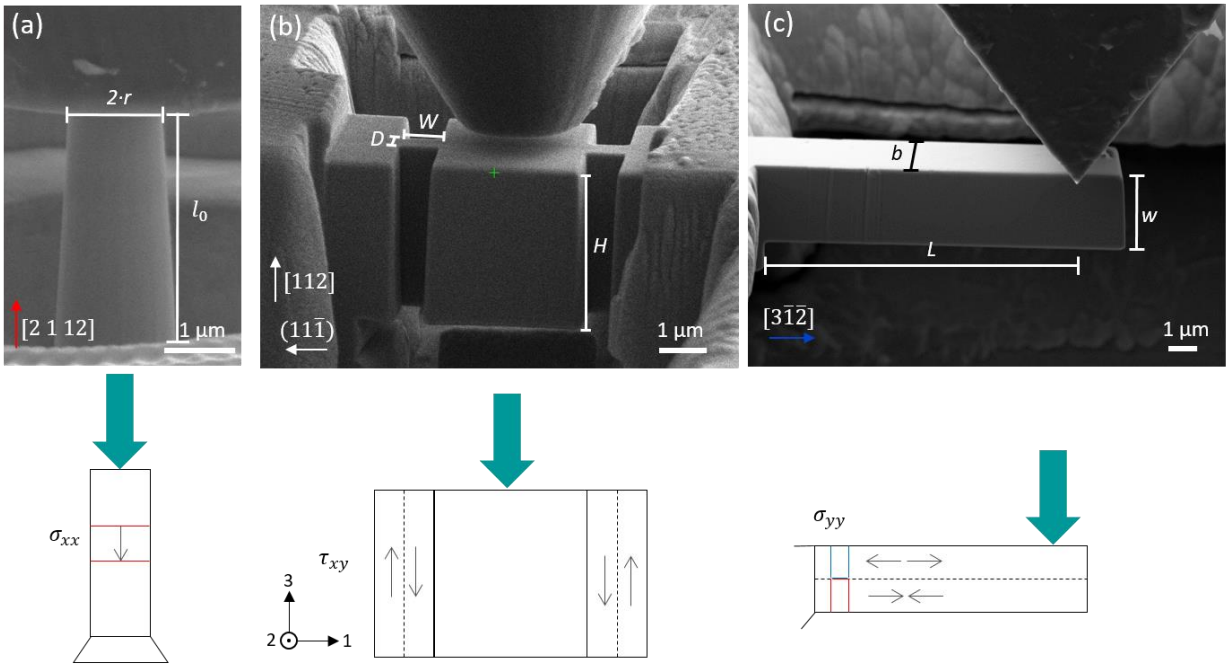

Figure 3-2 *In situ* SEM micromechanical testing representation and relevant measurements, and respective schematic drawing of internal stress state (represented by the arrow) within the cross-section of each micro mechanical geometries applied to measure twinning stress: (a) micro-shear, (b) micro-pillar compression and (c) micro-cantilever bending test (modified from [8]).

3.3. *In situ* SEM micro-mechanical testing set up

All *in situ* micro mechanical testing were performed in a SEM (Merlin Gemini II, Zeiss) with a Hysitron PI89 SEM Picoindenter (Bruker). Most of the tests were conducted with the load transducer of maximum force of 0.5 N and noise floor of 5 µN (high load transducer), except for micro-pillars with diameter below 1 µm. Due to the nanoscale size and lower forces expected, a high resolution load transducer (low load transducer) was used that had a maximum load of 10 mN and a noise floor of 0.4 µN. And all tests were performed in displacement control mode.

3.3.1. Micro-pillar compression test

The indenter was equipped with a diamond flat punch tip (Synthon-MDP AG) with diameter varying depending on the micro-pillar size from 2 µm up to 20 µm. All tests were performed with

a strain rate of $10^{-2}\ s^{-1}$ and maximum strain around 8%. The mechanical data acquired from testing were load and displacement curve, which were later converted to engineering stress (σ_{eng}) and strain (ε) curve with the following equations:

$$\sigma_{eng} = P/\pi r^2 \tag{1}$$

$$\varepsilon = \Delta l/l_0 \tag{2}$$

where *P* is the load applied, *r* is the radius of the micro-pillar's top, Δl is the displacement applied and l_0 is the micro-pillar's height. With that the critical resolved shear stress ($\tau_{2\%}$) was calculated by

$$\tau_{2\%} = \sigma_{2\%} \cdot m \tag{3}$$

where *m* is the Schmid factor and $\sigma_{2\%}$ the yield stress taken with a 2% strain offset using a virtual unloading slope.

3.3.2. Micro-shear test

The indenter was equipped with a 2 µm diamond flat punch tip (Synthon-MDP AG). All tests were conducted with a displacement rate of 10 nm/s. Engineering shear stress (τ_{eng}) and shear strain (γ) were calculated according to equations respectively:

$$\tau_{eng} = P/2 \cdot H \cdot D \tag{4}$$

$$\gamma = \Delta/W \tag{5}$$

where *P* is the load and *Δ* is the displacement applied, *W* is the width, *D* is the thickness and *H* is the height of the shear ligaments.

3.3.3. Micro-cantilever bending test

The indenter was equipped with a 10 µm diamond wedge tip (Synthon-MDP AG) and displacement rate of 10 nm/s was used. For the micro-cantilever, tensile stress (σ) at the top surface was calculated with an assumption of fully plastic deformation, using by the equation:

$$\sigma = 4 \cdot P \cdot L/b \cdot w^2 \quad (6)$$

where P is the applied load, L is the length, b the width and w the thickness of the cantilever.

3.4. *Post mortem* analysis

3.4.1. Crystal orientation analysis using EBSD

Electron backscattered diffraction (EBSD) orientation analysis were carried out for two purposes: (i) firstly to identify potential grains with the desired crystallographic orientation to activate twinning and, (ii) to identify if deformation twinning was activated during *post mortem* analysis. The EBSD parameters used were as follows: for grain selection, the same parameters were used for all testing geometries, the acceleration voltage was maintained on 20 kV and the current was 8 nA; and for the *post mortem* analyses, there was a variation of the parameter to obtain the optimum resolution to resolve the nanoscale twin lamellas. In this case, the acceleration voltage varied from 20 kV to 30 kV and the current from 2 nA to 8 nA.

3.4.2. Slip system analyses for micro-pillars

To allow an easy correlation between Euler angles and in-plane orientation with slip system analyses, EBSD maps and *post mortem* SEM imaging were always taken with the same horizontal alignment. To guarantee that, prior to any analyses, a cross mark was cut with FIB in the sample's surface (see Figure 3-3(a)). With that, the same in-plane orientation could be easily achieved prior to SEM imaging, as the longer cross mark was always aligned horizontally parallel to the imaging axis. In addition to that, a MatLab script was used to calculate the Schmid factors based on Euler angles (obtained with EBSD analyses), which aided the selection of grains that would favor twinning. A Mathematica script previously developed was applied for slip system analyses. The script uses the Euler angles (of the particular grain) to simulate the expected slip systems, generating a pillar image with the slip traces inside (see Figure 3-3(c)). Then the simulated slip systems within the pillar were compared with the *post mortem* SEM images of the micro-pillars side (see Figure 3-3(b)) and top surface, and this way the slip system was identified.

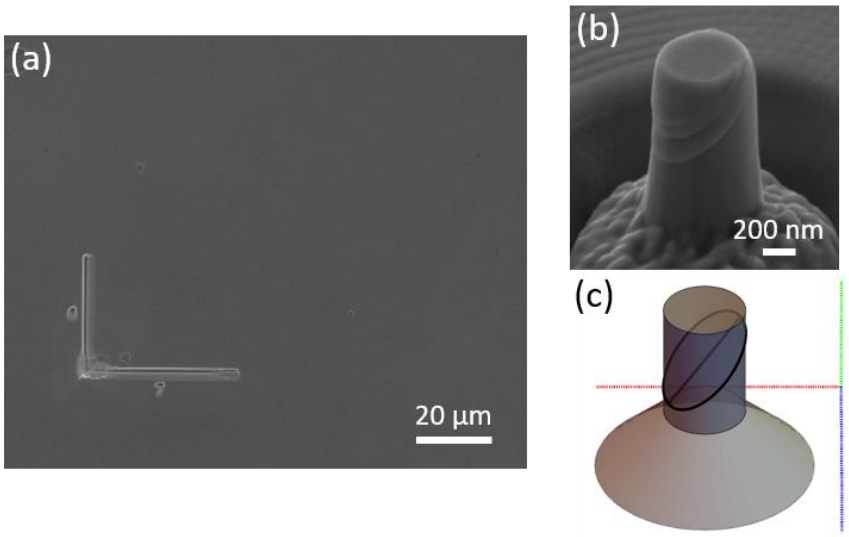

Figure 3-3 Overview of how the slip system analysis were performed: (a) a representation of the cross mark cut with FIB in every bulk samples to guarantee constant in-plane orientation which facilitates slip system analyses, (b) *post mortem* SEM image of the micro-pillars side view and (c) the simulated slip system used for comparison with (b) to identify the slip system activated.

3.4.3. BSE cross-section imaging for micro-pillars

Besides EBSD, cross-section imaging with the back-scattered electron (BSE) detector was also applied to verify if twinning was activated or not. This step was necessary due to the EBSD's limited spatial resolution, which was unable to resolve the nano scale twin lamellas formed, i.e. mostly in micro-pillars below 1 µm, but also, it cannot accurately confirm the absence of twinning. To enable the cross-section imaging, cross-section cut was performed with FIB-SEM, approximately one third to half of the micro-pillar in diameter, with an acceleration voltage of 30 kV and, depending on the size, a coarse milling with a current of 1.5 nA (sub 1 µm micro-pillar coarse step was skipped) followed by a polishing step with 50 nA to 10 nA. SEM images were then taken with an acceleration voltage of 10 kV and a current of 2 nA.

3.4.4. TEM analyses performed on micro-pillars

TEM investigations were also performed to confirm twinning activation, as well as, study the possible twinning mechanism. In this case, four samples were prepared, one for each diameter

from 1 µm to 10 µm. Selected micro-pillars were lifted out and glued on a copper grid using a FIB. Then platinum was deposited to protect the pillar from over-fibbing, and the top surface from FIB damage. To obtain the ideal thickness for TEM analyses (around 100 nm), the following milling steps were done: (i) coarse to fine milling with acceleration voltage of 30 kV, starting with a current of 300 pA until 500 nm, 100 pA until 200 nm and 20 pA until an approximate 100 nm thickness was reached; then (ii) a final milling step for cleaning with acceleration voltage of 2 kV and current of 10 pA. TEM bright field (BF) and dark field (DF) micrographs were acquired with an aberration-corrected TEM (Titan Themis 300, ThermoFischer) with an acceleration voltage of 300 kV.

To obtain the BF and DF image, the FIB samples are first tilted to a low-order zone axis. The region of interest is isolated by introducing the selected area diffraction (SAD). Next, the sample is tilted to achieve the two-beam condition by aligning with the Kikuchi lines from the desired diffraction spot, from which the dark field image will be acquired. In the two-beam condition, only one diffraction beam (other than the direct beam) is strongly diffracted. By placing the aperture at the direct beam, allowing it to pass, a BF image will be formed on the image plane. In this configuration, only electrons from the direct beams, contribute to the image. To obtain the centered DF image, the sample is tilted so that the direct beam is blocked by the objective aperture, and the diffracted beam is centered on the image plane. This results in an image where the regions that appear black correspond to the areas where the primary (direct) electron beam passes straight through the sample, while the diffracted electrons contribute to the contrast.

4. Quantitative measurement of twinning stress using various geometries

Chapter 4 is based on a published manuscript:

C.A. Teixeira, S. Lee, C. Kirchlechner, Measuring the twinning stress at the micron scale: A comprehensive comparison of testing geometries, Mater. Charact. 217 (2024) 114314. https://doi.org/10.1016/j.matchar.2024.114314.

The authors have agreed to have this manuscript as the Chapter 4 of this thesis. Each author contribution to the original manuscript can be found in detail in the Appendix, page 89.

4.1. Introduction

Deformation twinning is often attributed to the improvement of mechanical properties, for instance increase in tensile strength and ductility particularly of HEAs [3–6]. Furthermore, twinning is believed to be stress-controlled, thus a particular stress should be reached for twin formation, which is called the twinning stress. A thorough understanding of the deformation mechanism, including measuring the twinning stress, is crucial for advanced HEAs design. In this regard, there have been attempts to measure the twinning stress, which mainly consisted in interrupted mechanical test performed in bulk scale samples [4,53,55,56,60]. Such type of measurements is affected by the local microstructure that results in stress heterogeneities and, in consequence, fails to provide the twinning stress quantitatively.

To overcome that, *in situ* micro-mechanical testing is a valuable tool allowing stress measurements to be conducted locally, which enables underlying mechanisms to be investigated as well. Among the existing micro-mechanical geometries, the micro-pillar is the most applied so far, including in deformation twinning investigations [69–72,95,96]. However, there are other established micro-mechanical geometries that could be used as alternatives to measure twinning stress, such as micro-shear and micro-cantilever (see Chapter 2). Therefore, in this chapter the aim is to investigate and compare three different micro mechanical geometries for quantifying twinning stress in HEAs: micro-shear, micro-pillar and micro-cantilever. In this comprehensive comparison, it will determine which micro-mechanical geometry is best suited to measure the twinning stress as well as investigate the twinning mechanism.

4.2. Results

4.2.1. Micro-shear test

The beauty of a micro-shear experiment is the ability to directly activate a specific slip system by applying pure shear deformation. This occurs due to its unique geometry allied to perfect in-plane alignment, which is a simple case of multiaxial loading condition ($\sigma_1 = \sigma_3 \neq 0, \sigma_2 = 0$) [103]. A micro-shear specimen is composed by: (i) the central block, which one could refer as the loading block as it is the position load is applied with the indenter tip, and (ii) two ligaments (geometry commonly referred as double shear), which is the two regions that undergoes shearing during test, therefore the region of interest (see Figure 3-2(b)). During a micro-shear test, loading is applied on the central block and, if the in-plane alignment is properly done, shearing of a $\{111\}$ plane in both ligaments will be observed parallel to the loading direction. With that, the activation of the aligned slip system is caused by pure shear. For deformation twinning to occur, the specimen should be aligned in-plane TD in a $\{111\}$ plane, and the loading direction to a $\langle 112 \rangle$ twinning direction, as observed in Figure 3-2 to apply maximum shear stress to twinning partial dislocations.

The samples were aligned in the $(11\bar{1})$ in-plane TD and the $[112]$ twinning loading direction, and an overview of the experiment is seen in Figure 4-1. During the micro-shear experiments, a shear stress plateau of around 300 MPa is reached (see Figure 4-1(a)). This value is slightly higher than the previously reported in literature of around 240 MPa [4,59]. In the present experiment, four specimens were tested, which resulted in an average plateau stress or CRSS of 339 ± 16 MPa. A good in-plane alignment is observed as shearing on the $(11\bar{1})$ plane is parallel to the loading direction. An indenter imprint can be observed on the top surface of the center block, suggesting some plastic deformation took place during initial loading prior to sliding of both ligaments (see Figure 4-1(b)). However, based on shallow imprint, it is reasonable to assume that the contribution from the plastic deformation on the center block to the overall plastic flow of the sample is negligible.

To identify if deformation twinning occurred, EBSD analysis was performed in both ligaments, which are referred as “L” and “R” after deformation (see Figure 4-1(b) and (c)). Prior the EBSD mapping, the specimens’ top surface layer was cut by FIB, around 1.5 µm thick, to ensure a flat top surface and to avoid shadowing on the EBSD detector. For the shear region “L”, nanoscale twin lamellas were observed, confirmed not only by the difference in crystallographic orientation

with the 60 degrees misorientation, but also [111] pole figure of twinned region and matrix, which shares one common pole corresponding to the twin plane (see Figure 4-1(c)).

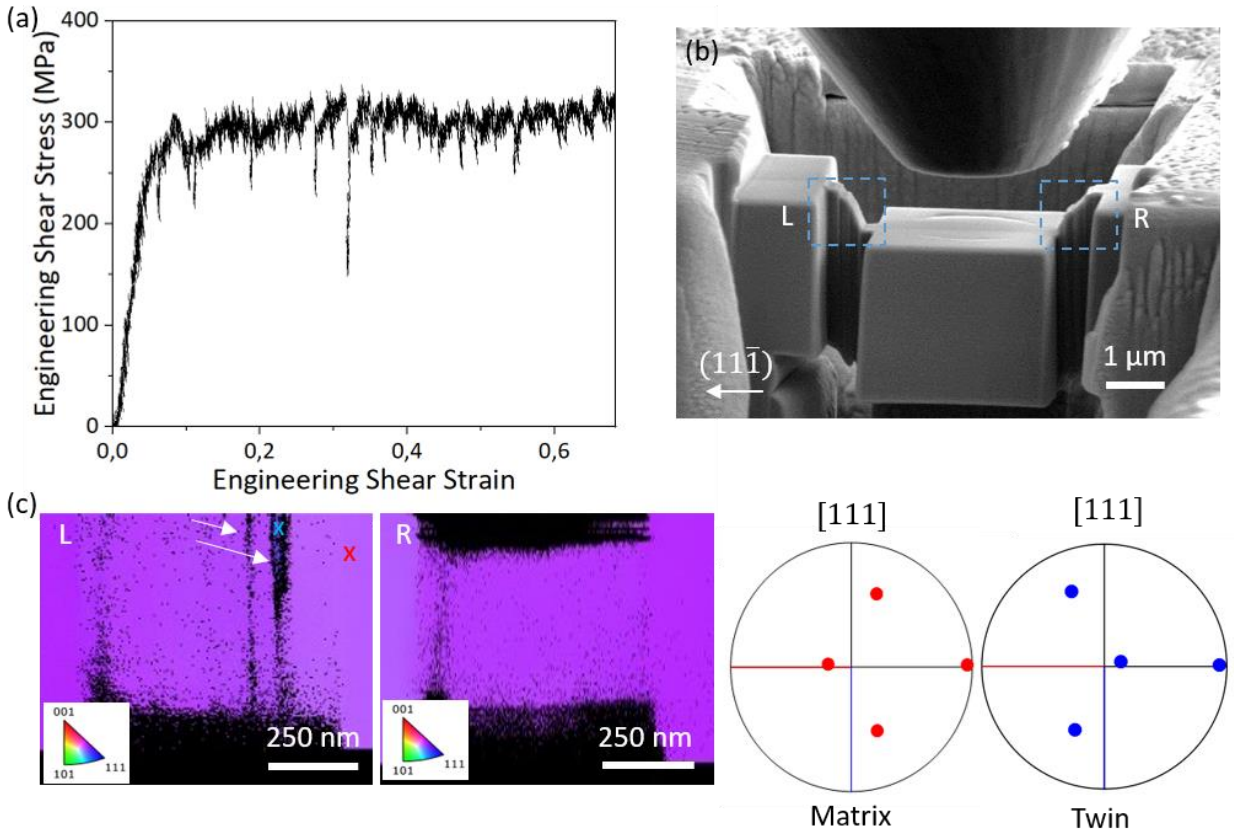

Figure 4-1 Overview of a micro-shear experiment followed by *post mortem* analysis for identification of deformation twinning: (a) a representative engineering stress and strain curve, (b) a *post mortem* SEM image, (c) EBSD analysis with IPF-Z of regions "L" and "R" seen in (b) and [111] pole figures of the twin and matrix taken from the regions indicated by the "x"s (reprinted from [8]).

Contrary to that, no twin lamella was observed for the "R" ligament from the EBSD mapping. This can be explained by the opposing shear direction in both ligaments, as deformation twinning is polarized, meaning no twin formation is triggered if shear direction opposes the twinning direction (see Figure 3-2(b)) [51]. Which, for instance, also explains the tension-compression asymmetry

observed in deformation twinning [51]. Therefore, in one of the ligaments deformation twinning would not be observed, as the imposed shear direction will always be contrary to twin formation.

The micro-shear geometry allows to compute the contribution of deformation twinning to overall shear strain. For that, firstly the twin displacement was calculated considering the known crystallographic orientation relation between matrix and twin, and the twin thickness that can be measured from SEM imaging via EBSD. Then, this value was divided by the total displacement applied in each micro-shear sample. The shear displacement caused by deformation twinning was in average 18 nm and the total displacement applied reached in average 852 nm, this led to a contribution of 2.1 % of the overall shear strain. Although this estimated twinning contribution can be considered the lower bound, as the resolution limit of the EBSD might not have resolved the nanoscale twins formed, clearly dislocation slip is the main contributor to shear deformation.

4.2.2. Micro-pillar compression test

As described in Chapter 3.2, deformation twinning, under compression, is expected to form near a ⟨001⟩ crystallographic orientation, as the leading partial dislocation has the highest Schmid factor. In this condition, the resolved shear stresses are maximized on the leading partial dislocation and an extension of the stacking fault occurs during applied load, resulting in deformation twinning [69,70]. In this Chapter only micro-pillars of 0.5 μm and 1 μm were considered, this way the characteristic lengths of each geometry would be similar and, therefore, this allows a comparison between the other testing geometries. And 3 specimens were tested in each case.

One very attractive feature of a micro-pillar experiment is the ease in mechanical data interpretation; by simply normalizing the load-displacement curve with the micro-pillar's area and height, the initial data is converted to the engineering stress-strain curve (see Figure 4-2(a)). Multiple slip was likely to occur for the micro-pillars tested, as their loading direction was near a ⟨001⟩ crystallographic orientation, therefore there are multiple slip systems with Schmid factor similar (as seen in Figure 4-2(b)). SEM imaging allowed the slip planes to be identified, therefore, the upper plane corresponds to the $(\bar{1}11)$ and the lower plane is the $(1\bar{1}1)$. In this case, to trigger deformation twinning, there are only two possible twinning direction (with highest Schmid factor)

and, therefore, the possible slip systems would be: $(\bar{1}11)[\bar{1}1\bar{2}]$ and $(1\bar{1}1)[1\bar{1}\bar{2}]$. To confirm the slip system observed, EBSD analyses and SEM cross-section imaging with BSE detector were performed. The *post mortem* analyses confirmed the $(\bar{1}11)[\bar{1}1\bar{2}]$ slip system, which has a Schmid factor of 0.46. As a result, CRSS calculated was 294 ± 46 MPa, with the yield stress taken with a 2 % offset. As the micro-pillar size reduced to 0.5 µm diameter a CRSS of 425 ± 197 MPa was calculated. The increase in yield stress and large standard deviation is expected, as the mechanical size-effect leads to a stochastic behavior [86].

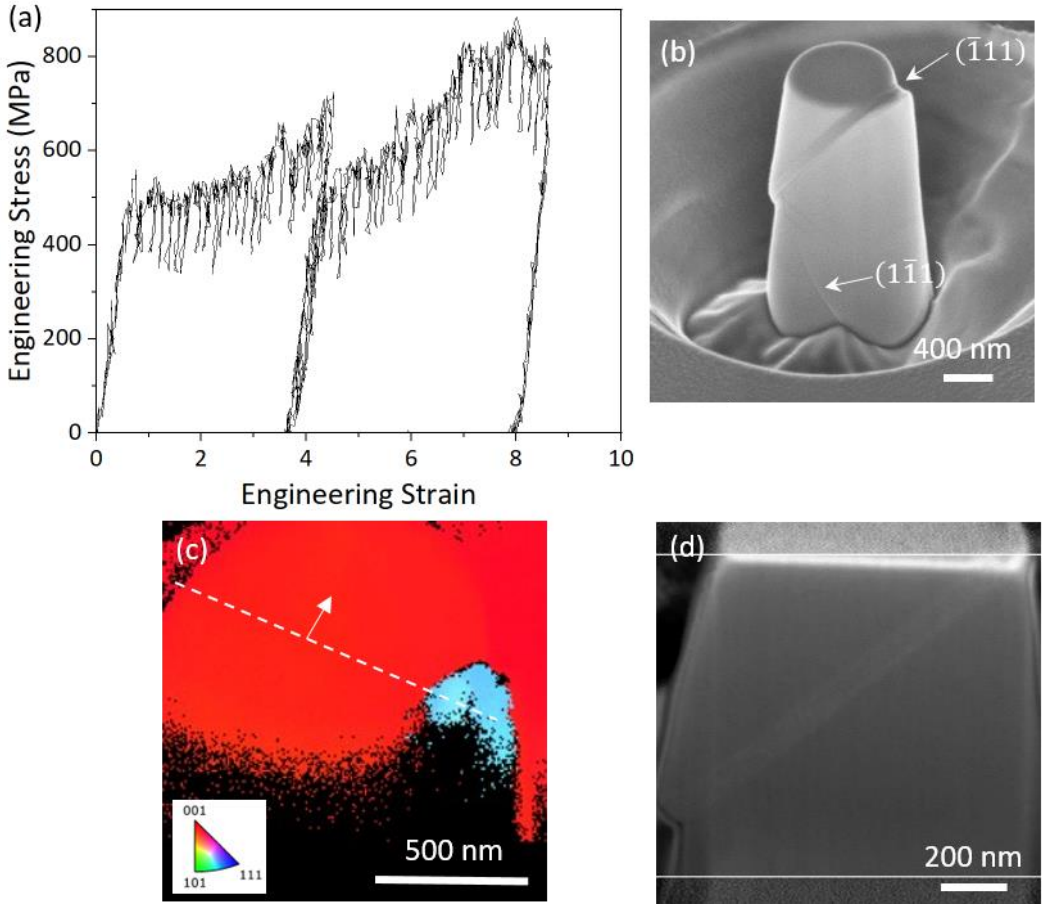

Figure 4-2 Overview of a micro-pillar compression experiment followed by *post mortem* analysis for deformation twinning identification: (a) representative engineering stress and strain curve, (b) *post mortem* SEM image, (c) micro-pillar's (b) top surface EBSD IPF-Z analyses and (d) cross-section SEM image with BSE detector, note the arrow on (c) highlights the point of view in (d) (reprinted from [8]).

4.2.3. Micro-cantilever bending test

For the micro-cantilevers, the in-plane orientation of the sample was selected to promote deformation twinning in the upper half of the cantilever, as this simplifies *post mortem* analyses with EBSD mapping on the top surface. With that in mind, 3 specimens were aligned in a $\langle 123 \rangle$ TD and 2 in a $\langle 111 \rangle$ TD, which means in the long cantilever axis. In this conditions, a multiple slip is expected for cantilevers aligned to a $\langle 111 \rangle$ TD, with 3 possible twinning directions, and single slip for the ones aligned to a $\langle 123 \rangle$ TD, as the Schmid factor for the leading partial dislocation is maximized.

The first micro-cantilever tested was orientated along $[3\bar{1}\bar{2}]$ in TD. Based on Schmid factor calculations, single slip activation was predicted either full dislocation slip in $(11\bar{1})[1\bar{1}0]$ or $(11\bar{1})[\bar{1}21]$ twinning direction, with Schmid factor value of 0.46 and 0.47 respectively (Figure 4-3). However, SEM *post mortem* analyses (Figure 4-3(b)) showed two slip planes, the $(11\bar{1})$ and $(1\bar{1}\bar{1})$. In this case, the secondary slip system activated is most likely due to strain concentration near the cantilever's base, as this specimen had the highest displacement applied of around 3.5 μm. EBSD analyses confirmed deformation twinning in the $(1\bar{1}\bar{1})$ slip plane with a $[\bar{1}\bar{2}1]$ (Figure 4-3(c)), considering the highest Schmid factor. The calculated Schmid factor was 0.30 (for the $(1\bar{1}\bar{1})[\bar{1}\bar{2}1]$ twinning system), thus the CRSS was 237 MPa. Note that it is assumed for CRSS calculations the fully plastic condition and pure tensile stresses for all cantilevers.

Two other micro-cantilevers were tested in the $[\bar{1}\bar{3}2]$ TD, but interestingly deformation twinning was not observed in EBSD analyses. Although orientations are similar to the previous $[3\bar{1}\bar{2}]$ TD cantilever, there was a lower total displacement applied for the $[\bar{1}\bar{3}2]$ TD. This variation in displacement ranged from 0.5 μm to 1 μm. As a result, no secondary slip plane was observed and only full dislocation slip on $(1\bar{1}1)[110]$ slip system with a Schmid factor of 0.46.

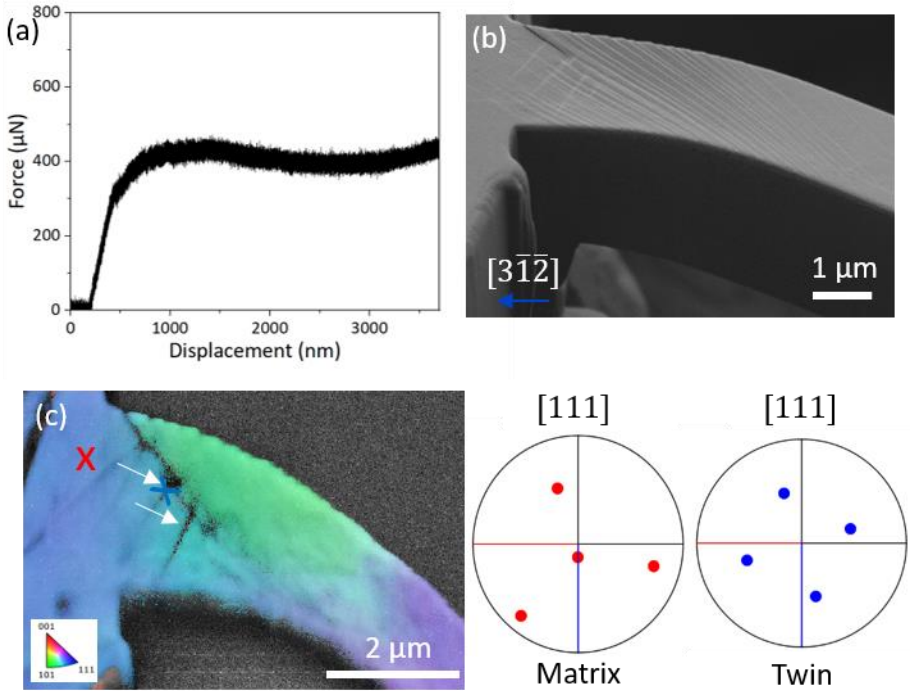

Figure 4-3 Overview of the micro-cantilever experiments followed by *post mortem* analysis for deformation twinning on the [3$\bar{1}\bar{2}$] TD: (a) the force and displacement curve, (b) the *post mortem* SEM imaging and (c) IPF-Z EBSD analyses and [111] IPF of the matrix and twin taken from the regions indicated by the "x"s (reprinted from [8]).

For the two micro-cantilevers aligned along [11$\bar{1}$] in TD (Figure 4-4), multiple slip system was observed. Given that the Schmid factors calculated were the same for the 6 predicted slip system, it was expected that more than one slip system would be activated in this case. However, SEM *post mortem* analyses showed that one of the cantilevers had two slip planes activated and the other three. Note that there was a difference in maximum displacements between them, one displacement of 1 μm and the other 2 μm, respectively (Figure 4-4(b)). EBSD analyses (Figure 4-4(c)) confirmed that twin lamella was only observed in the cantilever with the largest displacement (2 μm) and 3 slip planes activated. Therefore, the (111)[11$\bar{2}$] twinning system was activated with a Schmid factor of 0.31 and in the case of full dislocation slip a Schmid factor of 0.27. Overall, deformation twinning was observed in 2 out of 5 micro-cantilevers, thus the average CRSS for deformation twinning was 301 ± 63 MPa and, when no twins were observed, was 292 ± 26 MPa.

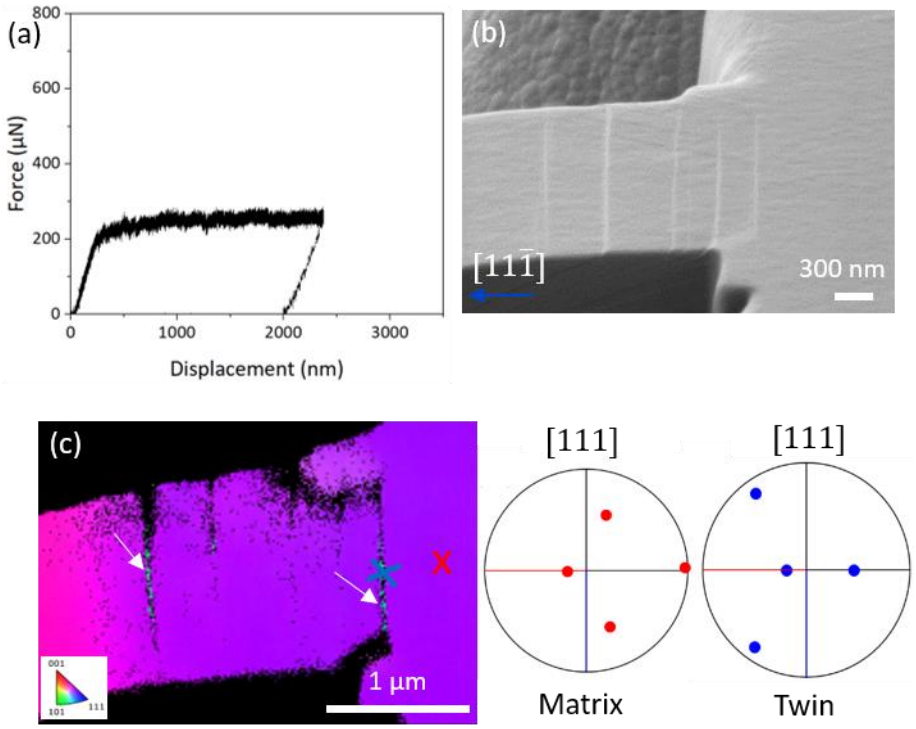

Figure 4-4 Overview of the micro-cantilever experiments followed by *post mortem* analysis for deformation twinning on the [11$\bar{1}$] TD: (a) the force and displacement curve, (b) the *post mortem* SEM imaging and (c) IPF-Z EBSD analyses and [111] IPF of the matrix and twin taken from the regions indicated by the "x"s (reprinted from [8]).

Deformation twinning is believed in literature to be a stress-controlled mechanism, however, the current results conflicts with that assumption, considering the cantilevers of same orientation and the stresses that were reached during test. These observations suggest that additional criteria would be required for deformation twinning to nucleate. Two hypotheses could be considered in this case: (i) the stress concentration near the cantilever base and (ii) the opposing shear stress sign. In the first case, the difference in displacement applied (2 μm to 3.5 μm) could have resulted in a higher stress concentration (for the latter) near the cantilever base enabling twining to occur, which was not observed for the other three cantilevers as this particular stress was not reached. In the second, the same explanation as previously mentioned in Section 4.2.1 would apply for at least one of the cantilevers in both [11$\bar{1}$] and [$\bar{1}\bar{3}$2] orientations. The absence of twinning could be a result of the cantilevers being arranged one in front of the other, within the same grain. This way, the shear

stress would be opposite in identical slip planes on opposite cantilever, therefore, in one condition twinning would be favored and in the other suppressed, even if the critical stress for twinning was reached.

4.3. Comparison of testing geometries for twinning stress measurements

The main objective of Chapter 4 was to investigate three different micro-mechanical geometries (micro-shear, pillar and cantilever) in terms of twinning stress measurements and deformation twinning studies. In this section, a comprehensive comparison between the three testing geometries is conducted, as each of them presented challenges regarding specimen preparation, *post mortem* analyses and geometry efficiency.

Among the geometries tested, the optimum approach for quantitative understanding of deformation twinning could be considered the micro-shear. Its unique alignment and geometry allow direct activation of the twinning system without any constrains, therefore, twinning dislocations can freely glide, and slip on other slip systems are not expected due to low resolved shear stress on them. The mechanical data showed good reproducibility, which is evident by the smallest standard deviation compared to the other geometries (Figure 4-5). Hence, reliable mechanical data can be obtained without a large number of specimens tested. In term of *post mortem* analyses including EBSD scans of the sheared region, they were easily performed after the top layer removal by FIB. With that, deformation twinning was confirmed in all specimens tested. However, considering the complexity of this geometry, other factors should be taken in to account during its application to study deformation twinning, such as: (i) perfect alignment with a {111} slip plane; (ii) time-consuming sample fabrication and (iii) opposing shear directions on both shear zones. First, to avoid unwanted slip systems to be activated, this geometries requires perfect alignment with a {111} slip plane. Secondly, in polycrystalline samples, as the one used in this work, an additional coarse milling step for large material removal to expose the desired grain is required. This step was performed by femtosecond pulsed-laser milling in this case, however, could be time-consuming if the milling was to be done with FIB. And finally, as previously discussed in Section 4.2.1, given the polarized nature of deformation twinning and the opposing shear direction in each shear region, twinning will only be triggered in one of the sheared regions and that may result in asymmetric loading.

With the micro-pillar compression test, some of the drawbacks from the micro-shear test can be overcome, such as: alignment challenges, twinning direction and time-consuming fabrication. In a micro-pillar experiment, only the loading direction needs to be considered for deformation twinning, which simplifies the fabrication process. In terms of time, micro-pillars are by far the fastest specimens to fabricate compared to the other geometries. A quick EBSD scan allied with rapid FIB annular milling techniques, reduces the fabrication time which in turn allows statistical data analyses to be done. Such statistical analyses are necessary due to the large standard deviation observed in mechanical data (Figure 4-5). This larger deviation as micro-pillar size decreases are expected in micro to nanoscale testing due to mechanical size effect, as discussed in Section 4.2.2. However, the most challenging aspect in applying the micro-pillar geometry to study deformation twinning is the *post mortem* analyses. Often the twin lamellas observed are in the nanoscale (see Chapter 5 for more details), which could be difficult to resolve by EBSD (due to resolution limitations) and might require further analyses including a lift-out and TEM investigations. Although, keeping in mind that the other geometries may present similar problems. Nevertheless, mechanistic and size effect studies are a possibility with micro-pillar compression experiments, as it enables to mechanically test samples from a micron to nanoscale, proving important insights into underlying mechanism, which will be further explored in Chapter 5. As a conclusion, the micro-pillar geometry is suitable for studying deformation twinning, i.e. quantification of the twinning stress and its mechanism.

Applying the micro-cantilever geometry to investigate deformation twinning is more complex compared to the other geometries in this study. In terms of specimens' fabrication time, given the required TD alignment in a polycrystalline sample, it can be equally tedious as for a micro-shear specimen. For the bending experiment, a line contact is necessary, therefore, instead of a flat punch, a wedge tip is used on the testing set up. This tip requires a good alignment with the specimen to avoid activation of unexpected slip systems. For studying deformation twinning (successfully done in 2 out of 5 samples) the observations on Section 4.2.3 suggested that additional criteria such as setting the twinning direction based on bending moment or larger maximum displacements might be crucial to promote twinning. Compared to the micro-pillars with similar dimension, the cantilevers mechanical data was consistent (Figure 4-5). Finally, although the initial assumptions of ease to apply tensile stresses than a micro-tensile specimen

were correct, the strain gradient in a micro-cantilever complicates the correlation and interpretation of the mechanical data and the twinning mechanism.

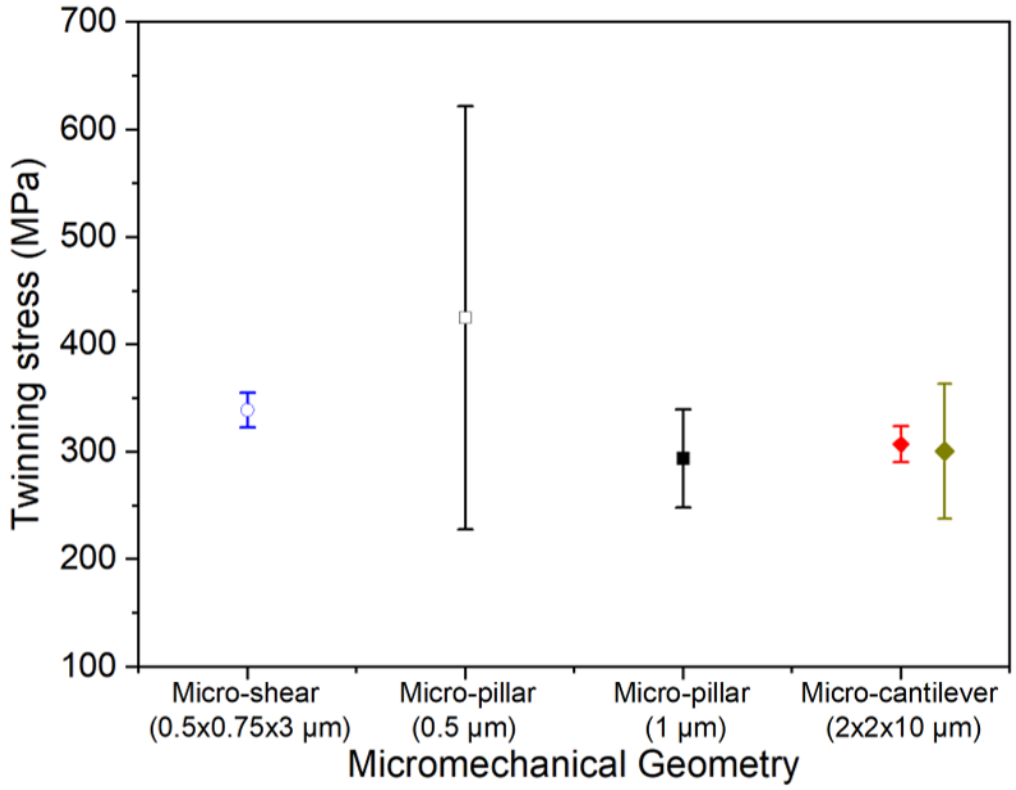

Figure 4-5 Micro mechanical geometries tested and their respective CRSS average and standard deviations. Note that each shape represents a particular geometry and the stress comparison is done according to the samples dimensions. Two different markers are shown for the micro-cantilever, which represents the ones where deformation twinning was not activated (in red) and the ones where it was (in yellow) (reprinted from [8]).

4.4. Conclusion of Chapter 4

In this Chapter, a comprehensive comparison of three micro-mechanical testing geometries to measure the twinning stress of the Cantor alloy was conducted. Among the geometries, the micro-shear one presents an optimum condition for twinning stress measurements with high reproducibility. Additionally, distinguishing twinning and dislocation slip is best done with this

geometry. However, the opposing shear direction in each ligament allows twinning be only triggered in one side. For the micro-pillar geometry, its application ease is a particularly attractive feature, consisting in a fast fabrication process allied to an uncomplicated crystallographic alignment, which makes it a suitable candidate to not only to study twinning mechanism but also measure the twinning stress. Noting that the mechanical size effect, expected in small scale mechanics, requires a large number of specimens to be tested to obtain meaningful data and an extensive *post mortem* analyses might be required depending on the twin lamellas size. And lastly, the micro-cantilever test results showed the least efficiency, activating deformation twinning in only 2 out of 5 samples, which coupled to the complexity in correlating the stresses and mechanism suggest that this geometry is the least suitable to investigate deformation twinning.

5. Insights into the twinning mechanism and stress analysis of the Cantor high entropy alloy

Chapter 5 is based on a manuscript submitted for publication and currently under review.

Manuscript is entitled: "Mechanistic insights and stress analysis of deformation twinning in the Cantor high entropy alloy"

Authors: C.A. Teixeira[1], U. Bansal[1], G. Laplanche[2], P. Gumbsch[1], S. Lee[1], C. Kirchlechner[1]

[1]Institute for Applied Materials, Karlsruhe Institute of Technology, Karlsruhe, 76131, Germany

[2]Institut für Werkstoffe, Ruhr-Universität Bochum, Bochum, D-44801, Germany

All authors have agreed to have this manuscript as the Chapter 5 of this thesis. Each author contribution to the original manuscript can be found in detail in the Appendix, page 90.

5.1. Introduction

The importance of twinning as a deformation mechanism for FCC alloys, including the FCC HEAs such as the Cantor and derivatives, has been well recognized in literature, however, its underlying mechanism remains a question to date. Classical theory explains twin nucleation by the successive glide of Shockley partial dislocations on adjacent {111} planes, leaving a stacking fault on each plane first, which leads to the micro-twin formation. It is generally accepted that dislocation slip activity precedes deformation twinning, however this oversimplifies twin formation and growth processes, and more elaborated models have been proposed (see a detailed description of the models in Chapter 2, page 10).

As demonstrated in Chapter 4, *in situ* micro-pillar compression is a suitable tool for studying twinning mechanisms. Within the micro-mechanical studies reported thus far (only for the Cantor alloy subsets [96,123,124]) there are no experimental reports which explored a large range from a nano to micron scale combined with a detailed investigation of dislocation mechanisms for deformation twinning formation. The variation of micro-pillar diameter is relevant in mechanistic studies, as it provides information on critical stresses for twin nucleation and that allied to

advanced microstructural characterization techniques allows an extensive investigation on twinning mechanisms of the Cantor alloy.

In this Chapter, by applying *in situ* SEM micro-pillar compression tests, the aim is to provide a more comprehensive understanding of the twinning mechanism. Here, micro-pillar of diameters ranging from 0.14 μm to 10 μm were tested and each pillar thoroughly investigated for twinning. With that, mechanistic insights were obtained, as the mechanical behavior and slip activity observed were different as micro-pillar diameter varied, and a comparison of mechanical size effect for twinning stress and full dislocation slip was conducted. Hypotheses of possible twinning mechanism are also discussed in this Chapter.

5.2. Results

5.2.1. *In situ* micro-pillar compression test deformation twinning

The mechanical behavior observed (Figure 5-1(a)) for the micro-pillars tested was as expected in small scale mechanics, as the specimen size decreases there was an increase in the flow stress. This behavior is attributed to the mechanical size effect and it has been explained in literature by the limited number of dislocations (due to small sample volume) as well as size of dislocation sources (as discussed in Chapter 2, page 18) [86]. This also results in the stochastic stress-strain response observed. As pillars size decreased, a shift from load drops to strain bursts is noted, which cannot be attributed to a change in material behavior but rather is caused by the different transducers applied. Given that some pillar were below 0.5 μm diameter, the load was expected to be small and that required the use of a load transducer with a higher force resolution and a higher stiffness which comes at a cost of pronounced strain bursts. Note that the mechanical data interpretation is limited to yield stress taken either from a 2% offset or first strain burst, which ever occurred first.

Post mortem SEM images show that, while sub-micron pillars activated single slip plane, multiple slip planes activation was observed in the micro-pillars with a diameter larger than 1 μm (Figure *5-1*(b) – (d)). Since the micro-pillar were in majority aligned with a ⟨1 1 10⟩ orientation, where several predicted slip systems have a similar or in some cases identical Schmid factors (*m*), activation of multiple slip can be expected. For the micro-pillars between 0.14 μm to 0.5 μm,

single slip on the $(1\bar{1}1)$ slip plane was observed in the *post mortem* SEM analyses (Figure 5-*1*(d) and (e)). The slip planes will be referred as the Thompson tetrahedron notation in the remaining of this Chapter. Therefore, the $(1\bar{1}1)$ plane is the (BCD) that corresponds to (*a*) plane, meaning the plane opposite the to A corner (see the schematic representation on Figure 5-1(f)). This way the plane $(\bar{1}11)$ is the plane (ACD), which corresponds to the (*b*) plane, and so forth. For the 1 µm diameter micro-pillars, two slip planes were activated and identified as (*a*) and (*b*) (Figure 5-1(d)). And lastly, the micro-pillars with diameters of 3 µm and above exhibited activation of multiple slip systems. All 4 possible slip planes predicted by Schmid factor calculations were observed for the 10 µm representative case (Figure 5-1(e)). The slip direction analyses will be introduced once the activation of deformation twinning is confirmed or not.

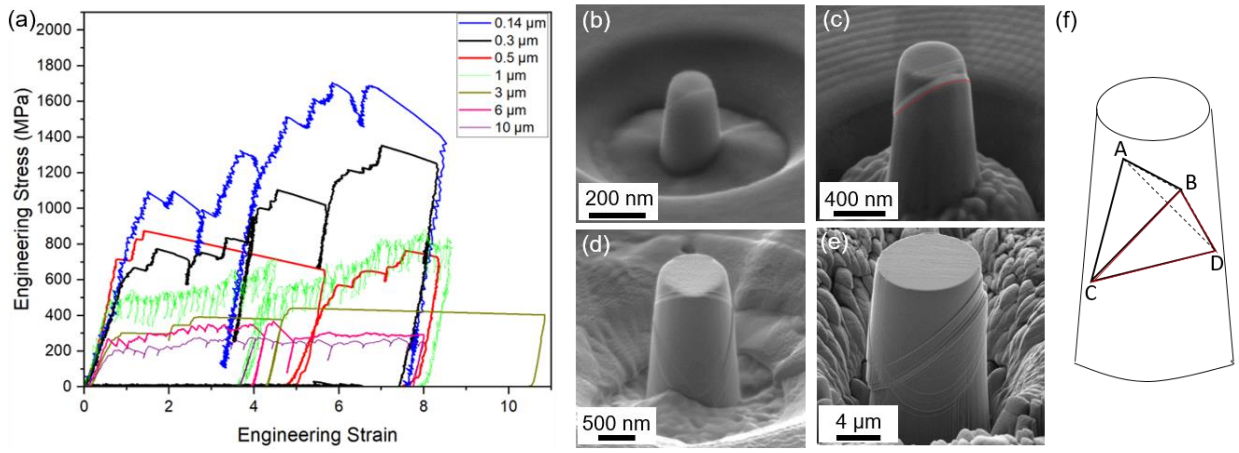

Figure 5-1 *In situ* SEM micropillar compression experiments and respective *post mortem* SEM images: (a) Representative engineering stress and strain curves for all the *in situ* micro-pillar compression. *Post mortem* SEM images of micro-pillars with diameters: (b) 0.14 µm, (c) 0.5 µm, (d) 1 µm and (e) 10 µm. (f) A schematic representation of micro-pillars (b) and (c) with a Thompson tetrahedron oriented close to a ⟨1 1 10⟩ loading direction. (reprinted from reference [9])

5.2.2. *In situ* micro-pillar compression test dislocation slip

To allow for a comparison of dislocation based plasticity and deformation twinning, micro-pillars compression experiments for samples oriented for full dislocation slip were also performed (Figure

5-2). A similar mechanical behavior – increase in flow stress as micro-pillar size decreases – was observed for the samples oriented for full dislocation slip (Figure 5-2(a)) and can be explained as mentioned above (in Section 5.2.1), due to mechanical size-effect that additionally leads to a stochastic response. The analyses of the mechanical data, i.e. yield stress, was maintained similarly to samples deformed by twinning. *Post mortem* SEM images confirmed the activation of a single slip system as predicted by Schmid factor calculations (Figure 5-2(b)). SEM images analyses from top surface and side view of the micro-pillar confirmed the predominant activation of the $(1\bar{1}1)[011]$ slip system for both $[9\ 6\ 11]$ and $[8\ 3\ 10]$, which is the plane (BCD) that corresponds to plane (*a*), and DB Burgers vector, in Thompson tetrahedron notation.

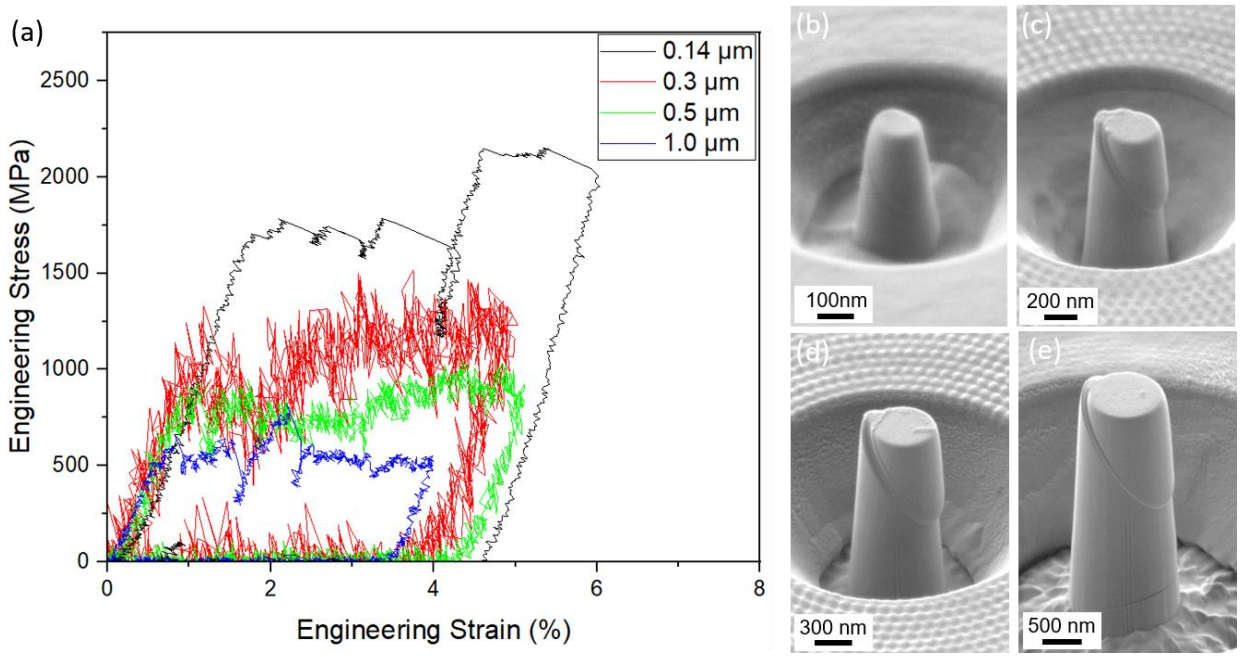

Figure 5-2 *In situ* SEM micro-pillar compression experiments and *post mortem* SEM images, for samples oriented for full dislocation slip: (a) representative engineering stress and strain curve; after deformation micro-pillars of diameter: (b) 0.14 µm, (c) 0.3 µm, (d) 0.5 µm and (e) 1 µm (reprinted from Supplementary material in [9]).

5.2.3. Deformation twinning activation

Post mortem analysis was performed to confirm deformation twinning using the following techniques: EBSD on the top surface, BSE detector imaging on a FIB-milled cross-section as well as lift-out and TEM investigations (Figure 5-3). This analyses started with EBSD on the micro-pillars' top surface, as no further sample preparation was required (Figure 5-3 (a) and (b)). Twinning was evidenced by the change in orientation observed in the IPF-Z map (Figure 5-3 (b)), allied to a 60 degrees misorientation (twin-matrix) (Figure 5-3 (d)) and further confirmed by the (111) pole figure where the twin and matrix shared a common pole that correspond to the twin plane (Figure 5-3 (c)). This way, deformation twinning was confirmed in 6 out of 10 micro-pillars between 1 μm and 6 μm. Out of this range, EBSD was not successful in detecting twinning, as it is a technique only sensitive to the top surface and there is spatial resolution limitation that might not allow possible nanotwins to be resolved. Due to such limitations, EBSD is not able to document the absence of deformation twinning. Then, extensive investigations on the micro-pillars cross-section was performed with BSE imaging and TEM analyses. With the BSE cross-section imaging method, the presence of twin lamella was confirmed in 10 out of 12 micro-pillar, from 0.14 μm to 1 μm diameter (Figure 5-3(e)). In larger micro-pillars, this method was not successful, as finer nanoscale twins were formed and SEM imaging was unable to resolve them. In this case, a lift-out followed by TEM analyses was performed (Figure 5-3(f)), acquiring BF and DF micrographs on a ⟨011⟩ zone axis (ZA) condition. In summary, a total of 22 micro-pillars were analyzed, and deformation twinning presence was observed in 10 out of 12 micro-pillars below 3 μm, only 3 out of 7 between 3 μm and 6 μm, and for the 10 μm diameter pillars no twin was observed (as summarized in Figure 5-4).

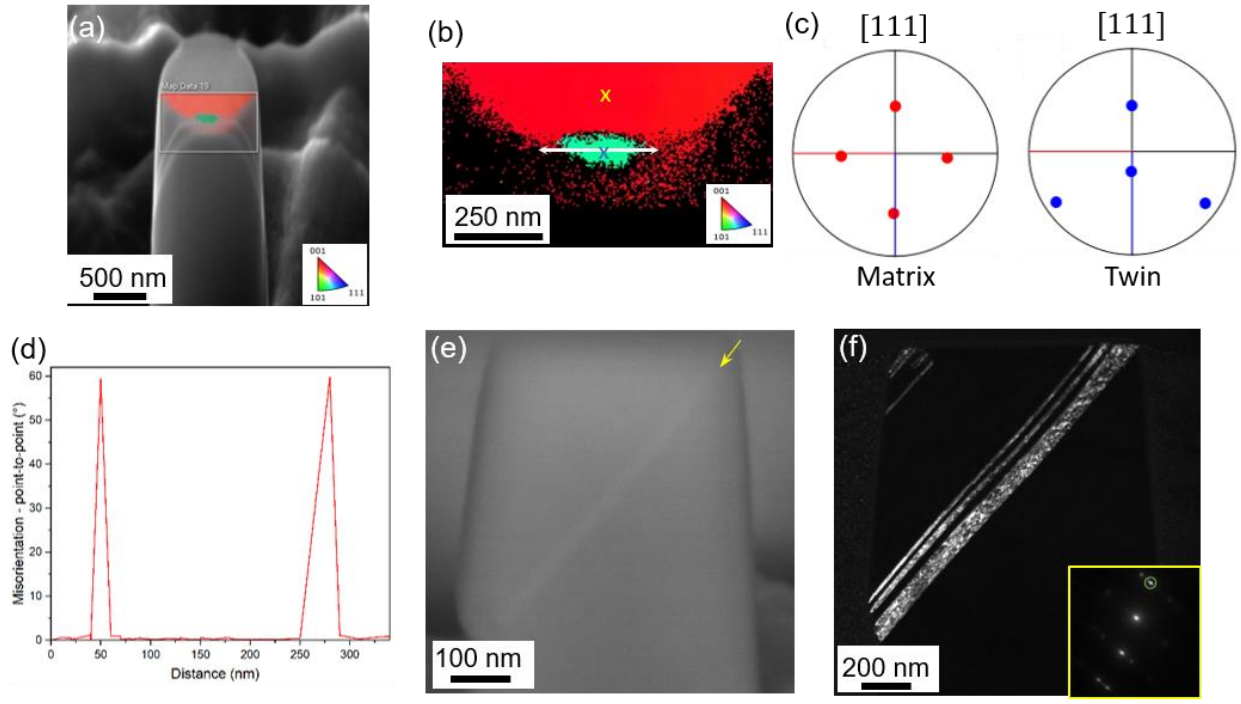

Figure 5-3 *Post mortem* analyses performed to identify if a twin lamella was formed: (a) SEM image of a micro-pillar's side view combined with EBSD IPF-Z map performed on the top surface; (b) EBSD IPF-Z analyses on the micro-pillar's top surface (the green region represents deformation twinning); (c) the matrix and twin [111] PF taken from positions marked by "x" in (b), the blue representing the twin and the yellow representing the matrix; (d) misorientation plot point-to-point of double arrow white line in (b); (e) BSE detector cross-section imaging with twin highlighted by the yellow arrow; and (f) TEM DF image showing layers of twins. (reprinted from reference [9])

An overall plot of CRSS and respective micro-pillars diameters tested is shown in Figure 5-4, with distinction of pillars where twinning was observed (in single slip or multiple slip) and not. Note that in this case the CRSS was calculated as follows: for micro-pillars between 0.14 µm and 6 µm the highest value of *m* for the leading partial dislocation was used regardless if twinning was observed from *post mortem* analysis or not; and for the 10 µm, which deformation twinning was not observed, the highest m for full dislocation slip was used (see Figure 5-4 and Figure 5-5). Detailed analysis on the twinning stress will be continued in the following section.

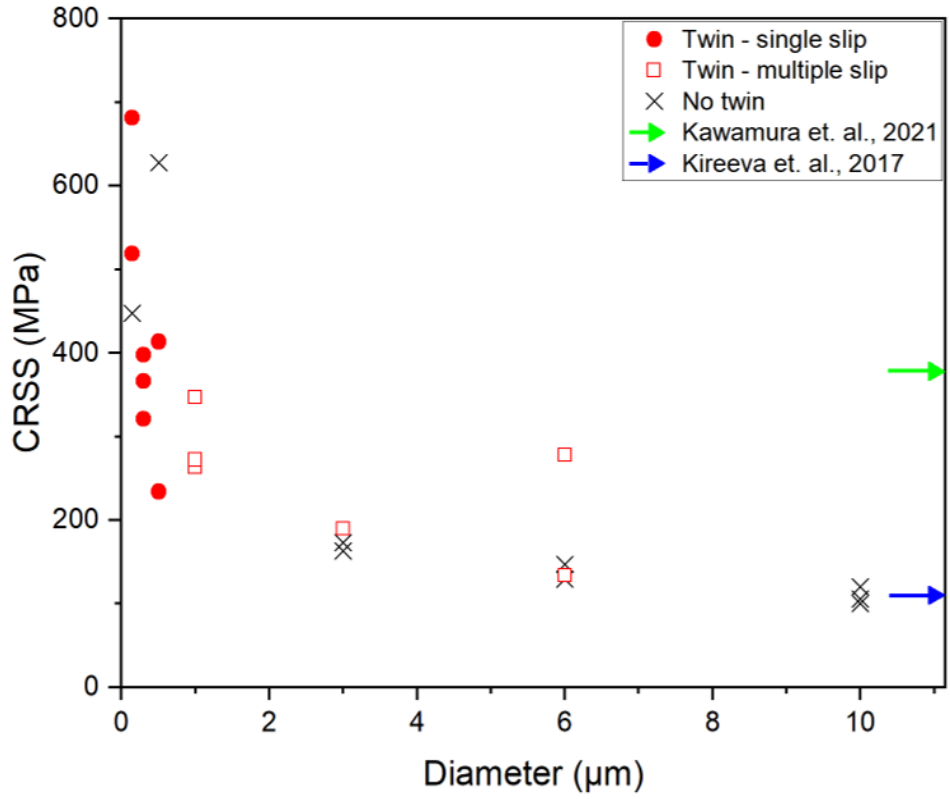

Figure 5-4 Plot of CRSS and respective diameters of micro-pillars. Note that it is highlighted the samples which deformation twinning was observed (in single and multi-slip cases) and samples which it was not. Literature estimated lower and upper bond for twinning stress is also presented in the plot [54,55]. (reprinted from reference [9])

5.2.4. Twinning stress and mechanical size effect

As the micro-pillars' diameter reached 10 μm, the stresses dropped seemingly below the twinning stress threshold, as twinning was not detected by the *post mortem* techniques applied. From CRSS of the micro-pillars that showed deformation twinning in Figure *5-4*, the twinning stress of the given micro-pillar diameter can be calculated. Furthermore, an estimation of the lower bound of the twinning stress of the Cantor alloy could be done by considering the largest micro-pillar with lowest CRSS to activate twinning, which was found to be around 130 MPa. There have been many attempts in literature to estimate the twinning stress of the Cantor alloy, however, solely by interrupted mechanical test in a bulk scale. The effect of grain size or crystallographic orientation,

in the case of single crystals, were evaluated, and the reported twinning stress values varied from 110 MPa to 378 MPa [4,53,55,56,60,65], range within the twinning stress estimated in this work.

Once the micro-pillars that showed deformation twinning were determined (as seen in Figure 5-4), the mechanical size-effect on twinning stress was analyzed (see Figure 5-5). Here, the average of the CRSS for deformation twinning, for each diameter, was used. For comparison purpose, the mechanical size-effect for micro-pillars showing full dislocation slip was also determined, noting that the 3 μm, 6 μm and 10 μm CRSS data was taken from reference [117]. For the fitting, the size scale power-law [113] equation used was:

$$\tau_{2\%} = \tau_{bulk} + k{D_{mp}}^{-n} \tag{7}$$

where k is the fitting parameter, D_{mp} is the micro-pillar's diameter, n is the size scaling exponent and τ_{bulk} is the bulk shear stress which was reported in literature as 50.4 ± 2.0 MPa [125].

Size scaling fitting results initially suggested that the twinning stress could be less size dependent compared to full dislocation slip (see Figure 5-5). In the deformation twinning case the fitted exponent was -0.40 ± 0.04 and for full dislocation slip was -0.51 ± 0.04. Note that in Figure 5-5 the size scaling exponent error was determined by the standard error of them mean scaled with the square root of the reduced Chi square and scatter bars represent the standard deviation. A similar size scaling exponent for full dislocation slip has been reported in literature [125] (as shown in Chapter 2). In the case of deformation twinning, a smaller size exponent of -0.32, has been reported for one of the Cantor alloy's subset, the CoCrFeNi HEA, for micro-pillars of diameters between 272 nm to 1253 nm [96]. Such difference was attributed to a twinning process that would initiate from preexistent dislocation sources and this would lead to a weaker size effect compared to dislocation slip, which requires new dislocation to nucleate from free surfaces as dislocation occurs initial stages of deformation [96]. Nevertheless, both size scaling exponents for twinning and dislocation slip in this work are smaller compared to other FCC metals and alloys [70,89,120], which suggests that other strengthening mechanisms might be more dominant, such as: solid solution hardening or high lattice friction [96,117,125].

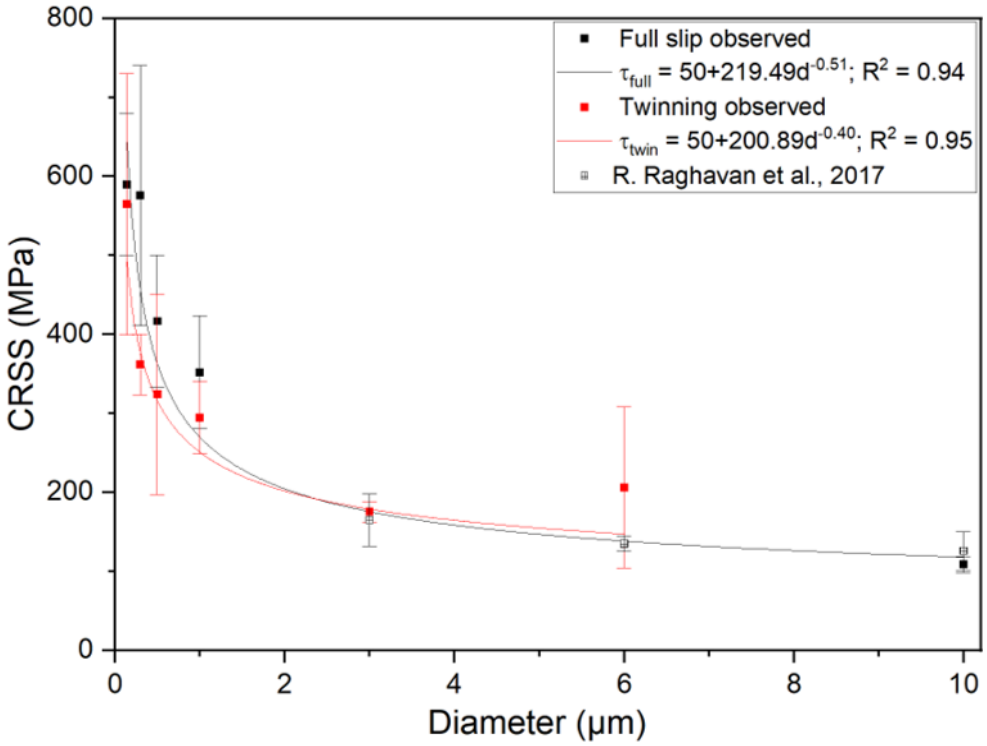

Figure 5-5 *In situ* micro-pillar compression results in a size-effect plot for both full dislocation slip and deformation twinning mechanical. Note that CRSS data from 0.5 μm and 1 μm for deformation twinning was previously showed in the Chapter 4 and published in [8] and CRSS data from 3 μm, 6 μm and 10 μm for full dislocation slip was taken from reference [117] (reprinted from reference [9]).

What is surprising from Figure 5-5 is that, in the case of smaller micro-pillars, the CRSS for deformation twinning is smaller than that of full dislocation slip. As mentioned previously, the smaller size exponent for deformation twinning was attributed to the fact that twinning process requires pre-existing dislocations. Therefore, it is expected that the twinning stress would be higher than that of full dislocation slip. To further the analyses statistically and better understand the CRSS results, cumulative probability plots of the mechanical data were analyzed (see Figure 5-6). The scatted bands on the cumulative probability plots were obtained from a 95% confidence interval. The statistical analyses were limited to micro-pillars of diameter between 0.14 μm and 1 μm, as in these samples the CRSS for twinning was lower than dislocation slip. Most of the mechanical data analyzed follow a very similar trend, except for the 0.3 μm micro-pillars (see

Figure 5-6 (b)). Only for this micro-pillar size, a substantial difference in distribution width and mean CRSS is observed, which suggests that this particular data set could have contributed to the small difference in size scaling exponent calculated for deformation twining oriented pillars. In conclusion, with the present results the difference of size scaling exponent, for deformation twinning compared to full dislocation slip, can be considered negligible.

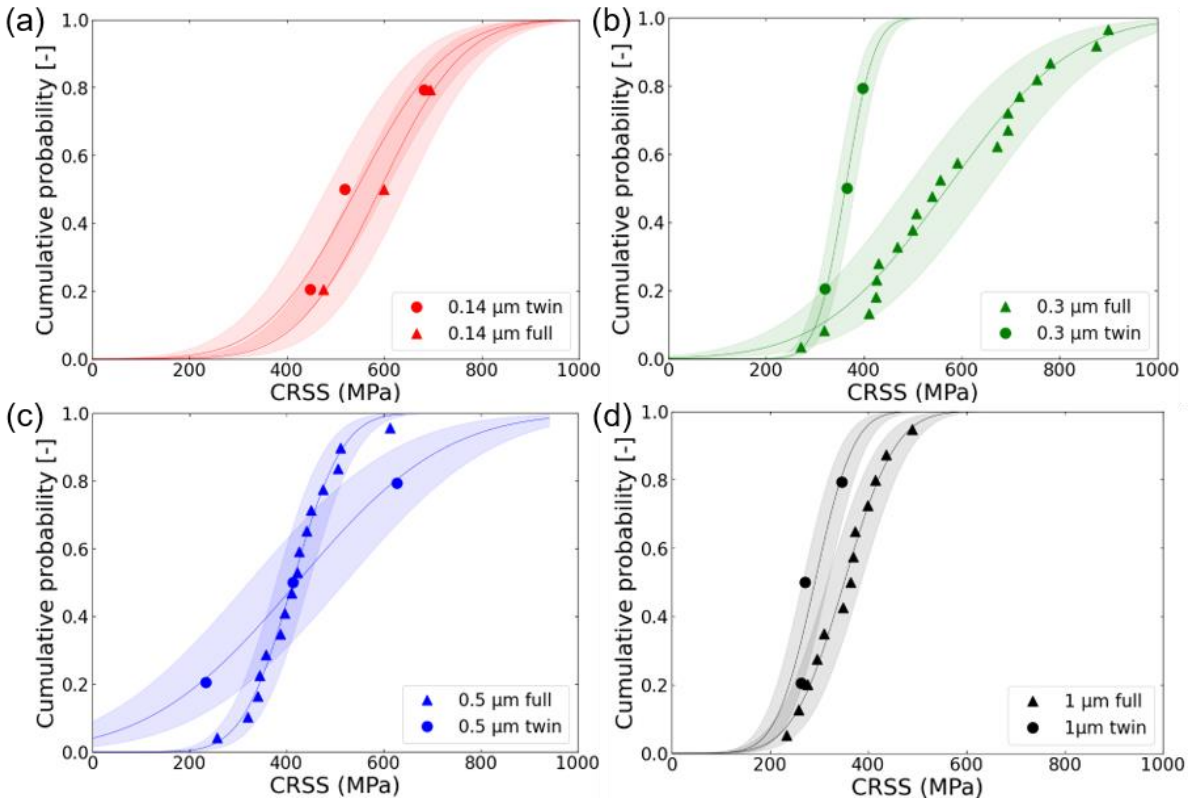

Figure 5-6 Cumulative probability plots of micro-pillars oriented for deformation twinning and full dislocation slip of diameters: (a) 0.14 µm, (b) 0.3 µm, (c) 0.5 µm and (d) 1 µm (reprinted from reference [9]).

5.2.5. Further slip system and TEM investigations

The stress analyses performed in the previous section provided interesting inputs on deformation twinning and critical stresses. To obtain more insights into the twinning mechanism and how twins were nucleated in the micro-pillars tested, further TEM investigations combined with SEM imaging for slip system analyses were performed (Figure 5-7). For the sub-micron pillars, the

0.5 µm will be used as representative, since the pillars were prepared in the same grain and exhibited predominantly the same slip activity (Figure 5-7(a) and (b)). The *post mortem* SEM images from top and side view (Figure 5-7(a) and (b)) confirmed activation of full dislocation slip with a Burgers vector of DB on the plane (*a*). Same plane which a twin lamella was observed with BSE cross-section imaging.

Similarly, indication of dislocation slip activity was also observed in the 1 µm diameter micro-pillars. Since two slip planes were activated, determining the slip direction only by *post mortem* SEM imaging (see Figure 5-7(c)) is complicated and required further TEM investigation (see Figure 5-7(e)). In this case, deformation twinning was only observed in the (*a*) plane and no clear evidence of slip plane interaction was noticed, as no shearing of the twin lamella was observed. Interestingly, as highlighted by the upper case white arrow in Figure 5-7(e), an indication of dislocation slip activity is exhibited as a sharp trace, in contrast to the inclined slip morphology, typical of deformation twinning, indicated by the red arrow.

For the 3 µm micro-pillar case, in addition to multiple slip activation observed by *post mortem* SEM imaging (see Figure 5-7(d)), different features were revealed in the TEM analyses (see Figure 5-7(f)). A single thinner and shorter twin lamella, compared to previously displayed in smaller pillars, were observed (see Figure 5-7(f)).

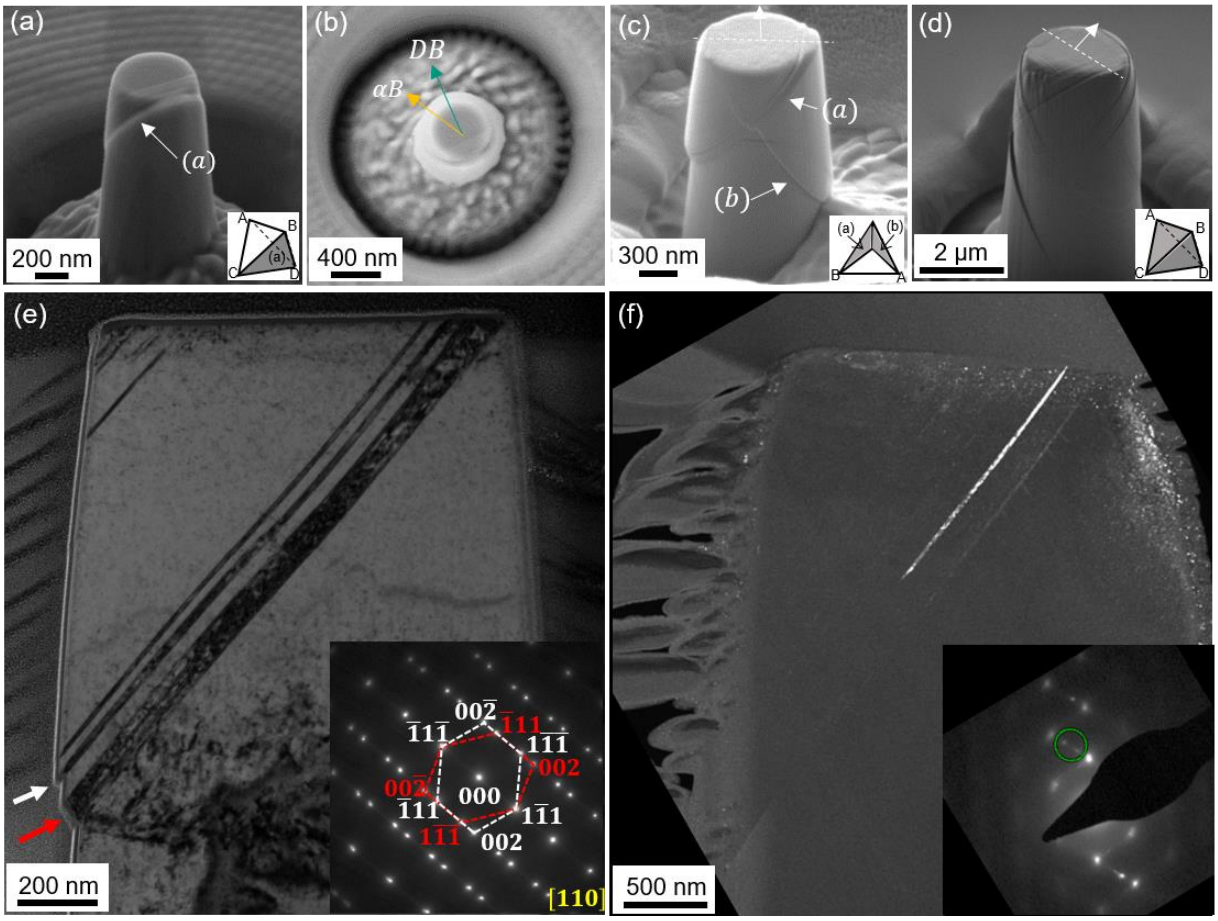

Figure 5-7 *Post mortem* analysis for further investigation of deformation twinning: *post mortem* SEM image of a 0.5 μm diameter micro-pillars from: (a) side and (b) top view; (c) *post mortem* SEM image side view of the (c) 1 μm and (d) 3 μm diameter micro-pillars with respective viewing direction of the TEM lamella in (c) and (f); (e) a TEM BF micrograph of a 1 μm diameter micro-pillar and in inset the selected area diffraction pattern (SADP) taken at the [110] zone axis with the spots corresponding to the twin (a white arrow highlights the dislocation slip trace and a red arrow highlights the twin inclined morphology); (f) Two-beam DF micrograph of a 3 μm diameter micro-pillar taken from 110 diffracted spot and in inset the SADP which shows the spots corresponding to twin. (reprinted from reference [9])

5.3. Discussion

5.3.1. Primary twin mechanism

As introduced in Section 2.2, page 7, there are several twinning mechanisms proposed to describe the twin formation. In the present case, however, given the limited sample volume of the micro-pillars tested and the initial low dislocation density (see calculation on the Appendix, page 76), models that require a particular arrangement of dislocations might be unlikely to occur. In micron to nanoscale samples, the dislocation population (in terms of the number of dislocations, not in terms of densities) is limited, therefore, prismatic sources and/obstacles such as Lomer-Cottrell locks, required for the pole mechanism or two-layer models (respectively) to occur [74,75,77–79,82,85], are less likely to be found compared to bulk samples [72,108]. Considering for instance the two-layer model, reported by Narita and Takamura [77,85], a Lomer-Cottrell lock is the necessary barrier (immobile dislocation) for the twin source to form, which should either be developed through the interaction of two dislocations of different slip planes or already exist within the micro-pillar. In the range of 0.14 μm to 0.5 μm diameter micro-pillars, where single slip system activation was observed and a low number of dislocations due the small pillar size exists, these mechanisms are likely suppressed. Therefore, only surface source nucleation of partial dislocations or Mahajan and Chin's three-layer model remain as a possible twinning mechanism in this scenario [72,73,76].

In the scenario of the three-layer model, a single slip plane activation would be required, in which co-planar dislocations with different Burgers vectors react to form the three-layer stacking fault as twin source. As noticed in the 0.3 μm diameter micro-pillar (see Figure 5-3(c)), the twin lamellae are consistently observed from the top corner of the micro-pillar. This represents the region of highest stresses and in contact with the indenter tip suggesting that such twin lamella could have been nucleated from the top surface. In fact, this feature allowed deformation twinning to be identified in several cases by EBSD analyses of the micro-pillars' top surface. Similarly, this behavior was observed in micro-pillars of 1 μm diameter. In the TEM analyses there was no clear shearing of the twin lamella, i.e. lack of interaction between slip planes (see Figure *5-7*(e)), undermining the multiple slip models, which require two different slip planes to interact. Furthermore, the sharp slip trace highlighted by the white arrow on the TEM BF micrograph (see Figure 5-7(c)) is an evidence that supports strong dislocation slip activity cutting through the whole

pillar. Note that this was the only slip plane twinning was observed. This behavior is consistent with the three-layer model, as multiple slip models would require activation and interaction of different planes and the twin source would form in the center region of the micro-pillar. Additionally, for the sub-micron micro-pillars, not only single slip activation was observed, but also *post mortem* SEM analyses exhibited evidences that suggest full dislocation slip activity (see Figure 5-7(a) and (b)). Therefore, such observations support the hypotheses of the three-layer model. This way, the three-layer stacking fault that acts as the twin source is formed by the co-planar dislocation undergoing the reaction CB+DB→3αB (see the Schmid factors of the dislocations on Table 5-1).

Table 5-1 Schmid factor of dislocations involved in the three-layer mechanism in the case of 0.5 μm pillars, considering its actual compression axis (reprinted from reference [9]).

Dislocation type	Full dislocations		Leading partial dislocation
Burgers vector	CB	DB	αB
Schmid Factor	0.36	0.46	0.47

The other possible scenario for twinning activation in (sub) micron pillars is the nucleation of partial dislocations from surface sources. It is known that surface damage introduced by FIB may serve as sites for dislocation nucleation [95,126–128]. Although this effect diminishes as micro-pillar diameter increases, through reduction of the FIB-affected area, they are more relevant in the 0.14 μm diameter micro-pillars because of their higher surface-to-volume ratio. In the 0.14 μm diameter micro-pillar case, to form a stacking fault the partial dislocation nucleated from a surface source would span across the micro-pillar in a distance of approximately 0.2 μm. This requires a particular shear stress that could be estimated by applying the equation for distance separation between two partials (d_s) proposed by Byun [129], which can be rearranged to calculate the required external stress (τ_{zx}),

$$\tau_{zx} = \frac{2\gamma_{SF}}{b_p} - \frac{2(2-3\nu)Gb_p}{d_s[8\pi(1-\nu)]} \tag{8}$$

where b_p is the partial dislocation Burgers vector, γ_{SF} is the stacking fault energy, ν is the Poisson's ratio and G is the shear modulus. The stacking fault energy for the Cantor alloy has been

reported to be between 20 mJ/m² and 35 mJ/m² [52–55,65,130], the G and v around 81 GPa and 0.25 respectively [131], which results in a required external stress of 265 MPa, a stress level achieved for micro-pillars between 0.14 µm and 1 µm diameter. However, surface nucleation seems unlikely among larger micro-pillars as such stresses are not reached from 3 µm diameter. It is important to note that the key contributor to the required applied stress is the stacking fault energy, therefore, increasing the necessary extension distance of the partial dislocation, e.g. as micro-pillar size increases, will not affect the stress necessary for the stacking fault to be formed (within the diameter range tested).

Nonetheless, twin nucleation does not seem to occur predominantly via surface sources. Considering that the damage layer is throughout the micro-pillar's surface and the loading direction near a ⟨1 1 10⟩ orientation (i.e. similar or close Schmid factors in multiple slip systems), deformation twinning – or the formation of extended stacking faults – should have been observed in several slip planes. However, that is not the case, as twin nucleation was observed in a similar manner for all micro-pillars up to 1 µm diameter, meaning from the top corner and in only one slip system.

As multiple slip systems were activated for micro-pillars larger than 1 µm diameter, distinct features were observed: finer twins (see Figure 5-7(f)) and a different twin morphology (see Figure 5-8). Similarly to the smaller micro-pillars, the 3 µm diameter TEM DF micrograph showed a twin lamella that seems to be nucleate from the top surface of micro-pillar (see Figure 5-7(f)), however, it is shorter (i.e. not across the entire micro-pillar's length) and thinner. This suggests that dislocation slip could contribute more to plastic deformation in larger micro-pillars. Furthermore, the interesting twin morphology observed will be discussed in the following section.

5.3.2. Other twinning mechanisms?

For 3 µm and 6 µm diameter micro-pillars a different twin morphology was observed (see Figure 5-8). Previously the twin lamellae seem to start from the top corner of the micro-pillar, however, the one observed on the TEM DF micrograph at two beam condition (see Figure 5-8(a) and magnified in (b)) for the 3 µm diameter seem to nucleate on the micro-pillars' center region from an activated slip plane in a equidistant manner. TEM electron diffraction analysis confirmed that

this twin array is connected to a slip trace rather than a twin lamella, noted by the strong dark contrast of the slip trace. In the case of the 6 μm diameter micro-pillar, the TEM DF micrograph revealed a twin lamellae with similar morphology to the secondary twin seen on the 3 μm diameter micro-pillar (see Figure 5-8(c) and magnified in (d)). For both cases, 3 μm and 6 μm micro-pillars, it was difficult to determine accurately the twin plane, as the tilt angles in TEM investigation is limited, however the distance measured between the two twin spots were 9.4 nm^{-1} and 9.5 nm^{-1} respectively, which suggested the reflections corresponds to the {111} planes.

Contrary to the smaller micro-pillars presented in Section 5.3.1, other twinning mechanisms become a possibility as multiple slip systems are activated. The other mechanisms refer to the multiple slip models, which are the ones that require either a particular arrangement of dislocation to be within the pillar or the interaction of dislocations of different slip planes to form the twin source (see Section 2.2, page 7). In micro-pillars of 3 μm and 6 μm diameter, a greater dislocation population is expected, however, considering the low dislocation density of the bulk piece (see Appendix, page 83), a small number of dislocations are expected in such samples, even though it is a larger sample volume. Therefore, the likelihood of these dislocations interacting to form the twin sources could be considered small. Therefore, it seems that this particular twin morphology is formed by means of a different nucleation mechanism (see Figure 5-8(b) and (d)).

It could be hypothesized that this twin is formed as a result of a de-twinning process, which occurred on the slip trace where the secondary twin seems to nucleate. Different de-twinning mechanisms have been reported in literature such as the reverse or pseudo reverse de-twinning mode [132,133], however, given that the original crystallographic orientation was reestablished and stress state maintained constant during the experiments, these models could be disregarded and a simpler de-twinning process is proposed. The twin boundaries introduced in the micro-pillar can lead to compatibility stresses on the interface (matrix-twin), due to elastic and plastic anisotropy caused by the different crystallographic orientation [134,135]. The stresses could have increased locally, which triggered the emission of a trailing partial dislocation on the twinning plane leading to de-twinning. Such local stresses were then accommodated by the nucleation of the secondary twins in a different slip plane. Nevertheless, to determine how the secondary twin type nucleated is difficult, especially in a multiple slip activation case, hence the mechanism remains unclear.

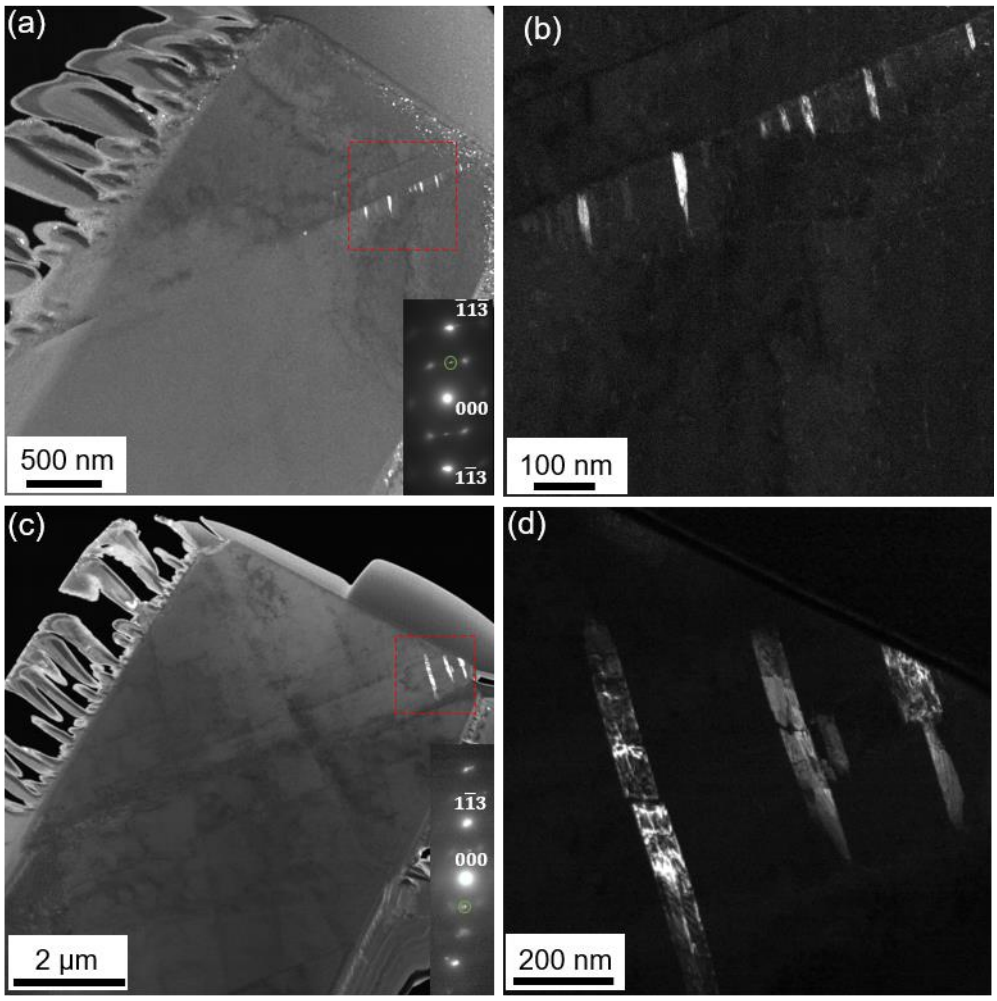

Figure 5-8 TEM analysis exhibiting the microstructure of the secondary twins: (a) a TEM DF micrograph of the 3 µm micro-pillar in two-beam condition, taken from the yellow encircled reflection displayed in inset; (b) magnified TEM DF micrograph of region highlighted by the red dashes region shown in (a); (c) a TEM DF micrograph, of a 6 µm micro-pillar, taken from the encircled reflection displayed in inset; (d) magnified TEM DF micrograph of the red dashed region shown in (d) (reprinted from [9]).

5.3.3. Sub-micron micro-pillar CRSS difference in full slip and twinning

As remarked in Sections 5.3.1 and 5.3.2, twin nucleation evolves from dislocation slip activity. With that in mind, CRSS for dislocation slip would be expected to be lower than the one for

deformation twinning, since dislocation slip is required for a twin source to be formed and additional processes also need to occur to form a twin. However, for micro-pillars below 3 μm diameter, the opposite was observed.

Deformation twinning consists of three major steps: (i) dislocation motion should be activated to initiate a dislocation reaction required for step (ii); (ii) formation of such twin source, and (iii) the same twin source should be activated. Although it is unclear what is the stress required for each step to occur, the steps (ii) and (iii) might not play a dominant role in twinning as the difference in CRSS for deformation twinning compared to dislocation slip is, as shown here, negligible. I.e. no additional stress seems to be necessary to either form the twin source or to activate it. The twinning process continues, once the dislocations required are either present or nucleated to form the twin source. This is an indication that, from a particular threshold stress, strain predominates over stress, therefore for deformation twinning to occur it requires the presence and activation of specific dislocations to develop a twin source.

5.3.4. Twinning mechanism for the other geometries

As different micro-mechanical geometries were tested in this work (see Chapter 4), an additional question could be: can the three-layer model describe twin nucleation in all geometries tested?

Although there were no further investigations with TEM, as carried out for the micro-pillars, for micro-shear geometry there were supporting evidences for the three-layer model (i.e. co-planar dislocations reacting to form the twin source) and the possible dislocation reaction is schematically shown in Figure 5-9(a). Besides single slip activation, SEM imaging of micro-shear specimen's top view showed a rotation of the central loading block along the normal axis to the activated {111} plane, as highlighted by the yellow arrow in Figure 5-9(b). Considering that load direction was aligned to a ⟨112⟩ orientation, this rotation suggest full dislocation slip activity, which could be supporting evidence of the Mahajan and Chin model.

For the micro-cantilever geometry, the three-layer model might not describe twin formation. Here, deformation twinning was only observed in samples that multiple slip systems activation occurred, and, therefore, multi-slip models (e.g. two-layer or stair-rod cross-slip, etc.) become a possibility

and should be considered. However, given the inhomogeneous stress distribution of the micro-cantilever during test, it is difficult to propose the twinning mechanism.

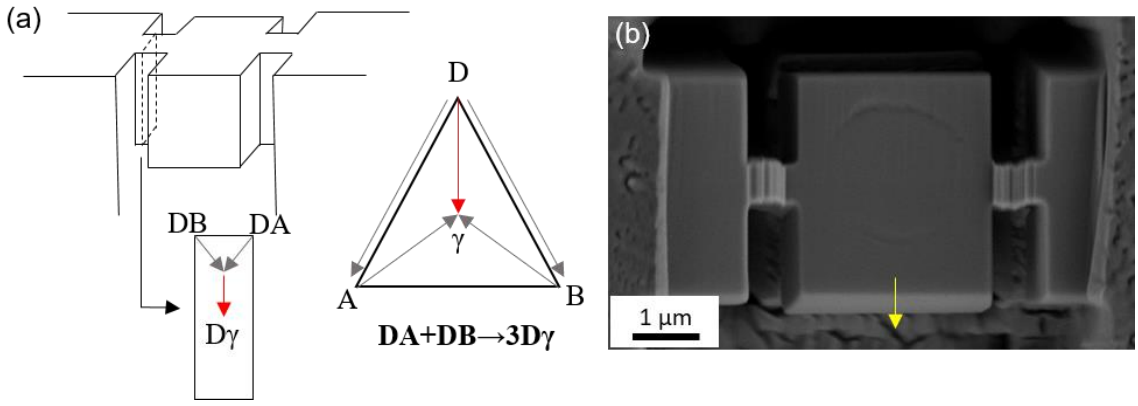

Figure 5-9 Possible twinning mechanism for the micro-shear geometry: (a) schematic of the three-model with the co-planar dislocation reaction and respective Thompson tetrahedron notations; (b) top view SEM image with red arrow highlighting the rotation of the central loading block, which suggest full dislocation slip activity.

5.4. Conclusions of Chapter 5

In this Chapter *in situ* micro-pillar compression was applied to study the twinning mechanism in the Cantor HEA. In summary:

- For the sub-micron micro-pillars, the three-layer twinning mechanism, proposed by Mahajan and Chin, seems to the predominant. SEM and TEM investigations suggested full dislocation activity allied to single slip activation, which supports the hypothesis that the twin source could have been formed by co-planar dislocations with different Burgers vectors reaction.
- Statistical analysis showed a negligible difference in CRSS for deformation twinning and dislocation slip, as the slight calculated difference can be attributed to the 0.3 μm micro-pillar mechanical data, as it was the only sub-set that exhibited a distribution width difference.

- The lower bound of the twinning stress of the Cantor alloy was estimated by the largest micro-pillar to activate deformation twinning, which was around 130 MPa.
- A secondary twin type was identified in 3 μm and 6 μm diameter micro-pillars. The twin formation was hypothesized to occur in consequence of a de-twinning process, where the stress accommodation could have led to the nucleation of the rather equidistant twin lamellae. However, the secondary mechanism remains unclear.
- Above a certain threshold stress, deformation twinning seems strain-dependent rather than stress-dependent.
- In the micro-shear geometry, the three-layer model proposed by Mahajan and Chin seems to be the predominant mechanism, as in addition to single slip plane activation, the rotation of the loading block suggests full dislocation slip activity.
- The twinning mechanism for the micro-cantilever geometry is unclear.

6. Summary

The HEAs approach for materials design enabled not only innumerous alloy possibilities, but most importantly the combination of desirable properties previously thought as mutually exclusive, becoming an attractive alloy. Although widely investigated over the past decades, there is still a lack of fundamental understanding of their underlying deformation mechanism. Therefore, to shed light in this knowledge gap and enable further mechanism-based development of advanced HEAs, in this thesis, deformation twinning was investigated by means of *in situ* SEM micro-mechanical testing on the Cantor HEA. Within the scope of this work, insights into two main questions were obtained: (i) can twinning stress be measured with micromechanics? and (ii) what is the twinning mechanism?

Can twinning stress be measured with micromechanics?

A comprehensive comparison of three micro-mechanical testing geometries, e.g. micro-shear, micro-pillar and micro-cantilever, was done to understand which was the optimum approach to measure the twinning stress of the Cantor alloy and, consequently, study the twinning mechanism. The approach consisted in maintaining the characteristic length of each geometry similar, to allow a comparison among them, and then aligning crystallographically each of their loading axis to maximize the resolved shear stress on the leading partial dislocation, promoting deformation twinning. It was found that micro-shear and micro-pillar were both suitable for deformation twinning studies, given their high success rate in activating twinning and reliable mechanical data.

However, some remarks should be considered for the micro-shear geometry. Although direct activation of the twinning system without constrains (i.e. free dislocation glide) by applying pure shear is a key advantage compared to other geometries, an asymmetric loading might be experienced as twins are only nucleated in one of the ligaments, due to opposing shearing directions. Additionally, the contribution of deformation twinning to the overall shear strain was 2.13%, which is a small contribution. Therefore, deformation is mostly realized by dislocation slip. In contrast, deformation twinning contribution to overall strain for the 1 μm diameter micro-pillar was 44.6% (see Appendix, page 84).

Moreover, given the complexity of the micro-shear geometry in terms of samples alignment and fabrication, micro-pillar compression was the geometry applied for the remainder of the work. Compared to the geometries tested, micro-pillars are easier to fabricate and to analyze the mechanical data, correlating to the underlying mechanism. The ease in fabrication also allows different micro-pillar diameter to be tested, which provides not only the critical stresses for twin nucleation but also twin structure changes, as stress levels are varied, can be observed (combining with advanced characterization techniques), therefore, insights into the possible twinning mechanism.

What is the twinning mechanism?

In situ micro-pillar compression experiments combined with advanced characterization techniques (EBSD, SEM-BSE, TEM) were performed for different micro-pillar diameters, providing important information on critical stresses and their mechanical response was observed, which contributed to further understanding of the twinning mechanism. A transition from single slip to multiple slip activity was observed as the micro-pillar diameter increased, and twin nucleation seems to develop by the means of two distinct twinning mechanism. In the primary twin case, mainly observed in submicron and 1 μm diameter pillars, the three-layer model seems to be the predominant mechanism. Twins were predominantly nucleated from the micro-pillars top surface, single slip (in submicron pillars case) as well as evidences of dislocation slip activity were observed, through SEM and TEM analyses, which are supporting evidences for the Mahajan and Chin mechanism. The same mechanism seems to be predominant for the micro-shear geometry, as single slip activation and evidences for full dislocation slip was observed. Furthermore, although the secondary twin mechanism remains unclear, it was proposed that local stresses could have increased due to compatibility stresses (twin-matrix) leading to emission of the trailing partial dislocations on the twin plane, resulting in detwinning, and nucleation of the secondary twin type to accommodate stresses locally, which was observed in the 3 μm diameter micro-pillar and similar twin morphology seen on the 6 μm micro-pillar.

This mechanistic behavior transition was accompanied by a decrease in CRSS, eventually reaching levels below the twinning stress, and deformation twinning no longer observed for the 10 μm diameter micro-pillars. The twinning stress lower bound in this work was estimated to be around

130 MPa. Moreover, the comparison between deformation twinning and dislocation slip mechanical size effect was found to be negligible. Interestingly, for submicron pillars a lower CRSS for deformation twining compared to dislocation slip was observed, which could be an indication that the dominant factor for deformation twinning would be nucleation of a dislocation, which then would lead to twin source formation and operation without requiring additional stresses.

In conclusion, interesting mechanistic evidences and valuable stress insights were obtained through *in situ* SEM micro-mechanical experiments in this work. Micro-shear and micro-pillar are suitable geometries for deformation twinning studies. Furthermore, evidences suggested that three-layer model, proposed by Mahajan and Chin, was the predominant mechanism, however, the secondary twin type require further investigations to fully comprehend its mechanism.

7. Outlook

Although this work has an important contribution in to the fundamental understanding of deformation twinning, there are still some fundamental questions on the HEAs deformation mechanism remaining, that require further attention in the future.

In this work, relevant insights into most suitable micro-mechanical geometry approach to measure the twinning stress and insights on the twinning mechanism were obtained, however, quantitative stress analyses were limited to the yield stress. Moreover, how the onset of deformation twinning affects the mechanical behavior (e.g. work hardening) of the Cantor alloy has not been explored with small scale mechanics, to the author's knowledge. Macro scale experiments have shown a continuous work hardening coinciding with the onset of deformation twinning, suggesting its contribution. In small scale, micro-pillar compression has been previously applied in TWIP steel [69] and an unstable work hardening for pillars that deformed by mechanical twinning was observed. However, strain hardening measurements are difficult to be performed with micro-pillar compression, as apparent hardening can be caused by lateral forces, sample geometry, etc. This issue could be solved by applying the micro-tensile geometry and would provide additional knowledge about deformation twinning.

Furthermore, what caught initial attention of the scientific community about the Cantor alloy and derivatives was their outstanding mechanical behavior under cryogenic temperatures. Although not an entirely new behavior (i.e. increase of flow stress and ductility), it stood out because of the significant increase combined with high fracture toughness. Thus far, studies have shown a low dependence of the shear modulus to temperature [131,136], which indicates the influence of thermally activated processes on their yield strength. The activation volume measurements in bulk samples [137] and in small scale [118,119] suggested that no new mechanism would arise from the atomic complexity of the HEAs, rather the thermally activated solid solution strengthening [137] or Peierls and dislocation-dislocation interaction [118,119] are the main deformation mechanisms. However, *in situ* SEM micromechanical testing below room temperature could be applied to investigate how dislocation and twin boundary interaction would affect the activation volume. This could provide additional insights to better understand the mechanical behavior of the Cantor alloy and subsets.

8. References

[1] B. Cantor, I.T.H. Chang, P. Knight, A.J.B. Vincent, Microstructural development in equiatomic multicomponent alloys, Mater. Sci. Eng. A 375–377 (2004) 213–218. https://doi.org/10.1016/j.msea.2003.10.257.

[2] J.W. Yeh, S.K. Chen, S.J. Lin, J.Y. Gan, T.S. Chin, T.T. Shun, C.H. Tsau, S.Y. Chang, Nanostructured high-entropy alloys with multiple principal elements: Novel alloy design concepts and outcomes, Adv. Eng. Mater. 6 (2004) 299–303. https://doi.org/10.1002/adem.200300567.

[3] B. Gludovatz, A. Hohenwarter, D. Catoor, E.H. Chang, E.P. George, R.O. Ritchie, A fracture-resistant high-entropy alloy for cryogenic applications, Science. 345 (2014) 1153–1158. https://doi.org/10.1126/science.1254581.

[4] G. Laplanche, A. Kostka, O.M. Horst, G. Eggeler, E.P. George, Microstructure evolution and critical stress for twinning in the CrMnFeCoNi high-entropy alloy, Acta Mater. 118 (2016) 152–163. https://doi.org/10.1016/j.actamat.2016.07.038.

[5] A. Gali, E.P. George, Tensile properties of high- and medium-entropy alloys, Intermetallics 39 (2013) 74–78. https://doi.org/10.1016/j.intermet.2013.03.018.

[6] F. Otto, A. Dlouhý, C. Somsen, H. Bei, G. Eggeler, E.P. George, The influences of temperature and microstructure on the tensile properties of a CoCrFeMnNi high-entropy alloy, Acta Mater. 61 (2013) 5743–5755. https://doi.org/10.1016/j.actamat.2013.06.018.

[7] M.D. Uchic, D.M. Dimiduk, J.N. Florando, W.D. Nix, Sample dimensions influence strength and crystal plasticity, Science. 305 (2004) 986–989. https://doi.org/10.1126/science.1098993.

[8] C.A. Teixeira, S. Lee, C. Kirchlechner, Measuring the twinning stress at the micron scale: A comprehensive comparison of testing geometries, Mater. Charact. 217 (2024) 114314. https://doi.org/10.1016/j.matchar.2024.114314.

[9] C.A. Teixeira, U. Bansal, G. Laplanche, P. Gumbsch, S. Lee, C. Kirchlechner, Mechanistic insights and stress analysis of deformation twinning in the Cantor high entropy alloy, Under Rev. (2025).

[10] E.P. George, W.A. Curtin, C.C. Tasan, High entropy alloys: A focused review of mechanical properties and deformation mechanisms, Acta Mater. 188 (2020) 435–474. https://doi.org/10.1016/j.actamat.2019.12.015.

[11] D.B. Miracle, O.N. Senkov, A critical review of high entropy alloys and related concepts, Acta Mater. 122 (2017) 448–511. https://doi.org/10.1016/j.actamat.2016.08.081.

[12] J.W. Yeh, Recent progress in high-entropy alloys, Ann. Chim. Sci. Des Mater. 31 (2006) 633–648. https://doi.org/10.3166/acsm.31.633-648.

[13] J.W. Yeh, Physical Metallurgy of High-Entropy Alloys, Jom 67 (2015) 2254–2261. https://doi.org/10.1007/s11837-015-1583-5.

[14] S. Ranganathan, Alloyed pleasures: Multimetallic cocktails, Curr. Sci. 85 (2003) 1404–1406.

[15] Y. Wu, F. Zhang, X. Yuan, H. Huang, X. Wen, Y. Wang, M. Zhang, H. Wu, X. Liu, H. Wang, S. Jiang, Z. Lu, Short-range ordering and its effects on mechanical properties of high-entropy alloys, J. Mater. Sci. Technol. 62 (2021) 214–220. https://doi.org/10.1016/j.jmst.2020.06.018.

[16] W. Li, D. Xie, D. Li, Y. Zhang, Y. Gao, P.K. Liaw, Mechanical behavior of high-entropy alloys, Prog. Mater. Sci. 118 (2021) 100777. https://doi.org/10.1016/j.pmatsci.2021.100777.

[17] F. Otto, Y. Yang, H. Bei, E.P. George, Relative effects of enthalpy and entropy on the phase stability of equiatomic high-entropy alloys, Acta Mater. 61 (2013) 2628–2638. https://doi.org/10.1016/j.actamat.2013.01.042.

[18] E.P. George, D. Raabe, R.O. Ritchie, High-entropy alloys, Nat. Rev. Mater. 4 (2019) 515–534. https://doi.org/10.1038/s41578-019-0121-4.

[19] J. Dąbrowa, M. Zajusz, W. Kucza, G. Cieślak, K. Berent, T. Czeppe, T. Kulik, M. Danielewski, Demystifying the sluggish diffusion effect in high entropy alloys, J. Alloys Compd. 783 (2019) 193–207. https://doi.org/10.1016/j.jallcom.2018.12.300.

[20] K.Y. Tsai, M.H. Tsai, J.W. Yeh, Sluggish diffusion in Co-Cr-Fe-Mn-Ni high-entropy

alloys, Acta Mater. 61 (2013) 4887–4897. https://doi.org/10.1016/j.actamat.2013.04.058.

[21] S. V. Divinski, A. V. Pokoev, N. Esakkiraja, A. Paul, A Mystery of "Sluggish Diffusion" in High-Entropy Alloys: The Truth or a Myth?, Diffus. Found. 17 (2018) 69–104. https://doi.org/10.4028/www.scientific.net/df.17.69.

[22] N.L. Okamoto, K. Yuge, K. Tanaka, H. Inui, E.P. George, Atomic displacement in the CrMnFeCoNi high-entropy alloy - A scaling factor to predict solid solution strengthening, AIP Adv. 6 (2016). https://doi.org/10.1063/1.4971371.

[23] Z. Wu, H. Bei, G.M. Pharr, E.P. George, Temperature dependence of the mechanical properties of equiatomic solid solution alloys with face-centered cubic crystal structures, Acta Mater. 81 (2014) 428–441. https://doi.org/10.1016/j.actamat.2014.08.026.

[24] C. Varvenne, A. Luque, W.A. Curtin, Theory of strengthening in fcc high entropy alloys, Acta Mater. 118 (2016) 164–176. https://doi.org/10.1016/j.actamat.2016.07.040.

[25] C. Varvenne, G.P.M. Leyson, M. Ghazisaeidi, W.A. Curtin, Solute strengthening in random alloys, Acta Mater. 124 (2017) 660–683. https://doi.org/10.1016/j.actamat.2016.09.046.

[26] C. Varvenne, A. Luque, W.G. Nöhring, W.A. Curtin, Average-atom interatomic potential for random alloys, Phys. Rev. B 93 (2016) 1–7. https://doi.org/10.1103/PhysRevB.93.104201.

[27] S.S. Sohn, A. Kwiatkowski da Silva, Y. Ikeda, F. Körmann, W. Lu, W.S. Choi, B. Gault, D. Ponge, J. Neugebauer, D. Raabe, Ultrastrong Medium-Entropy Single-Phase Alloys Designed via Severe Lattice Distortion, Adv. Mater. 31 (2019) 1–8. https://doi.org/10.1002/adma.201807142.

[28] R. Zhang, S. Zhao, J. Ding, Y. Chong, T. Jia, C. Ophus, M. Asta, R.O. Ritchie, A.M. Minor, Short-range order and its impact on the CrCoNi medium-entropy alloy, Nature 581 (2020) 283–287. https://doi.org/10.1038/s41586-020-2275-z.

[29] J. Ding, Q. Yu, M. Asta, R.O. Ritchie, Tunable stacking fault energies by tailoring local chemical order in CrCoNi medium-entropy alloys, Proc. Natl. Acad. Sci. U. S. A. 115 (2018) 8919–8924. https://doi.org/10.1073/pnas.1808660115.

[30] Q. Ding, Y. Zhang, X. Chen, X. Fu, D. Chen, S. Chen, L. Gu, F. Wei, H. Bei, Y. Gao, M. Wen, J. Li, Z. Zhang, T. Zhu, R.O. Ritchie, Q. Yu, Tuning element distribution, structure and properties by composition in high-entropy alloys, Nature 574 (2019) 223–227. https://doi.org/10.1038/s41586-019-1617-1.

[31] W. Feng, Y. Qi, S. Wang, Effects of short-range order on the magnetic and mechanical properties of FeCoNi(AlSi)x high entropy alloys, Metals (Basel). 7 (2017). https://doi.org/10.3390/met7110482.

[32] K. Inoue, S. Yoshida, N. Tsuji, Direct observation of local chemical ordering in a few nanometer range in CoCrNi medium-entropy alloy by atom probe tomography and its impact on mechanical properties, Phys. Rev. Mater. 5 (2021) 1–7. https://doi.org/10.1103/PhysRevMaterials.5.085007.

[33] L. Li, Z. Chen, S. Kuroiwa, M. Ito, K. Yuge, K. Kishida, H. Tanimoto, Y. Yu, H. Inui, E.P. George, Evolution of short-range order and its effects on the plastic deformation behavior of single crystals of the equiatomic Cr-Co-Ni medium-entropy alloy, Acta Mater. 243 (2023). https://doi.org/10.1016/j.actamat.2022.118537.

[34] B. Yin, S. Yoshida, N. Tsuji, W.A. Curtin, Yield strength and misfit volumes of NiCoCr and implications for short-range-order, Nat. Commun. 11 (2020) 1–7. https://doi.org/10.1038/s41467-020-16083-1.

[35] Q.J. Li, H. Sheng, E. Ma, Strengthening in multi-principal element alloys with local-chemical-order roughened dislocation pathways, Nat. Commun. 10 (2019) 1–11. https://doi.org/10.1038/s41467-019-11464-7.

[36] C. Tandoc, Y.J. Hu, L. Qi, P.K. Liaw, Mining of lattice distortion, strength, and intrinsic ductility of refractory high entropy alloys, Npj Comput. Mater. 9 (2023) 1–12. https://doi.org/10.1038/s41524-023-00993-x.

[37] P.E.J. Rivera-Díaz-Del-Castillo, H. Fu, Strengthening mechanisms in high-entropy alloys: Perspectives for alloy design, J. Mater. Res. 33 (2018) 2970–2982. https://doi.org/10.1557/jmr.2018.328.

[38] N. Ali, L. Zhang, D. Liu, H. Zhou, K. Sanaullah, C. Zhang, J. Chu, Y. Nian, J. Cheng,

Strengthening mechanisms in high entropy alloys: A review, Mater. Today Commun. 33 (2022) 104686. https://doi.org/10.1016/j.mtcomm.2022.104686.

[39] Z. Li, C.C. Tasan, H. Springer, B. Gault, D. Raabe, Interstitial atoms enable joint twinning and transformation induced plasticity in strong and ductile high-entropy alloys, Sci. Rep. 7 (2017) 1–7. https://doi.org/10.1038/srep40704.

[40] H. Traub, H. Neuhäuser, C. Schwink, Investigations of the yield region of concentrated CuGe and CuZn single crystals-I. Critical resolved shear stress, slip line formation and the true strain rate, Acta Metall. 25 (1977) 437–446. https://doi.org/10.1016/0001-6160(77)90234-6.

[41] T.H. Wille, C. Schwink, Precision measurements of critical resolved shear stress in CuMn alloys, Acta Metall. 34 (1986) 1059–1069. https://doi.org/10.1016/0001-6160(86)90216-6.

[42] T.H. Wille, W. Gieseke, C.H. Schwink, Quantitative analysis of solution hardening in selected copper alloys, Acta Metall. 35 (1987) 2679–2693. https://doi.org/10.1016/0001-6160(87)90267-7.

[43] G. Laplanche, A. Kostka, C. Reinhart, J. Hunfeld, G. Eggeler, E.P. George, Reasons for the superior mechanical properties of medium-entropy CrCoNi compared to high-entropy CrMnFeCoNi, Acta Mater. 128 (2017) 292–303. https://doi.org/10.1016/j.actamat.2017.02.036.

[44] B. Gludovatz, A. Hohenwarter, K.V.S. Thurston, H. Bei, Z. Wu, E.P. George, R.O. Ritchie, Exceptional damage-tolerance of a medium-entropy alloy CrCoNi at cryogenic temperatures, Nat. Commun. 7 (2016) 1–8. https://doi.org/10.1038/ncomms10602.

[45] S. Huang, W. Li, S. Lu, F. Tian, J. Shen, E. Holmström, L. Vitos, Temperature dependent stacking fault energy of FeCrCoNiMn high entropy alloy, Scr. Mater. 108 (2015) 44–47. https://doi.org/10.1016/j.scriptamat.2015.05.041.

[46] N. Stepanov, M. Tikhonovsky, N. Yurchenko, D. Zyabkin, M. Klimova, S. Zherebtsov, A. Efimov, G. Salishchev, Effect of cryo-deformation on structure and properties of CoCrFeNiMn high-entropy alloy, Intermetallics 59 (2015) 8–17. https://doi.org/10.1016/j.intermet.2014.12.004.

[47] S. Kibey, J.B. Liu, D.D. Johnson, H. Sehitoglu, Predicting twinning stress in fcc metals: Linking twin-energy pathways to twin nucleation, Acta Mater. 55 (2007) 6843–6851. https://doi.org/10.1016/j.actamat.2007.08.042.

[48] S.A. Kibey, L.L. Wang, J.B. Liu, H.T. Johnson, H. Sehitoglu, D.D. Johnson, Quantitative prediction of twinning stress in fcc alloys: Application to Cu-Al, Phys. Rev. B - Condens. Matter Mater. Phys. 79 (2009) 1–7. https://doi.org/10.1103/PhysRevB.79.214202.

[49] M.A. Meyers, O. Vöhringer, V.A. Lubarda, The onset of twinning in metals: A constitutive description, Acta Mater. 49 (2001) 4025–4039. https://doi.org/10.1016/S1359-6454(01)00300-7.

[50] R.E. Kubilay, W.A. Curtin, Theory of twin strengthening in fcc high entropy alloys, Acta Mater. 216 (2021) 117119. https://doi.org/10.1016/j.actamat.2021.117119.

[51] J.W. Christian, S. Mahajan, Deformation Twinning, 1995. https://doi.org/10.1002/pssb.2221910204.

[52] C. Wagner, G. Laplanche, Effects of stacking fault energy and temperature on grain boundary strengthening, intrinsic lattice strength and deformation mechanisms in CrMnFeCoNi high-entropy alloys with different Cr/Ni ratios, Acta Mater. 244 (2023) 118541. https://doi.org/10.1016/j.actamat.2022.118541.

[53] C. Wagner, G. Laplanche, Effect of grain size on critical twinning stress and work hardening behavior in the equiatomic CrMnFeCoNi high-entropy alloy, Int. J. Plast. 166 (2023) 103651. https://doi.org/10.1016/j.ijplas.2023.103651.

[54] I. V. Kireeva, Y.I. Chumlyakov, Z. V. Pobedennaya, I. V. Kuksgausen, I. Karaman, Orientation dependence of twinning in single crystalline CoCrFeMnNi high-entropy alloy, Mater. Sci. Eng. A 705 (2017) 176–181. https://doi.org/10.1016/j.msea.2017.08.065.

[55] M. Kawamura, M. Asakura, N.L. Okamoto, K. Kishida, H. Inui, E.P. George, Plastic deformation of single crystals of the equiatomic Cr−Mn−Fe−Co−Ni high-entropy alloy in tension and compression from 10 K to 1273 K, Acta Mater. 203 (2021). https://doi.org/10.1016/j.actamat.2020.10.073.

[56] W. Abuzaid, H. Sehitoglu, Critical resolved shear stress for slip and twin nucleation in

single crystalline FeNiCoCrMn high entropy alloy, Mater. Charact. 129 (2017) 288–299. https://doi.org/10.1016/j.matchar.2017.05.014.

[57] K.V.S. Thurston, A. Hohenwarter, G. Laplanche, E.P. George, B. Gludovatz, R.O. Ritchie, On the onset of deformation twinning in the CrFeMnCoNi high-entropy alloy using a novel tensile specimen geometry, Intermetallics 110 (2019) 106469. https://doi.org/10.1016/j.intermet.2019.04.012.

[58] L. Patriarca, A. Ojha, H. Sehitoglu, Y.I. Chumlyakov, Slip nucleation in single crystal FeNiCoCrMn high entropy alloy, Scr. Mater. 112 (2016) 54–57. https://doi.org/10.1016/j.scriptamat.2015.09.009.

[59] H. Huang, X. Li, Z. Dong, W. Li, S. Huang, D. Meng, X. Lai, T. Liu, S. Zhu, L. Vitos, Critical stress for twinning nucleation in CrCoNi-based medium and high entropy alloys, Acta Mater. 149 (2018) 388–396. https://doi.org/10.1016/j.actamat.2018.02.037.

[60] I. V. Kireeva, Y.I. Chumlyakov, Z. V. Pobedennaya, I. V. Kuksgausen, I. Karaman, Orientation dependence of twinning in single crystalline CoCrFeMnNi high-entropy alloy, Mater. Sci. Eng. A 705 (2017) 176–181. https://doi.org/10.1016/j.msea.2017.08.065.

[61] S.M. Copley, B.H. Kear, The dependence of the width of a dissociated dislocation on dislocation velocity, Acta Metall. 16 (1968) 227–231.

[62] S. Mahajan, Critique of mechanisms of formation of deformation, annealing and growth twins: Face-centered cubic metals and alloys, Scr. Mater. 68 (2013) 95–99. https://doi.org/10.1016/j.scriptamat.2012.09.011.

[63] C. Wagner, E.P. George, G. Laplanche, Effects of grain size and stacking fault energy on twinning stresses of single-phase CrxMn20Fe20Co20Ni40-x high-entropy alloys, Acta Mater. 282 (2025) 120470. https://doi.org/10.1016/j.actamat.2024.120470.

[64] M. Beyramali Kivy, M. Asle Zaeem, Generalized stacking fault energies, ductilities, and twinnabilities of CoCrFeNi-based face-centered cubic high entropy alloys, Scr. Mater. 139 (2017) 83–86. https://doi.org/10.1016/j.scriptamat.2017.06.014.

[65] N.L. Okamoto, S. Fujimoto, Y. Kambara, M. Kawamura, Z.M.T. Chen, H. Matsunoshita, K. Tanaka, H. Inui, E.P. George, Size effect, critical resolved shear stress, stacking fault

energy, and solid solution strengthening in the CrMnFeCoNi high-entropy alloy, Sci. Rep. 6 (2016) 1–10. https://doi.org/10.1038/srep35863.

[66] Y.T. Zhu, X.Z. Liao, X.L. Wu, Deformation twinning in nanocrystalline materials, Prog. Mater. Sci. 57 (2012) 1–62. https://doi.org/10.1016/j.pmatsci.2011.05.001.

[67] J.M. Park, J. Moon, J.W. Bae, M.J. Jang, J. Park, S. Lee, H.S. Kim, Strain rate effects of dynamic compressive deformation on mechanical properties and microstructure of CoCrFeMnNi high-entropy alloy, Mater. Sci. Eng. A 719 (2018) 155–163. https://doi.org/10.1016/j.msea.2018.02.031.

[68] G. Gottstein, Physical Foundations of Materials Science, 2004. https://doi.org/10.1007/978-3-662-09291-0.

[69] W.S. Choi, S. Sandlöbes, N. V. Malyar, C. Kirchlechner, S. Korte-Kerzel, G. Dehm, B.C. De Cooman, D. Raabe, Dislocation interaction and twinning-induced plasticity in face-centered cubic Fe-Mn-C micro-pillars, Acta Mater. 132 (2017) 162–173. https://doi.org/10.1016/j.actamat.2017.04.043.

[70] W.S. Choi, B.C. De Cooman, S. Sandlöbes, D. Raabe, Size and orientation effects in partial dislocation-mediated deformation of twinning-induced plasticity steel micro-pillars, Acta Mater. 98 (2015) 391–404. https://doi.org/10.1016/j.actamat.2015.06.065.

[71] S.Z. Wu, H.W. Yen, M.X. Huang, A.H.W. Ngan, Deformation twinning in submicron and micron pillars of twinning-induced plasticity steel, Scr. Mater. 67 (2012) 641–644. https://doi.org/10.1016/j.scriptamat.2012.07.023.

[72] Z.Y. Liang, M.X. Huang, Deformation twinning in small-sized face-centred cubic single crystals: Experiments and modelling, J. Mech. Phys. Solids 85 (2015) 128–142. https://doi.org/10.1016/j.jmps.2015.09.004.

[73] J. Michler, K. Wasmer, S. Meier, F. Östlund, K. Leifer, Plastic deformation of gallium arsenide micropillars under uniaxial compression at room temperature, Appl. Phys. Lett. 90 (2007). https://doi.org/10.1063/1.2432277.

[74] J.A. Venables, Deformation twinning in face-centred cubic metals, Philos. Mag. 6 (1961) 379–396. https://doi.org/10.1080/14786436108235892.

[75] J.A. Venables, On dislocation pole models for twinning, Philos. Mag. 30 (1974) 1165–1169. https://doi.org/10.1080/14786437408207269.

[76] S. Mahajan, G.Y. Chin, Formation of deformation twins in f.c.c. crystals, Acta Metall. 21 (1973) 1353–1363.

[77] N. Narita, J. Takamura, Deformation twinning in silver- and copper-alloy crystals, Philos. Mag. 29 (1974) 1001–1028. https://doi.org/10.1080/14786437408226586.

[78] J.B. Cohen, J. Weertman, A dislocation model for twinning in f.c.c. metals, Acta Metall. 11 (1963) 996–998. https://doi.org/10.1016/0001-6160(63)90033-6.

[79] H. Fujita, T. Mori, A formation mechanism of mechanical twins in F.C.C. Metals, Scr. Metall. 9 (1975) 631–636. https://doi.org/10.1016/0036-9748(75)90476-7.

[80] T. Mori, H. Fujita, Dislocation reactions during deformation twinning in Cu-11at.% Al single crystals, Acta Metall. 28 (1980) 771–776. https://doi.org/10.1016/0001-6160(80)90154-6.

[81] S. Mahajan, The evolution of intrinsic-extrinsic faulting in fcc crystals, Metall. Trans. A 6 (1975) 1877–1886. https://doi.org/10.1007/BF02646851.

[82] A.H. Cottrell, B.A. Bilby, LX. A mechanism for the growth of deformation twins in crystals, London, Edinburgh, Dublin Philos. Mag. J. Sci. 42 (1951) 573–581. https://doi.org/10.1080/14786445108561272.

[83] T.H. Lee, C.S. Oh, S.J. Kim, S. Takaki, Deformation twinning in high-nitrogen austenitic stainless steel, Acta Mater. 55 (2007) 3649–3662. https://doi.org/10.1016/j.actamat.2007.02.023.

[84] B.C. De Cooman, Y. Estrin, S. Kyu, Twinning-induced plasticity (TWIP) steels, Acta Mater. 142 (2018) 283–362. https://doi.org/10.1016/j.actamat.2017.06.046.

[85] N. Narita, J.I. Takamura, Twinning in f.c.c. and b.c.c. metals, Dislocations in Solids 9 (1992) 135–169.

[86] G. Dehm, B.N. Jaya, R. Raghavan, C. Kirchlechner, Overview on micro- and nanomechanical testing: New insights in interface plasticity and fracture at small length

scales, Acta Mater. 142 (2018) 248–282. https://doi.org/10.1016/j.actamat.2017.06.019.

[87] M.D. Uchic, D.M. Dimiduk, A methodology to investigate size scale effects in crystalline plasticity using uniaxial compression testing, Mater. Sci. Eng. A 400–401 (2005) 268–278. https://doi.org/10.1016/j.msea.2005.03.082.

[88] J. Hütsch, E.T. Lilleodden, The influence of focused-ion beam preparation technique on microcompression investigations: Lathe vs. annular milling, Scr. Mater. 77 (2014) 49–51. https://doi.org/10.1016/j.scriptamat.2014.01.016.

[89] D.M. Dimiduk, M.D. Uchic, T.A. Parthasarathy, Size-affected single-slip behavior of pure nickel microcrystals, Acta Mater. 53 (2005) 4065–4077. https://doi.org/10.1016/j.actamat.2005.05.023.

[90] B. Kondori, A. Needleman, A. Amine Benzerga, Discrete dislocation simulations of compression of tapered micropillars, J. Mech. Phys. Solids 101 (2017) 223–234. https://doi.org/10.1016/j.jmps.2017.01.015.

[91] D. Kiener, C. Motz, G. Dehm, Micro-compression testing : A critical discussion of experimental constraints, Mater. Sci. Eng. A 505 (2009) 79–87. https://doi.org/10.1016/j.msea.2009.01.005.

[92] M.D. Uchic, P.A. Shade, D.M. Dimiduk, Plasticity of micrometer-scale single crystals in compression, Annu. Rev. Mater. Res. 39 (2009) 361–386. https://doi.org/10.1146/annurev-matsci-082908-145422.

[93] C. Kirchlechner, J. Keckes, C. Motz, W. Grosinger, M.W. Kapp, J.S. Micha, O. Ulrich, G. Dehm, Impact of instrumental constraints and imperfections on the dislocation structure in micron-sized Cu compression pillars, Acta Mater. 59 (2011) 5618–5626. https://doi.org/10.1016/j.actamat.2011.05.037.

[94] D. Kiener, W. Grosinger, G. Dehm, R. Pippan, A further step towards an understanding of size-dependent crystal plasticity: In situ tension experiments of miniaturized single-crystal copper samples, Acta Mater. 56 (2008) 580–592. https://doi.org/10.1016/j.actamat.2007.10.015.

[95] Z.Y. Liang, J.T.M. De Hosson, M.X. Huang, Size effect on deformation twinning in face-

centred cubic single crystals: Experiments and modelling, Acta Mater. 129 (2017) 1–10. https://doi.org/10.1016/j.actamat.2017.02.063.

[96] Q. Zhang, R. Huang, J. Jiang, T. Cao, Y. Zeng, J. Li, Y. Xue, X. Li, Size effects and plastic deformation mechanisms in single-crystalline CoCrFeNi micro/nanopillars, J. Mech. Phys. Solids 162 (2022) 104853. https://doi.org/10.1016/j.jmps.2022.104853.

[97] G. Dehm, Miniaturized single-crystalline fcc metals deformed in tension: New insights in size-dependent plasticity, Prog. Mater. Sci. 54 (2009) 664–688. https://doi.org/10.1016/j.pmatsci.2009.03.005.

[98] C. Motz, T. Schöberl, R. Pippan, Mechanical properties of micro-sized copper bending beams machined by the focused ion beam technique, Acta Mater. 53 (2005) 4269–4279. https://doi.org/10.1016/j.actamat.2005.05.036.

[99] C. Motz, D. Weygand, J. Senger, P. Gumbsch, Micro-bending tests: A comparison between three-dimensional discrete dislocation dynamics simulations and experiments, Acta Mater. 56 (2008) 1942–1955. https://doi.org/10.1016/j.actamat.2007.12.053.

[100] B.N. Jaya, C. Kirchlechner, G. Dehm, Can microscale fracture tests provide reliable fracture toughness values? A case study in silicon, J. Mater. Res. 30 (2015) 686–698. https://doi.org/10.1557/jmr.2015.2.

[101] C. Mayr, G. Eggeler, G.A. Webster, G. Peter, Double shear creep testing of superalloy single crystals at temperatures above 1000 °C, Mater. Sci. Eng. A 199 (1995) 121–130. https://doi.org/10.1016/0921-5093(94)09721-6.

[102] J. Pfetzing-Micklich, S. Brinckmann, S.R. Dey, F. Otto, A. Hartmaier, G. Eggeler, Micro-shear deformation of pure copper, Materwiss. Werksttech. 42 (2011) 219–223. https://doi.org/10.1002/mawe.201100715.

[103] J.K. Heyer, S. Brinckmann, J. Pfetzing-Micklich, G. Eggeler, Microshear deformation of gold single crystals, Acta Mater. 62 (2014) 225–238. https://doi.org/10.1016/j.actamat.2013.10.002.

[104] N. Wieczorek, G. Laplanche, J.K. Heyer, A.B. Parsa, J. Pfetzing-Micklich, G. Eggeler, Assessment of strain hardening in copper single crystals using in situ SEM microshear

experiments, Acta Mater. 113 (2016) 320–334. https://doi.org/10.1016/j.actamat.2016.04.055.

[105] M. Seok, H. Gopalan, S. Nandy, S. Zaefferer, D. Raabe, C. Kirchlechner, G. Dehm, Microscale plastic anisotropy of basal and pyramidal I slip in pure magnesium tested in shear, Materialia 14 (2020) 100932. https://doi.org/10.1016/j.mtla.2020.100932.

[106] J.R. Greer, W.D. Nix, Nanoscale gold pillars strengthened through dislocation starvation, Phys. Rev. B - Condens. Matter Mater. Phys. 73 (2006) 1–6. https://doi.org/10.1103/PhysRevB.73.245410.

[107] J.A. El-Awady, M. Wen, N.M. Ghoniem, The role of the weakest-link mechanism in controlling the plasticity of micropillars, J. Mech. Phys. Solids 57 (2009) 32–50. https://doi.org/10.1016/j.jmps.2008.10.004.

[108] J.R. Greer, J.T.M. De Hosson, Plasticity in small-sized metallic systems: Intrinsic versus extrinsic size effect, Prog. Mater. Sci. 56 (2011) 654–724. https://doi.org/10.1016/j.pmatsci.2011.01.005.

[109] J.R. Greer, W.C. Oliver, W.D. Nix, Size dependence of mechanical properties of gold at the micron scale in the absence of strain gradients, Acta Mater. 53 (2005) 1821–1830. https://doi.org/10.1016/j.actamat.2004.12.031.

[110] S.I. Rao, D.M. Dimiduk, M. Tang, T.A. Parthasarathy, M.D. Uchic, C. Woodward, Estimating the strength of single-ended dislocation sources in micron-sized single crystals, Philos. Mag. 87 (2007) 4777–4794. https://doi.org/10.1080/14786430701591513.

[111] T.A. Parthasarathy, S.I. Rao, D.M. Dimiduk, M.D. Uchic, D.R. Trinkle, Contribution to size effect of yield strength from the stochastics of dislocation source lengths in finite samples, Scr. Mater. 56 (2007) 313–316. https://doi.org/10.1016/j.scriptamat.2006.09.016.

[112] D.M. Norfleet, D.M. Dimiduk, S.J. Polasik, M.D. Uchic, M.J. Mills, Dislocation structures and their relationship to strength in deformed nickel microcrystals, Acta Mater. 56 (2008) 2988–3001. https://doi.org/10.1016/j.actamat.2008.02.046.

[113] R. Dou, B. Derby, A universal scaling law for the strength of metal micropillars and nanowires, Scr. Mater. 61 (2009) 524–527.

https://doi.org/10.1016/j.scriptamat.2009.05.012.

[114] K.S. Ng, A.H.W. Ngan, Breakdown of Schmid's law in micropillars, Scr. Mater. 59 (2008) 796–799. https://doi.org/10.1016/j.scriptamat.2008.06.019.

[115] S.I. Rao, D.M. Dimiduk, T.A. Parthasarathy, M.D. Uchic, M. Tang, C. Woodward, Athermal mechanisms of size-dependent crystal flow gleaned from three-dimensional discrete dislocation simulations, Acta Mater. 56 (2008) 3245–3259. https://doi.org/10.1016/j.actamat.2008.03.011.

[116] S. Lee, M.J. Duarte, M. Feuerbacher, R. Soler, C. Kirchlechner, C.H. Liebscher, S.H. Oh, G. Dehm, Dislocation plasticity in FeCoCrMnNi high-entropy alloy: quantitative insights from in situ transmission electron microscopy deformation, Mater. Res. Lett. 8 (2020) 216–224. https://doi.org/10.1080/21663831.2020.1741469.

[117] R. Raghavan, C. Kirchlechner, B.N. Jaya, M. Feuerbacher, G. Dehm, Mechanical size effects in a single crystalline equiatomic FeCrCoMnNi high entropy alloy, Scr. Mater. 129 (2017) 52–55. https://doi.org/10.1016/j.scriptamat.2016.10.026.

[118] Y. Xiao, Y. Zou, A.S. Sologubenko, R. Spolenak, J.M. Wheeler, Size-dependent strengthening in multi-principal element , face-centered cubic alloys, Mater. Des. 193 (2020) 108786. https://doi.org/10.1016/j.matdes.2020.108786.

[119] Y. Xiao, R. Kozak, M.J.R. Hach, W. Steurer, R. Spolenak, J.M. Wheeler, Y. Zou, Micro-compression studies of face-centered cubic and body-centered cubic high-entropy alloys : Size-dependent strength , strain rate sensitivity , and activation volumes, Mater. Sci. Eng. A 790 (2020). https://doi.org/10.1016/j.msea.2020.139429.

[120] C.A. Volkert, E.T. Lilleodden, Size effects in the deformation of sub-micron Au columns, Philos. Mag. 86 (2006) 5567–5579. https://doi.org/10.1080/14786430600567739.

[121] A.S. Tirunilai, J. Sas, K.P. Weiss, H. Chen, D.V. Szabó, S. Schlabach, S. Haas, D. Geissler, J. Freudenberger, M. Heilmaier, A. Kauffmann, Peculiarities of deformation of CoCrFeMnNi at cryogenic temperatures, J. Mater. Res. 33 (2018) 3287–3300. https://doi.org/10.1557/jmr.2018.252.

[122] K. Lu, A. Chauhan, A.S. Tirunilai, J. Freudenberger, A. Kauffmann, M. Heilmaier, J. Aktaa,

Deformation mechanisms of CoCrFeMnNi high-entropy alloy under low-cycle-fatigue loading, Acta Mater. 215 (2021) 117089. https://doi.org/10.1016/j.actamat.2021.117089.

[123] N.J. Liu, Z.J. Wang, J. Ding, M. Asta, R.O. Ritchie, B. Gan, E. Ma, Z.W. Shan, Origin of the high propensity for nanoscale deformation twins in CrCoNi medium-entropy alloy, J. Mater. Sci. Technol. 183 (2024) 63–71. https://doi.org/10.1016/j.jmst.2023.10.025.

[124] X.K. Shang, Q.W. Guan, B.B. He, Enhanced strain hardening induced by twin boundary-dislocation interaction in micro-pillar compression of CoCrNi medium-entropy alloy, Materialia 24 (2022). https://doi.org/10.1016/j.mtla.2022.101491.

[125] S. Lee, M.J. Duarte, M. Feuerbacher, R. Soler, C. Kirchlechner, C.H. Liebscher, S.H. Oh, G. Dehm, S. Lee, M.J. Duarte, M. Feuerbacher, R. Soler, Dislocation plasticity in FeCoCrMnNi high- entropy alloy : quantitative insights from in situ transmission electron microscopy deformation, Mater. Res. Lett. 8 (2020) 216–224. https://doi.org/10.1080/21663831.2020.1741469.

[126] S. Lee, J. Jeong, Y. Kim, S.M. Han, D. Kiener, S.H. Oh, FIB-induced dislocations in Al submicron pillars: Annihilation by thermal annealing and effects on deformation behavior, Acta Mater. 110 (2016) 283–294. https://doi.org/10.1016/j.actamat.2016.03.017.

[127] S. Shim, H. Bei, M.K. Miller, G.M. Pharr, E.P. George, Effects of focused ion beam milling on the compressive behavior of directionally solidified micropillars and the nanoindentation response of an electropolished surface, Acta Mater. 57 (2009) 503–510. https://doi.org/10.1016/j.actamat.2008.09.033.

[128] L. Borasi, A. Slagter, A. Mortensen, C. Kirchlechner, On the preparation and mechanical testing of nano to micron-scale specimens, Acta Mater. (2024) 120394. https://doi.org/10.1016/j.actamat.2024.120394.

[129] T.S. Byun, On the stress dependence of partial dislocation separation and deformation microstructure in austenitic stainless steels, Acta Mater. 51 (2003) 3063–3071. https://doi.org/10.1016/S1359-6454(03)00117-4.

[130] S.F. Liu, Y. Wu, H.T. Wang, J.Y. He, J.B. Liu, C.X. Chen, X.J. Liu, H. Wang, Z.P. Lu, Stacking fault energy of face-centered-cubic high entropy alloys, Intermetallics 93 (2018)

269–273. https://doi.org/10.1016/j.intermet.2017.10.004.

[131] G. Laplanche, P. Gadaud, O. Horst, F. Otto, G. Eggeler, E.P. George, Temperature dependencies of the elastic moduli and thermal expansion coefficient of an equiatomic, single-phase CoCrFeMnNi high-entropy alloy, J. Alloys Compd. 623 (2015) 348–353. https://doi.org/10.1016/j.jallcom.2014.11.061.

[132] M.S. Szczerba, S. Kopacz, M.J. Szczerba, On the reverse mode of fcc deformation twinning, Acta Mater. 60 (2012) 6413–6420. https://doi.org/10.1016/j.actamat.2012.08.028.

[133] M.J. Szczerba, S. Kopacz, M.S. Szczerba, Experimental studies on detwinning of face-centered cubic deformation twins, Acta Mater. 104 (2016) 52–61. https://doi.org/10.1016/j.actamat.2015.11.025.

[134] I. Tiba, T. Richeton, C. Motz, H. Vehoff, S. Berbenni, Incompatibility stresses at grain boundaries in Ni bicrystalline micropillars analyzed by an anisotropic model and slip activity, Acta Mater. 83 (2015) 227–238. https://doi.org/10.1016/j.actamat.2014.09.033.

[135] T. Richeton, I. Tiba, S. Berbenni, O. Bouaziz, Analytical expressions of incompatibility stresses at Σ3111 twin boundaries and consequences on single-slip promotion parallel to twin plane, Philos. Mag. 95 (2015) 12–31. https://doi.org/10.1080/14786435.2014.984787.

[136] A. Haglund, M. Koehler, D. Catoor, E.P. George, V. Keppens, Polycrystalline elastic moduli of a high-entropy alloy at cryogenic temperatures, Intermetallics 58 (2015) 62–64. https://doi.org/10.1016/j.intermet.2014.11.005.

[137] G. Laplanche, J. Bonneville, C. Varvenne, W.A. Curtin, E.P. George, Thermal activation parameters of plastic flow reveal deformation mechanisms in the CrMnFeCoNi high-entropy alloy, Acta Mater. 143 (2018) 257–264. https://doi.org/10.1016/j.actamat.2017.10.014.

9. Appendix

ECCI dislocation density calculations

Electron channeling contrast imaging (ECCI) in the SEM was applied to calculate the initial dislocation density of the undeformed bulk samples used in this work. Additional SEM images with the SE detector were taken to avoid possible artifacts. During the analyses the acceleration voltage was kept as 30 kV and the current use was 5 nA. After the ECC images were taken, the initial dislocation density was calculated using the equation, $\rho = 2N/Lt$ (9), where N is the number of dislocation lines that intersect the line of length (L), and t is the probe depth, which was considered as 100 nm. The lines were kept with the same length, 3.5 µm, and 5 lines were drawn randomly and the process repeated 4 times (see Figure 9-1). Therefore, the initial dislocation density was calculated around $4.6 \pm 1.8 \times 10^{12}$ m^{-2}.

Figure 9-1 SEM ECCI analyses to calculated initial dislocation density by the line intersection method (reprinted from [9]).

Deformation twinning contribution micro-pillar compression

The contribution of deformation twinning (ε_t) to strain in a micro-pillar can be computed applying the equation [72],

$$\varepsilon_t = T\gamma_t \cos(\theta)/H \qquad 10$$

where T is the thickness of the twin lamella measured with the TEM micrograph, γ_t is the twinning shear strain $\sqrt{2}/2$ [51] and θ is the angle between the micro-pillar axis and the twinning direction (see Figure 9-2). Here it was considered the micro-pillar with 1 µm diameter, which is observed in Figure 9-2(b). The total twin lamellae thickness measured around 132 nm, the θ was found around 40° and the micro-pillar's initial height was 2.1 µm. Therefore, the calculated contribution in relation to the total engineering strain applied was 44.6%.

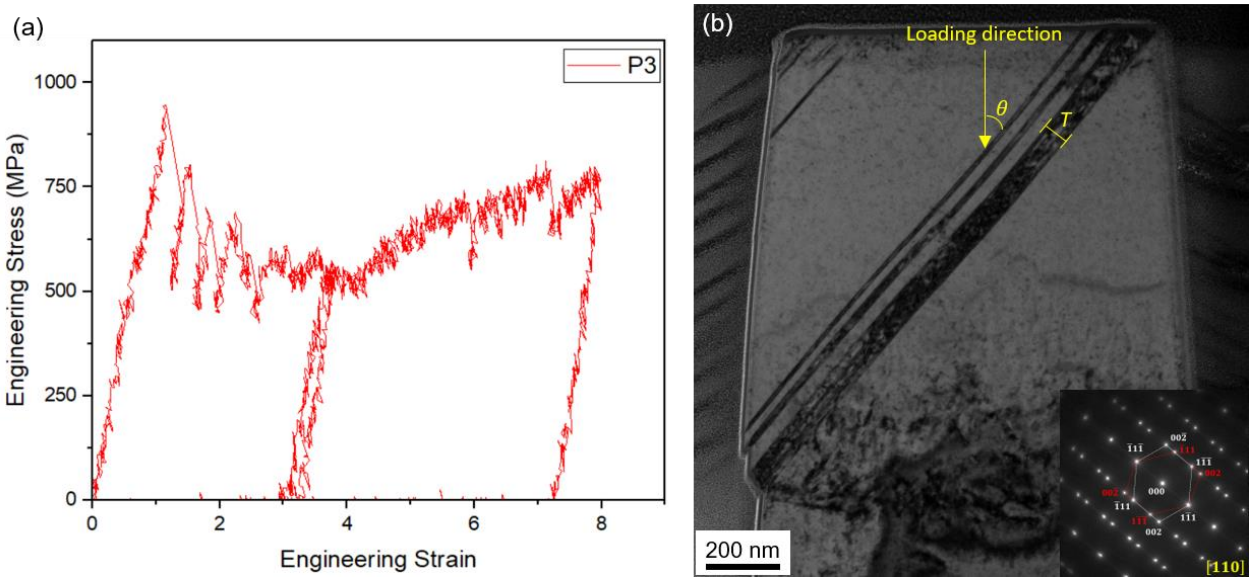

Figure 9-2 (a) Engineering stress and strain curve of micro-pillar P3 and (b) TEM BF micrograph also shown in Chapter 5 (modified from [9]).

Authors contribution to the original papers

Chapter 4: Quantitative measurement of twinning stress using various geometries

This Chapter is based on the manuscript: C.A. Teixeira, S. Lee, C. Kirchlechner, Measuring the twinning stress at the micron scale: A comprehensive comparison of testing geometries, Mater. Charact. 217 (2024) 114314. https://doi.org/10.1016/j.matchar.2024.114314.

The subsequent authors contribution to the original manuscript. All authors have agreed to have this manuscript as the Chapter 4 of this thesis.

Camila Aguiar Teixeira: Writing – original draft, Visualization, Methodology, Investigation, Formal analysis, Data curation, Conceptualization.

Subin Lee: Writing – review & editing, Supervision, Methodology, Investigation, Formal analysis, Data curation, Conceptualization.

Christoph Kirchlechner: Writing – review & editing, Supervision, Methodology, Funding acquisition, Formal analysis, Conceptualization.

Chapter 5: Insights into the twinning mechanism and stress analysis of the Cantor high entropy alloy

This Chapter is based on a manuscript submitted for publication and currently under review. The manuscript is entitled: "Mechanistic insights and stress analysis of deformation twinning in the Cantor high entropy alloy"

Authors: C.A. Teixeira[1], U. Bansal[1], G. Laplanche[2], P. Gumbsch[1], S. Lee[1], C. Kirchlechner[1]

[1]Institute for Applied Materials, Karlsruhe Institute of Technology, Karlsruhe, 76131, Germany

[2]Institut für Werkstoffe, Ruhr-Universität Bochum, Bochum, D-44801, Germany

The subsequent authors contribution to the original manuscript. All authors have agreed to have this manuscript as the Chapter 4 of this thesis.

Camila Aguiar Teixeira: Writing – original draft, Data curation, Methodology, Investigation, Formal analysis, Visualization.

Ujjval Bansal: Writing – review & editing, Investigation, Formal analysis.

Guillaume Laplanche: Writing – review & editing, Formal analysis.

Peter Gumbsch: Writing – review & editing, Formal analysis.

Subin Lee: Writing – review & editing, Data curation, Methodology, Investigation, Supervision, Formal analysis.

Christoph Kirchlechner: Writing – review & editing, Conceptualization, Methodology, Formal analysis, Supervision, Funding acquisition.

List of publications

2025 **C.A. Teixeira**, U. Bansal, G. Laplanche, P. Gumbsch, S. Lee, C. Kirchlechner, Mechanistic insights and stress analysis of deformation twinning in the Cantor high entropy alloy, *under review.*

2024 **C.A. Teixeira**, S. Lee, C. Kirchlechner, Measuring the twinning stress at the micron scale: A comprehensive comparison of testing geometries, Materials Characterization 217, 114314.

2024 F. Bignoli, P. Djemia, G. Terraneo, G. Abadias, C. Gammer, A. Lassnig, **C.A. Teixeira**, S. Lee, A. Ahmadian, A.L. Bassi, D. Faurie, M. Ghidelli, Novel class of crystal/glass ultrafine nanolaminates with large and tunable mechanical properties, ACS Applied Materials & Interfaces 16 (27), 35686-35696.

2023 R. Al-Salman, **C.A. Teixeira**, P. Zschumme, S. Lee, L. Griem, J. Aghassi-Hagmann, C. Kirchlechner, M. Selzer, KadiStudio use-case workflow: Automation of data-processing for in situ micropillar compression tests, Data Science Journal 22 (1).

2020 **C.A. Teixeira**, R.V. Da Silva, L.T. Pereira, M.F. de Oliveira, Oxygen effect on bending behavior of a zirconium based bulk metallic glass, Journal of Non-Crystalline Solids 535, 119966.